

1 **Fluvial sedimentary response to late Quaternary climate and tectonics at the**
2 **Himalayan Frontal Thrust, central Nepal**

3
4 **Mari Hamahashi^{1†}, Judith A. Hubbard^{1, 2}, Rafael V. Almeida³, Samuel H. Haines¹,**
5 **Lewis A. Owen⁴, Sanjita Mishra⁵, and Soma Nath Sapkota⁵**

6
7 ¹Earth Observatory of Singapore, Nanyang Technological University, Singapore, ²Asian
8 School of the Environment, Nanyang Technological University, Singapore, ³Department
9 of Geological Sciences, San Diego State University, USA, ⁴Department of Marine, Earth,
10 and Atmospheric Sciences, North Carolina State University, USA, ⁵Department of Mines
11 and Geology, National Seismological Center, Nepal

12
13 Corresponding author: Mari Hamahashi (mhamahashi@aquamarine.kobe-u.ac.jp)

14 †Current affiliation: Kobe Ocean-Bottom Exploration Center, Kobe University, Japan

15

16 **Key Points:**

17 • Boreholes combined with seismic profiles characterize the subsurface structure
18 and stratigraphy across the Main Frontal Thrust

19 • We document major transitions from fluvio-lacustrine to coarse fluvial channel
20 facies

21 • Indo-Asian monsoonal fluctuations have likely affected sediment supply and
22 river base levels in the frontal Himalaya of central Nepal

23

24

25

26

27

28

29

30

31 **Abstract**

32 To investigate the subsurface structure surrounding the Main Frontal Thrust (MFT) in
33 central Nepal, we drilled and cored sediments to depths of 45–100 m at ten sites. Our
34 boreholes were located along previously acquired high-resolution seismic profiles across
35 the MFT imaging the upper 1–2 km of the subsurface, which revealed a beveled erosional
36 surface in the hanging wall above a broad, gentle anticline, as well as growth strata in the
37 footwall. The boreholes exhibit interlayered clays, silts, sands, and gravels, dated with
38 optically stimulated luminescence and radiocarbon to $<72.5 \pm 4.3$ ka, with a transition from
39 finer to coarser sediments at $\sim 13.5 \pm 0.1$ ka. Near the fault tip, the sediments exhibit steeper
40 dips and deformation bands. A 25-m-thick section of silt and clay above the south end of
41 the buried anticline is interpreted as a temporary lacustrine depocenter formed due to
42 uplift near the fault tip. Based on the distribution of marker beds and sediment ages, we
43 interpret a shortening rate of 3.1–12.1 mm/a on the MFT. Three major transitions between
44 fluvio-lacustrine and coarse fluvial channel facies are inferred from the boreholes, and
45 the timings of these transitions correlate with Indian monsoonal intensity variations
46 linked to Earth's precession. We infer that strengthened monsoon led to increased river
47 discharge and advance of coarse bedload-dominant braided channels, whereas weak
48 monsoon formed a finer-grained channel environment. These monsoonal climate

49 variations have affected the depositional environment and river base levels in this region,
50 influencing the formation and apparent relative uplift of nearby river terraces.

51

52 **Plain Language Summary**

53 The Main Frontal Thrust (MFT) is the youngest and most active fault at the foot of the
54 Himalayan mountain belt, posing a major seismic hazard to the dense populations living
55 in the Himalaya and the Indo-Gangetic Plain. To study the recent deformation history of
56 the MFT in central Nepal, we drilled and sampled sediments to depths of 45–100 m at ten
57 sites. Our boreholes were located where previous surveys have imaged the structures of
58 the MFT using a seismic technique. The recovered sediments consist of clays, silts, sands,
59 and gravels. The deformation by the MFT is characterized by folding and steeply-dipping
60 sediments at the tip of the fault. We used two different methods to date the ages of the
61 sediments, called optically stimulated luminescence and radiocarbon dating. Based on the
62 observed structures and sediment ages, we interpret that the MFT in this region is slipping
63 at a rate of 3.1–12.1 mm/a. Three major transitions from coarse- to fine-grained sediments
64 indicate past changes in the river environment; these correlate with Indian monsoonal
65 climate changes. We interpret that monsoonal variations have significantly influenced

66 sediment deposition and erosion, impacting the geomorphology and relative uplift of the
67 region.

68

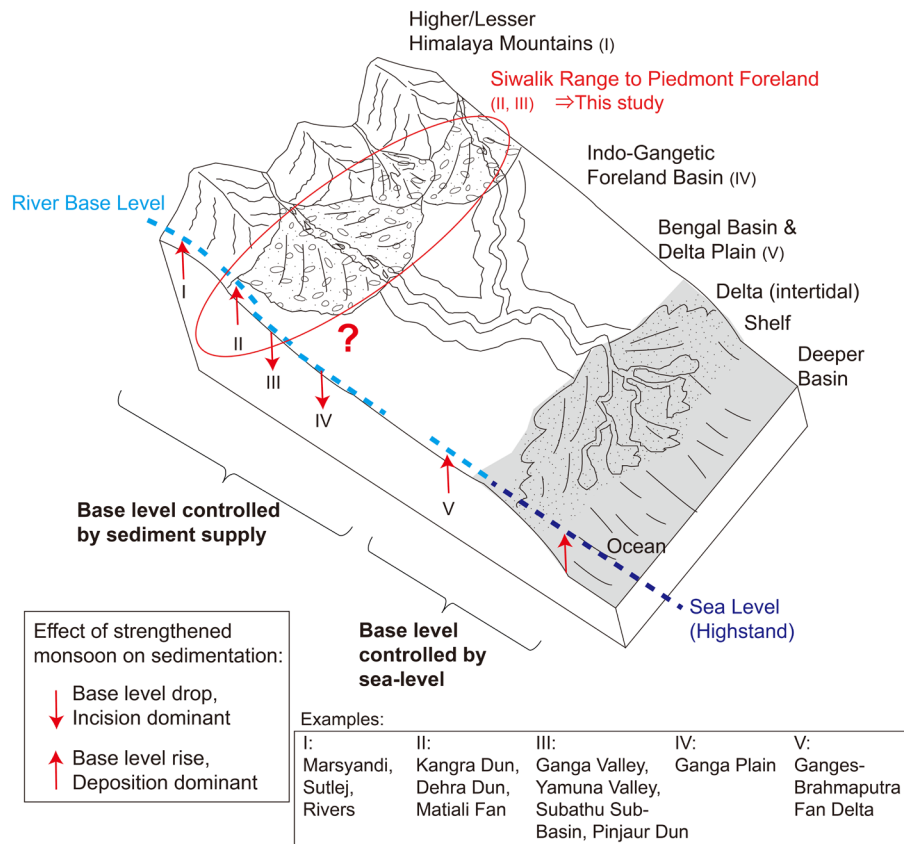
69 **1. Introduction**

70 Understanding the processes that govern sediment supply and river base levels in
71 an orogenic foreland is important for interpreting depositional processes, incision, and
72 tectonic deformation. River base level, which is the lowest level of erosion or the highest
73 level of sedimentary succession in a river profile, defines the equilibrium surface between
74 deposition and incision (e.g., Blum & Tornqvist, 2000; Catuneanu et al., 2009). In
75 tectonically active regions, rock uplift or subsidence is generally considered to be the
76 main driver for local base-level change, leading to river incision or fluvial sediment
77 deposition; an example of this interaction is steady-state topography models that assume
78 that erosion balances rock uplift, and thus there is no change in the landscape over time
79 (e.g., Willet & Brandon, 2002). Tectonic uplift plays a major role in the frontal Himalaya,
80 where young active faults underlie and deform sediments at the piedmont.

81 Climate can also play an important role in modulating river base levels in foreland
82 systems. In the Himalayan foreland, the Indian summer monsoon is responsible for more

83 than 80% of the annual rainfall, significantly impacting river discharge and sediment flux
84 in both the foreland and downstream in the Indo-Gangetic-Bengal basin (e.g., Bookhagen
85 et al., 2010). Changes in the monsoonal climate are known to affect sedimentation and
86 river base levels over various timescales (e.g., Plink-Björklund, 2015), but their effects in
87 the proximal foreland are not well understood (Fig. 1). While river base levels close to
88 the coast are primarily affected by sea level (e.g., Goodbred et al., 2014), those in the
89 frontal foreland are largely influenced by sediment supply and the combined effects of
90 climate and tectonics (e.g., Bookhagen et al., 2005; Fig. 1). This impact of climate on
91 base level should be taken into account when interpreting tectonic deformation from
92 geomorphology; here, we study this effect in the frontal Himalaya of central Nepal.

93



94

95 **Figure 1. Variations in river base levels in the Himalayan foreland system in**

96 **response to strengthened Indian monsoon, from the high mountains to the ocean**

97 **basin. During strong Indian monsoon events, an increase in river discharge and**

98 **sediment supply are inferred to cause aggradation and base level rise in regions I, II**

99 **and V, whereas incision and base level fall occur in III and IV, notably variable**

100 **within the piedmont foreland (regions II and III). An opposite process is inferred**

101 **during weak monsoon periods. Base levels in regions I-IV are likely controlled**

102 **mainly by sediment supply, whereas region V is controlled by sea level. References**

103 **for each example in regions I-IV (lower rectangle) are as follows (locations are shown**

104 **in Supporting Information Figure S8). I: Marsyandi river (Pratt et al., 2002), Sutlej**
105 **river (Bookhagen et al., 2005, 2006). II: Kangra dun (Thakur et al., 2014; Dey et al.,**
106 **2016), Dehra dun (Densmore et al., 2016), Matiali fan (Kar et al., 2014). III: Ganga**
107 **valley (Sinha et al., 2009; Ray and Srivastava, 2010), Yamuna valley (Dutta et al.,**
108 **2012), Subathu sub-basin (Kumar et al., 2007), Pinjaur dun (Suresh et al., 2007). IV:**
109 **Ganga plain (Srivastava et al., 2003b; Gibling et al., 2005; Sinha et al., 2007). V:**
110 **Ganges-Brahmaputra fan delta (Goodbred and Kuehl, 2000 a,b; Goodbred et al.,**
111 **2014; Pickering et al., 2014, 2017).**

112

113 The thrust system at the foot of the Himalaya is composed of a largely right-
114 stepping fault system called the Main Frontal Thrust (MFT), which dips 20°–40° to the
115 north before linking with a gently dipping megathrust at 2–5 km depth, the Main
116 Himalayan Thrust (MHT; Almeida et al., 2018). In the Bardibas region of central Nepal,
117 this fault system has been imaged by high-resolution seismic profiles that cross two
118 strands of the MFT, locally named the Bardibas and Patu thrusts, constraining both the
119 local deformation and the depositional environment (Almeida et al., 2018; Liu et al.,
120 2020; Figs. 2, 3; Supporting Information Fig. S1). These seismic profiles indicate that the
121 southern MFT strand (the Bardibas thrust) at this location is blind (Figs. 3a,b).

122 Furthermore, as slip on this fault decreases to the west, the geomorphic signature of the
123 fault decreases, with the westernmost 5 km of fault-related deformation completely erased
124 by surface processes (Fig. 2c). In this tip region, the seismic profiles reveal a ~4-km-wide
125 hanging-wall anticline bevelled by erosion and then later buried by ~100 m of sediments
126 (Almeida et al., 2018; Fig. 3c). This relationship cannot be explained by tectonics alone,
127 and implies that the local river base level was at least ~100 m lower at some point in the
128 past. A scour surface interpreted as an incised valley within the growth strata of the
129 footwall suggests that similar base-level changes may have occurred multiple times
130 (Almeida et al., 2018).

131 To constrain the depositional patterns, rates of deformation, and evolution of
132 inferred incision/aggradation events near the MFT in central Nepal, we drilled and cored
133 the imaged stratigraphy to depths of 45–100 m below the surface (mbs) at ten locations
134 in the hanging wall and footwall of the Bardibas thrust (Figs. 2, 3). Here, we characterize
135 the sedimentary facies from recovered cores and report on sediment ages obtained by
136 optically stimulated luminescence (OSL) and radiocarbon (^{14}C) dating. By combining our
137 observations with previously acquired seismic profiles, our analyses allow us to 1)
138 reconstruct the shallow structure and infer the slip rate of the Bardibas thrust, and 2)
139 interpret the evolution of the depositional environment and river base levels in this region

140 in relation to past climatic changes.

141

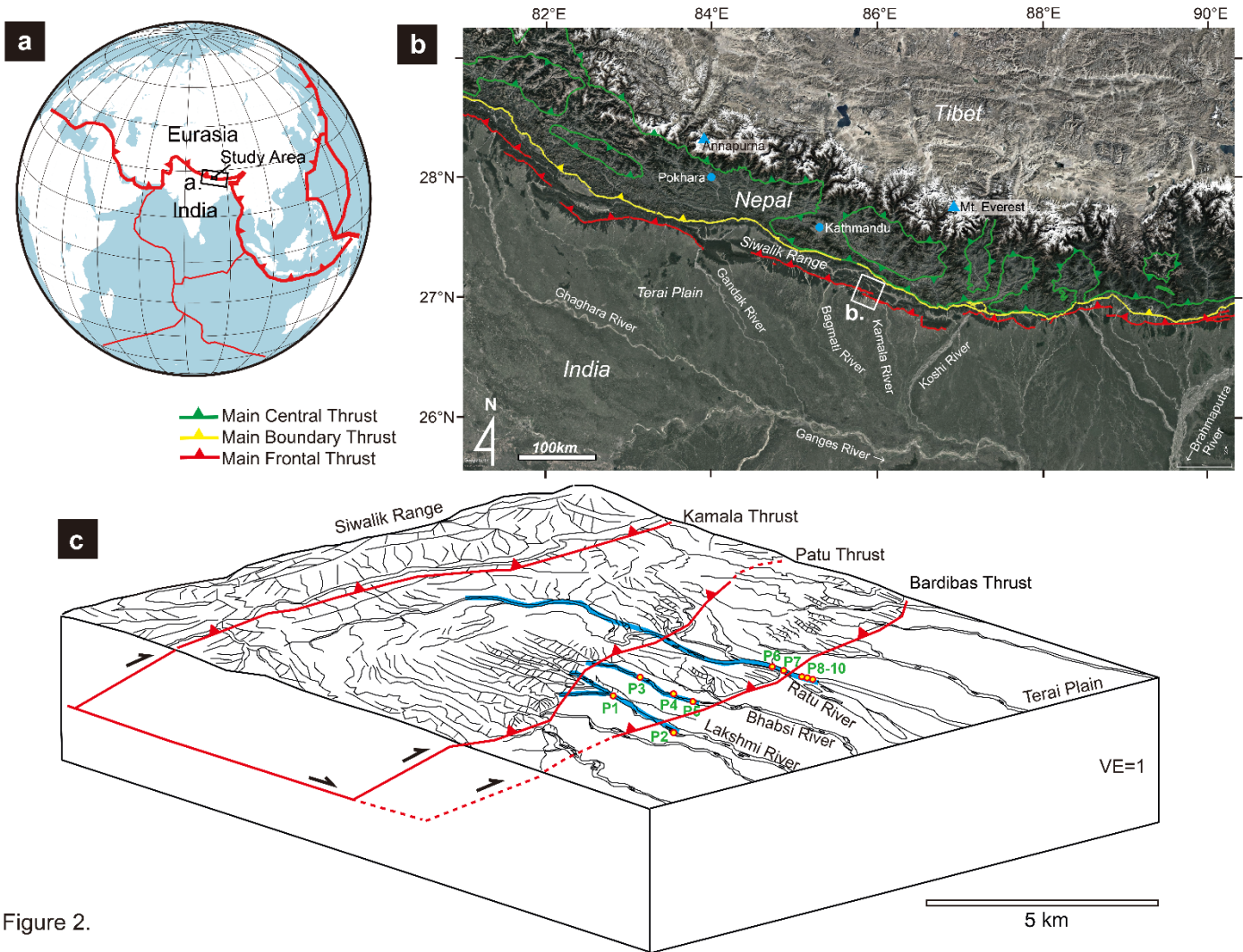


Figure 2.

142

143 **Figure 2. Regional map of study area. (a) Major tectonic plate framework showing**

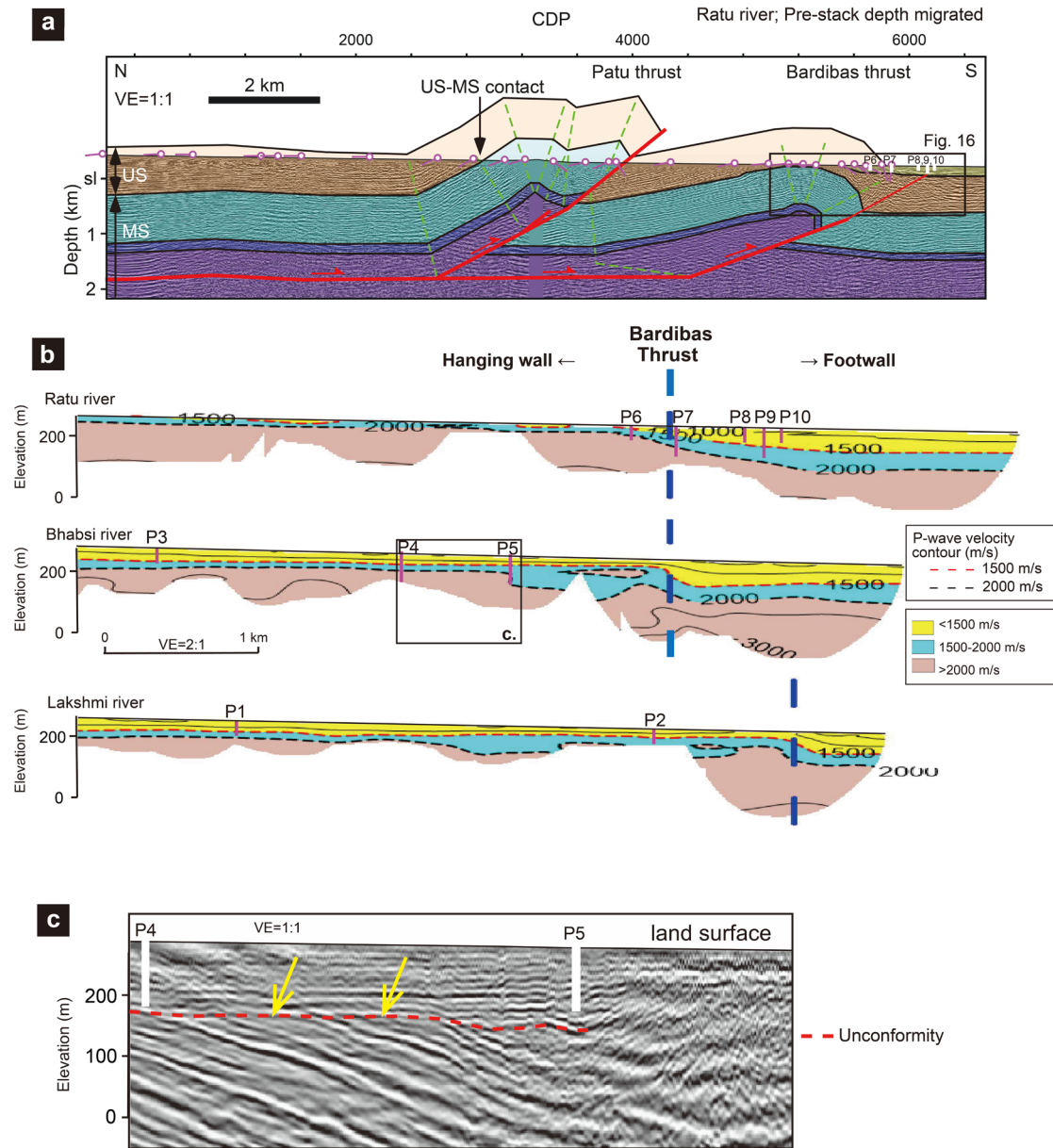
144 **collision of India to Eurasia, and location of study area. Box shows location of (a).**

145 **(b) Satellite image showing major Himalayan faults and river systems from high**

146 **mountains to foreland basin (Terai plain). The Siwalik Range is located between the**

147 **Main Frontal Thrust and Main Boundary Thrust. White box marks the location of**
148 **study area shown in (c). (c) Close-up of study area showing traced geography of the**
149 **frontal foreland and braided river system. Drill sites are shown by yellow dots**
150 **labeled P1–P10, along the Lakshmi, Bhabsi, and Ratu rivers. Blue lines show**
151 **locations of previously acquired seismic reflection profiles along the rivers (Almeida**
152 **et al., 2018; Liu et al., 2020) (Figure 3). Red lines: approximate locations of the fault**
153 **strands of the Main Frontal Thrust in this region. Red dashed lines: locations where**
154 **the fault displacement decreases and are likely terminated. The geomorphological**
155 **signature of the Bardibas thrust decreases west of the Bhabsi river. No vertical**
156 **exaggeration.**

157



158

159 **Figure 3. Sections across the study area. (a) Interpreted Ratu river seismic profile**

160 **(pre-stack depth-migrated, no vertical exaggeration) by Almeida et al. (2018) (red**

161 **lines: thrusts; green dashed lines: axial surfaces). Uninterpreted profile is shown in**

162 **Supporting Information Fig. S1. CDP spacing is 2.5 m. Depth measurements are**

163 **with respect to sea-level (sl). White vertical bars show locations of borehole sites P6–**

164 **P10 in this study. US: Upper Siwalik Group. MS: Middle Siwalik Group. Contact**
165 **between US and MS observed in the field. Magenta tick marks: projected bedding**
166 **dips measured from the field (Almeida et al., 2018). Area of black box is shown in**
167 **Figure 16. (b) 2D refraction velocity models by Liu et al. (2020) generated from**
168 **seismic data collected along Ratu, Bhabsi, and Lakshmi rivers (vertical exaggeration**
169 **2:1), with locations of borehole sites (magenta bars) P1–P10. Each contour line**
170 **shows 500 m/s velocity interval. Red and black dashed lines show the 1500 and 2000**
171 **m/s contours, respectively. Blue vertical dashed lines represent the approximate**
172 **location of the tip of the Bardibas thrust. Black box along Bhabsi river shows**
173 **location of seismic reflection image shown in c. (c) Section of Bhabsi river seismic**
174 **profile (post-stack depth-migrated, no vertical exaggeration) on the hanging wall of**
175 **the Bardibas thrust by Almeida et al. (2018), showing close-up of the buried angular**
176 **unconformity (marked by yellow arrows and red dashed line) between tilted Siwalik**
177 **Group strata (below) and subhorizontal fluvial sediments (above). White vertical**
178 **bars show locations of boreholes P4 and P5.**

179

180 **2. Geologic Setting**

181 The Himalaya is currently accommodating shortening at a rate of $\sim 13\text{--}21$ mm/a
182 (Larson et al., 1999; Ader et al., 2012; Lindsey et al., 2018). The MFT is the youngest and
183 most active fault of the Himalayan orogen, extending >2500 km along strike. During the
184 interseismic period, geodetic observations show shortening accumulating around the deep
185 base of the megathrust, but most of this shortening is expected to eventually reach the
186 surface as slip along the MFT (Lavé and Avouac, 2001), likely during or soon after large
187 earthquakes, as inferred from paleoseismic studies (e.g., Nakata et al., 1998; Lavé et al.,
188 2005; Sapkota et al., 2013; Bollinger et al., 2014; Wesnousky et al., 2017; Wesnousky,
189 2020; Dal Zilio et al., 2021). This seismic hazard poses a threat to the populations living
190 in the Himalaya and its foothills, as well as the densely populated areas of the Indo-
191 Gangetic Plain. The fault system also modifies the accommodation space and sediment
192 supply to the largest foreland basin system on Earth, i.e., the Indo-Gangetic Plain (e.g.,
193 Kumar et al., 2007).

194 Our study area in central Nepal (Fig. 2) is located in the lowlands between the
195 foothills of the Himalaya (the Siwaliks) and the Indo-Gangetic Plain, a region known as
196 the Terai. Located within ~ 1 km south of the topographic range front, the area is actively
197 deforming due to slip on the Patu and Bardibas thrusts (e.g., Bollinger et al., 2014;

198 Almeida et al., 2018) (Figs. 2, 3). Paleoseismic studies have identified fault offsets
199 associated with the last two great ($M > 8$) earthquakes in east-central Nepal along the Patu
200 thrust (1255 and 1934 CE; Sapkota et al., 2013; Bollinger et al., 2014). In contrast, no
201 surface rupture has been identified along the Bardibas thrust, although a fold scarp has
202 been found (Bollinger et al., 2014).

203 The fault system here has been characterized by seismic reflection surveys, which
204 imaged the $\sim 20\text{--}30^\circ$ north-dipping Bardibas thrust as blind, and the $\sim 28\text{--}39^\circ$ north-
205 dipping Patu thrust as emergent (Figs. 3a; Almeida et al., 2018). Refraction velocities
206 determined from the seismic data document the distribution of low-velocity sediments
207 overlying the more lithified Siwalik bedrock in the hanging wall ($\sim 20\text{--}50$ m thick) and
208 footwall ($\sim 80\text{--}120$ m thick) of the Bardibas thrust, indicating relatively recent sediment
209 deposition across the fault, with $\sim 60\text{--}70$ m of uplift since their deposition (Fig. 3b; Liu et
210 al., 2020). The effect of fault-related shortening on the Bardibas thrust should be to raise
211 the hanging wall relative to base level and cause incision; the observation of deposition
212 (Fig. 3c) therefore implies that another factor must be influencing base level, and the
213 magnitude of that effect must exceed that of local tectonics. Specifically, exogenetic
214 factors such as climate must play an important role in modulating the river base levels
215 and incision in this region (Almeida et al., 2018).

216 The bedrock in the study region consists of the Miocene-Pliocene Siwalik Group,
217 which is a set of fluvial strata comprising at large scale an overall coarsening-upward
218 sequence of alternating beds of sandstone and siltstone with lenses of conglomerate, with
219 smaller-scale fluvial successions showing fining-upward sequences (Corvinus, 2001;
220 Ulak, 2009; Dhital, 2015; Supporting Information Fig. S2a). The current depositional
221 environment is characterized by confined braided channels with minor overbank
222 floodplains within a channel-dominant alluvial fan system. The contemporary alluvial fan
223 is surrounded by abandoned river terraces, older alluvial fans, and uplifted hills.

224 The highest river terrace is ~70 m above the current riverbed and has a reported
225 age of ~7 ka based on radiocarbon dating of a charcoal buried in the same horizon as
226 cobble tool assemblages (artefacts of paleolithic industry) found within the sediments
227 (Gaillard et al., 2011; Bollinger et al., 2014). A succession of six to seven younger river
228 terraces, presumably abandoned during the Holocene, are also present (e.g., Gaillard et
229 al., 2011; Bollinger et al., 2014). These river terraces are both deposition-dominant “fill
230 terraces,” which exhibit thick alluvial fills not exposing the underlying bedrock, and
231 incision-dominant “strath terraces,” which are underlain by tilted bedrock (Supporting
232 Information Figs. S2b,c, S3). South of the Bardibas thrust, the rivers supply sediments
233 into the Indo-Gangetic foreland basin between the Koshi and Gandak megafans (e.g.,

234 DeCelles and Cavazza, 1990; Sinha et al., 2014). Surprisingly, as the rivers travel
235 hundreds of kilometers towards the southeast, their channel widths decrease (from ~300
236 m to ~10 m wide) (Supporting Information Fig. S4). Some of these narrow meandering
237 channels are abandoned, while others eventually merge with the Koshi river and flow into
238 the Ganges-Brahmaputra rivers and the Bay of Bengal (Supporting Information Fig. S4a).

239 In contrast to the major transverse Himalayan rivers, e.g., Ganga, Maakali, Karnali,
240 Narayani, and Koshi rivers, which cut across the High Himalaya with large drainage
241 basins, the catchment areas of the Lakshmi, Bhabsi, and Ratu rivers in this study are
242 confined to the southern part of the Siwalik Range (area <100 km²), and the drainages are
243 hence younger (Fig. 2; Supporting Information Fig. S4). The rivers are supplied mainly
244 by seasonal monsoon rainfall and associated runoff, with hardly any contribution of
245 snowmelt (e.g., Bookhagen and Burbank, 2010). Annual rainfall around the Siwalik
246 Range is about 2.8–3.8 m/a in central-eastern Nepal, with >80% of total precipitation
247 occurring during the Indian summer monsoon (Bookhagen and Burbank, 2010). The
248 moisture is derived from the Bay of Bengal and is carried north and rainfall peaks spatially
249 south of the topographic barriers formed by the Lesser and Higher Himalayas (e.g.,
250 Bookhagen and Burbank, 2010; Hirschmiller et al., 2014; Deal et al., 2017). The rivers in
251 the foreland thus have highly variable water discharge, experiencing high flow and

252 flooding during the monsoon, with a long dry period for the rest of the year. Because the
253 monsoon supplies large amounts of water to this river system, climate-driven changes in
254 monsoon intensity are expected to be one of the key paleoenvironmental controls on its
255 fluvial sedimentary record.

256

257 **3. Methods**

258 To investigate the subsurface structure surrounding the MFT, we drilled and cored
259 sediments to depths of 45–100 m at ten sites (Sites P1–P10) across the fault. Drilling was
260 conducted along the Lakshmi, Bhabsi and Ratu rivers around the town of Bardibas in the
261 Mahottari district of central Nepal (Figs. 2). These rivers flow nearly perpendicular to the
262 MFT. Sites P1–P5 are located on the hanging wall of the Bardibas thrust, whereas Sites
263 P6–P10 are located on the footwall (Figs. 2b, 3).

264 Rotary drilling was applied using XUL-100 and UEW vol-35 drill rigs and NQ
265 double core barrels, with core recovery of 28–59% (average: 41%), and maximum
266 penetration depths of 45–100 mbs. There was no attempt to core the first 5 m of each
267 borehole. Areas of low recovery were associated with coarse gravels and poorly sorted
268 fluvial sediments. The cores were transferred from the core barrel to rolled tins with a

269 mechanical extruder, tightly secured to avoid light exposure, transported to Kathmandu,
270 and then cut in a dark room, preserving 25–30 cm of core every 2 m for sampling for OSL
271 dating. The rest of the cores were then cut open, and laid in steel trays for observation.

272 The recovered cores were logged based on principal grain size range, sediment
273 color, lithification, bed thickness, grading, sorting, clast size, sedimentary and
274 deformation structures, weathering, organic content, and bioturbation (Supporting
275 Information Dataset S1). The orientations of structures such as bedding were measured
276 using core protractors by Holcombe Coughlin Oliver (www.hcovglobal.com). We also
277 referred to the geotechnical reports from the drilling operations to infer the lithology
278 where the cores had low or no recovery (Supporting Information Dataset S2). All core log
279 data were digitized using Strater 5 (Golden Software LLC), and facies were interpreted.
280 We combined our observations with the co-located seismic reflection profiles of Almeida
281 et al. (2018; and unpublished data) to reconstruct regional cross-sections.

282 To date the sediments, we conducted OSL dating on quartz grains in fine sand,
283 and accelerator mass spectrometry ^{14}C dating on organic sediments (see details in
284 Supporting Information Texts S1, S2, Figs. S5–S7). Eighteen OSL samples were
285 measured at the University of Cincinnati and North Carolina State University, using an
286 automated Riso OSL reader model TL-DA-20. At least thirty-two quartz aliquots were

287 measured for each sample. The single aliquot regeneration (SAR) method (Murray &
288 Wintle, 2000, 2003) was used to determine the dose rate for age estimation. To help
289 resolve the overestimate of ages due to partial bleaching and hence a large spreads of
290 equivalent dose values (dispersion >25%), we applied a 2-mixing model (Vermeesch,
291 2009) to determine the minimum age for samples that yielded >25% dispersion. For
292 samples that showed $\leq 25\%$ dispersion, we used the average OSL ages.

293 Fourteen samples of organic sediments were measured for ^{14}C dating at Beta
294 Analytics Inc., using NEC accelerator mass spectrometers. Given the absence of detrital
295 charcoals and other macrofossils, the bulk organic fraction (carbon content: 0.06–1.62%)
296 smaller than 180 μm , inclusive of humic and humins, was used for dating. $\delta^{13}\text{C}$ values
297 were measured separately by Thermo isotope ratio mass spectrometers (IRMS).
298 Conventional radiocarbon ages were calculated using the Libby half-life (5568 years),
299 and were corrected for total isotopic fractionation effects. Errors reported from the
300 laboratory are based on 1-sigma counting statistics. Calibration of the conventional age
301 was performed using the 2013 calibration databases (INTCAL13) (Reimer et al., 2013),
302 high probability density range method, and Bayesian probability analysis (Ramsey, 2009).
303

304 **4. Results**

305 **4.1. Core descriptions**

306 Three sedimentary facies were present within the recovered cores: 1) poorly
307 sorted gravels with silt to sand, interpreted to represent coarse-grained braided channel
308 facies (herein “Facies A”); 2) moderately sorted silt to sand with gravels sandwiched by
309 thin floodplain silts, interpreted to represent fine-grained braided channel facies (herein
310 “Facies B”); and 3) massive, well-sorted clayey silt with bioturbation, alternating redox
311 state and occasional sand beds, interpreted to represent fluvio-lacustrine facies (herein
312 “Facies C”). In all boreholes, Facies A caps the upper section, overlying Facies B and C
313 (Figs. 4–10). Detailed lithological and structural features for each site are described in
314 this section. The recovered gravels are mainly metamorphosed quartz-feldspar-mica
315 sandstone including quartzite. These are similar to typical clasts found in conglomerates
316 of the Upper Siwaliks Group and are likely reworked derived clasts (e.g., Dhital, 2015).

317

318 **4.1.1 Lakshmi river (Hanging wall)**

319 **4.1.1.1 Site P1 (27.03302°N, 85.87577°E; total depth of core: 55 mbs)**

320 The recovered sedimentary sequence at Site P1 (0–55 mbs) (Fig. 4a) consists of

321 three beds of 6–11-m-thick, poorly sorted gravels ($16 \text{ mm} < \text{diameter (d)} < 256 \text{ mm}$) with
322 a matrix of fine-coarse sand (Fig. 5a), assigned as Facies A, interbedded with 7–11-m-
323 thick moderate-poorly sorted, grayish-orange silt to medium sand, and well-sorted silt
324 (Fig. 5b), assigned as Facies B. These interbeds of coarse and fine sediments are
325 interpreted to represent bedload and suspended load deposits of a braided river system.
326 Well-sorted silts (at 12–14 and 34–35 mbs) are thin, and occur near the base of coarser
327 beds; we interpret these to have floodplain or aeolian origin (Fig. 5b). The sediments are
328 generally massive, and contain occasional rip-up clasts. The presence of oxidized patches
329 and black Fe/Mn oxides in fine-grained sediments indicate moderate
330 pedogenesis/weathering.

331

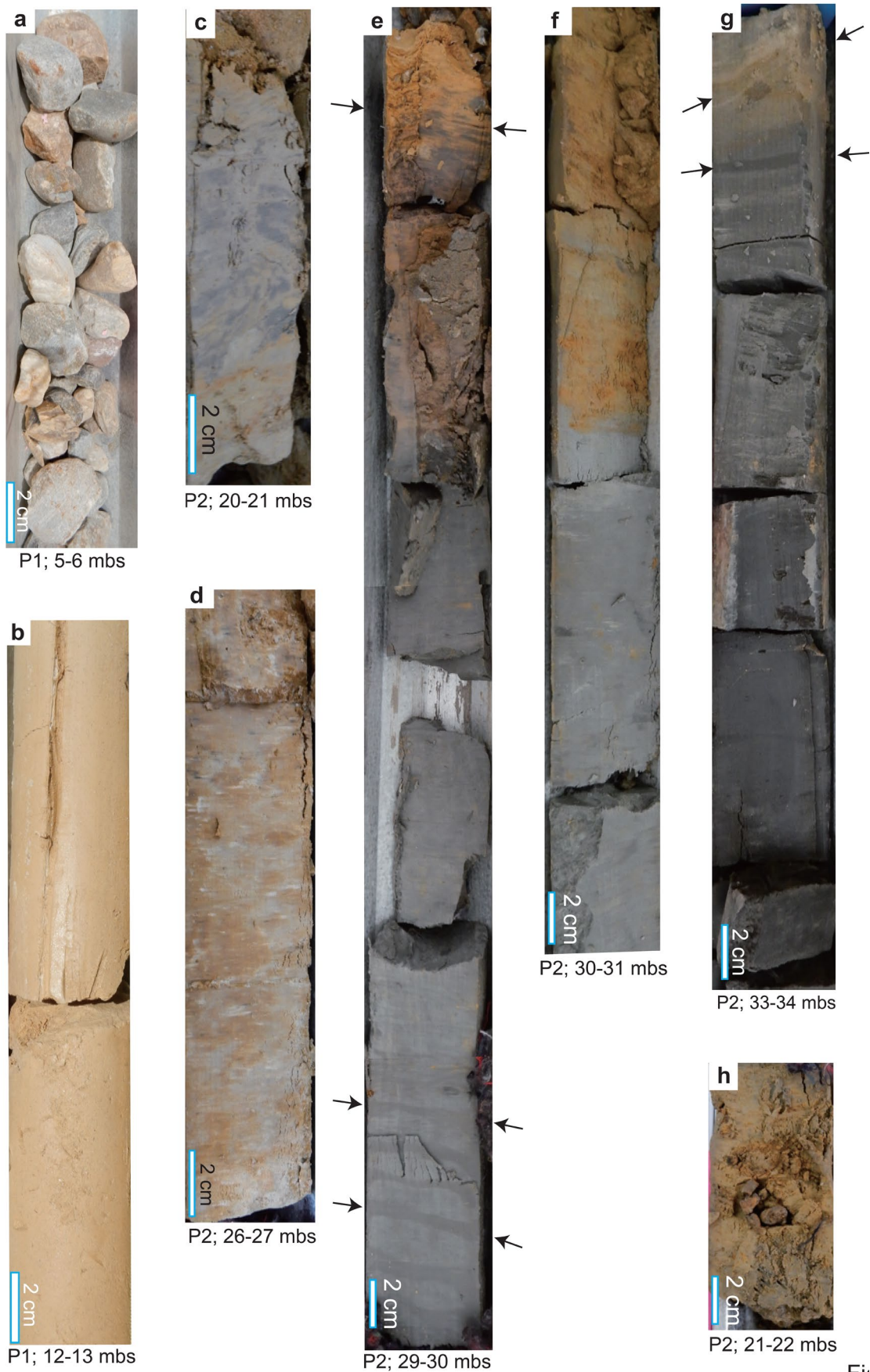
332 **4.1.1.2 Site P2** (27.01315°N, 85.85964°E; total depth of core: 45 mbs)

333 The upper 20 m of sediments at Site P2 (Fig. 4b) consist of mostly poorly sorted
334 gravels ($16 \text{ mm} < \text{d} < 128 \text{ mm}$) with variable amounts of fine to coarse sand; these likely
335 represent bedload-dominant channel deposits and are assigned as Facies A. In contrast,
336 the underlying sediments (20–45 mbs) consist of primarily well-sorted clayey silt, with
337 several beds of fine to medium sand containing a few gravel clasts (a few cm to 3 m thick,
338 with the thickest sections at 29–33, 35–38 and 42–45 mbs); this suggests a change in

339 depositional environment (Figs. 5c–h). Bioturbation by burrowing and color mottling
340 associated with an irregular distribution of Fe/Mn oxides are distinct, reflecting
341 pedogenesis (Figs. 5c,d). These sediments are generally massive, occasionally containing
342 rhythmic interbeds of silt and clay (0.2–2 cm thick; Figs. 5e–g). Other sedimentary
343 structures include silty rip-up clasts and silt dikes. These sediments are interpreted to have
344 been deposited in a waterlogged, low-energy lacustrine environment in the vicinity of a
345 channel, with pulses of sandy fluvial inputs and aeolian silts (loess), which we assign as
346 Facies C.

347 The observed bedding planes are mostly sub-horizontal, dipping between 0° and
348 10° (Fig. 4b). The interval at 20–29 mbs is characterized by oxidized, dark yellowish
349 orange silty clay with distinct pedogenic features, including rounded mud-filled nodules
350 (Fig. 5h); below 29 mbs, gleyed dark gray sediments are more dominant (Fig. 4b).
351 Gradual alternations between gleyed silty clay and oxidized silty clay are common at 29–
352 34 mbs, implying changes between anaerobic and aerobic conditions (Figs. 5e–g).

353



363

E..

364 **Figure 5. Representative features of cores from Lakshmi river Sites P1 and P2. Cores**
365 **in each image are shallowing upward. (a) Coarse gravels at Site P1; 5–6 mbs. (b)**
366 **Well-sorted silt at Site P1; 12–13 mbs. (c) Silty clay exhibiting bioturbation at Site**
367 **P2; 20–21 mbs. (d) Silt with mottled texture interpreted to be paleosol at Site P2;**
368 **26–27 mbs. (e) Transition from gleyed to oxidized silty clay, with thin interbeds of**
369 **silt and clay (marked by arrows) at Site P2; 29–30 mbs. (f) Transition from gleyed**
370 **clay to oxidized silt at Site P2; 30–31 mbs. (g) Interbeds of silt and clay showing**
371 **cross-bedding (marked by arrows) at Site P2; 33–34 mbs. (h) Rounded mud-filled**
372 **nodules observed in silty clay at Site P2; 21–22 mbs.**

373

374 **4.1.2 Bhabsi river (Hanging wall)**

375 **4.1.2.1 Site P3 (27.02714°N, 85.88994°E; total depth of core: 50 mbs)**

376 The upper 27 m of sediments at Site P3 (Fig. 6a) are mostly coarse gravels (8 mm
377 $< d < 64$ mm) with variable amounts of sand, and are assigned as Facies A. Beneath this
378 unit (27–50 mbs, base of core), the sediments are finer grained, characterized by
379 moderately to poorly sorted fine to medium sand with gravels, interbedded with well-
380 sorted silt to clay, assigned as Facies B. The well-sorted fine sediments include brown

381 clay (Fig. 7a), grayish-orange silt, and gleyed clay/silt, interpreted to be of floodplain
382 origin. These sediments are massive and thinly bedded, with no bioturbation, contrasting
383 with the lacustrine sediments at Site P2. A distinct, lithified organic-rich black clay
384 (possibly a paleosol) is present at 40 mbs and coarsens up to fine sand (Fig. 7b). This
385 observed reverse grading was likely caused by a gradual increase in water level during
386 flooding in the overbank (e.g., Iseya, 1989; Rubin et al., 1998; Skolasińska, 2014).

387 The sediments are generally structureless, occasionally containing rip-up clasts
388 and oxidized spots. Gradual transitions from silt to clay and from sand to silt show wavy
389 contacts that dip 15–30° below 40 mbs (Fig. 6a). Infiltration of roots and organic materials
390 in brown and gleyed clay, together with the distribution of Fe/Mn oxides, indicates
391 pedogenesis.

392

393 **4.1.2.2 Site P4** (27.01497°N, 85.88236°E; total depth of core: 100 mbs)

394 The upper 42 m of sediments at Site P4 (Fig. 6b) are mostly coarse gravels (16
395 mm < d < 256 mm) with coarse sand and thin layers of poorly sorted sandy clay with
396 pebbles, representing bedload-dominant channel deposits, assigned as Facies A. From
397 42–100 mbs (base of the core), the sediments are finer grained, consisting of packages of
398 silt to very coarse sand with gravels, assigned as Facies B (Fig. 7c–f). These sediments

399 generally have normal grading, sandwiched by well-sorted gleyed clayey silt, grayish-
400 orange silt, and/or brown clay, interpreted to be floodplain deposits. Under the microscope,
401 the gleyed sediments contain disseminated pyrite and ferrous minerals that presumably
402 formed under reducing conditions.

403 Moderate to intense color mottling due to bioturbation and pedogenesis are
404 common in the fine sediments, as are fine-grained rip-up clasts. The sediments are
405 generally massive, except for several horizons of inclined laminas in silty fine sand (Figs.
406 7c,d), which dip 3–45° below 55 mbs (Fig. 6b). These dips likely reflect local sedimentary
407 processes such as cross-bedding, and/or post-depositional processes such as soft sediment
408 deformation.

409

410 **4.1.2.3 Site P5** (27.00879°N, 85.88044°E; total depth of core: 95 mbs)

411 The upper 68 m of sediments at Site P5 (Fig. 6c) are mostly coarse gravels (16 mm
412 $< d < 256$ mm) with variable amounts of silt to coarse sand, occasionally interbedded with
413 poorly sorted silty clay to fine sand with pebbles, assigned as Facies A. From 68–95 mbs
414 (base of the core), the sediments are finer grained, consisting of normally graded, poorly
415 sorted silt to coarse sand with gravels of Facies B (Fig. 7g–i). Inclined laminas in silty
416 fine sand are present, and are mostly oxidized (Fig. 7i). Very well sorted, clayey silt is

417 thinly interbedded between coarser channel deposits, and is interpreted to represent
 418 aeolian/floodplain sediment. The dips of these laminae and silt beds range from 5°–65°
 419 and 2–30°, respectively (Fig. 6c), and they likely reflect largely local depositional
 420 processes such as cross-bedding, and/or post-depositional processes such as soft-sediment
 421 deformation.

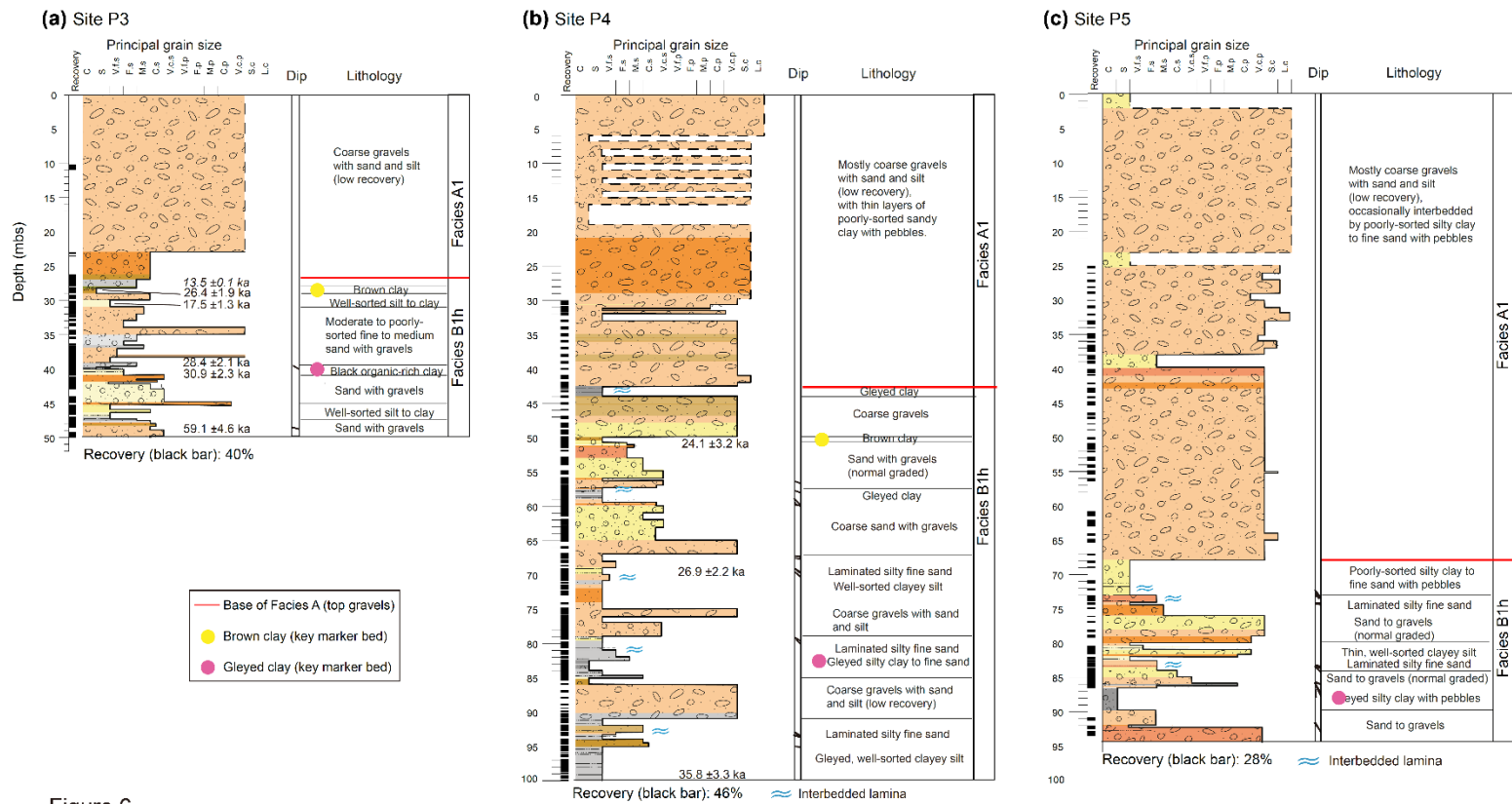


Figure 6.

422 **Figure 6. Graphic sedimentary core logs for Bhabsi river sites (a) P3, (b) P4, and (c)**
 423 **P5 showing principal grain size, sediment color, dip angles and description of**
 424 **lithology. Black bars show recovered core. Symbols next to core log are described in**
 425 **legend below. Dating results are for OSL and radiocarbon (*italic*) ages. Age results**

426 **are detailed in Figure 12 and Tables 1 and 2. Measured dip angles are shown as tilted**
427 **lines. Facies A and B are interpreted facies (see Section 4.2 for details). Red line**
428 **marks the base of top gravel section (Facies A1). Brown clay (yellow dots) and gleyed**
429 **clay (pink dots) are key beds traced in Fig. 14.**

430

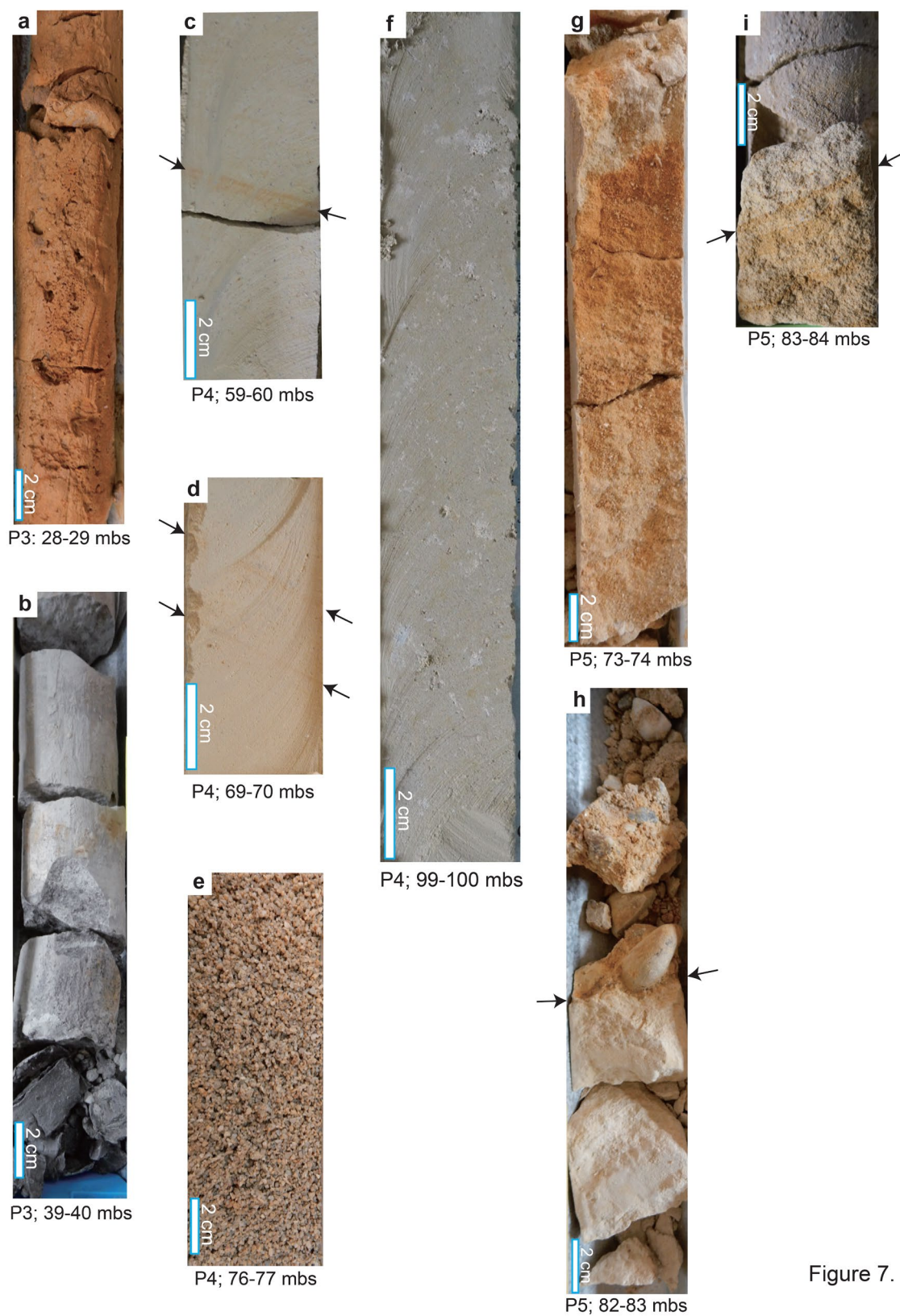


Figure 7.

431

432

433 **Figure 7. Representative features of cores from Bhabsi river Sites P3–P5. Cores in**
434 **each image shallow upward. (a) Brown clay at Site P3; 28–29 mbs. (b) Black organic-**
435 **rich clay at Site P3; 39–40 mbs. (c) Inclined lamina in gleyed silt at Site P4; 59–60**
436 **mbs. (d) Inclined lamina in grayish orange silt at Site P4; 69–70 mbs. (e) Very coarse**
437 **sand at Site P4; 76–77 mbs. (f) Gleyed silt at Site P4; 99–100 mbs. (g) Fine to medium**
438 **sand at Site P5; 73–74 mbs. (h) Erosional contact from silt to gravels recovered at**
439 **Site P5; 82–83 mbs. (i) Inclined laminas in silty sand at Site P5; 83–84 mbs.**

440

441 **4.1.3 Ratu river (Footwall)**

442 **4.1.3.1 Site P6 (26.98673°N, 85.91089°E; total depth of core: 50 mbs)**

443 The upper 15 m of sediments at Site P6 (Fig. 8a) are mostly coarse gravels (16
444 $\text{mm} < d < 256 \text{ mm}$) with silt to coarse sand, representing bedload-dominant channel
445 deposits, assigned as Facies A (Fig. 9a). From 15 mbs, the sediments are finer grained,
446 characterized by silt and fine to coarse sand of Facies B, intercalated with gravels until
447 29 mbs. Below this unit, from 29 mbs to the base of the core at 50 mbs, gravel layers are
448 absent, and the sediments consist of moderately sorted, normally graded silt to medium
449 sand (Figs. 10a–f). Color mottling and oxidized spots are common throughout the core,

450 reflecting pedogenesis and bioturbation.

451 Continuous sub-vertical bedding planes characterize the sediments below 29 mbs,
452 whereas the sediments above dip sub-horizontally (3–25°) (Figs. 8a, 10a–f, 11). The
453 transition occurs around 30–35 mbs, where distinct silt laminas (1–2 mm thick) in well-
454 sorted, indurated sandy silt show an abrupt increase in dip from 30° to 85° (Figs. 10a–e,
455 11). Within this interval, laminas exhibit several variations of decrease and increase in
456 dip, forming multiple open, recumbent folds (Fig. 11). Below this interval, the sandy beds
457 maintain near-vertical dip (~75–90°) (Figs. 10f, 11).

458

459 **4.1.3.2 Site P7** (26.98347°N, 85.91175°E; total depth of core: 100 mbs)

460 The upper 17 m of sediments at Site P7 (Fig. 8b) are mostly coarse gravels (16
461 mm < d < 256 mm) with silt and sand, assigned as Facies A. From 17 to 36 mbs, the
462 sediments become finer grained, consisting of poorly sorted silt with various sand and
463 pebbles intercalated with thin gravels of Facies B. At the bottom of this unit (35–36 mbs),
464 very well sorted, smooth and friable silt suggests aeolian loess. From 36 to 56 mbs, the
465 sediments exhibit mainly coarse gravels, similar to the upper 17 mbs (Facies A) (Fig. 9b).

466 Below this unit (56–100 mbs), the sediments become finer grained, consisting of
467 normally graded cycles of well sorted clayey silt intercalated with poorly sorted silt to

468 coarse sand with gravels of Facies B (Figs. 9c–e, 10g). 1–2-mm-thick laminae in fine sand
469 and silt are inclined ($\sim 15\text{--}45^\circ$) (Figs. 8b, 10g), and occasionally exhibit cross-bedding
470 (dip $5\text{--}40^\circ$) (Fig. 9c).

471 At depths of 66.34–66.42 mbs, distinctive white fine-grained tabular features,
472 identified to be deformation bands, are visible in the middle of a 2-m-thick moderately
473 sorted, medium-coarse grained, massive sand (Fig. 10h–m). The deformation bands are
474 narrow (0.5–3 mm) and cut across the core and inferred shallow bedding (Fig. 10h, i, m).
475 The bands form a conjugate set dipping 70° and 30° , where the high-angle band is cross-
476 cut by the sub-horizontal band (Fig. 10m). Under a microscope, the deformation band is
477 finer-grained than the host sand and lacks the abundant visible porosity of the host
478 immature arkosic sand (Fig. 10j,k,l). Instead, intergranular space is filled mostly by 50–
479 $100\ \mu\text{m}$ angular grains and clay material (Fig. 10k,l). Beneath this interval, sediment
480 lithification continues to increase downhole, as evident in massive gleyed clayey silt
481 below 82 mbs (Fig. 9e) and lithified conglomerates at 95–99 mbs (Fig. 9d).

482

483 **4.1.3.3 Site P8** (26.97999°N, 85.90928°E; total depth of core: 47 mbs)

484 The upper 18 m of sediments at Site P8 (Fig. 8c) are mostly coarse gravels (16
485 $\text{mm} < d < 256\ \text{mm}$) with silt to coarse sand, assigned as Facies A. From 18 to 35 mbs, the

486 sediments are finer grained, consisting of moderately to poorly sorted silt with sand and
487 pebbles, intercalated with thin gravels assigned as Facies B (Fig. 9f). Organic-rich black-
488 brown sandy silt at 19 and 21 mbs is notable. The sediments are generally massive, with
489 several sub-horizontal laminas observed in well sorted silt towards the bottom of the unit
490 (32–35 mbs), possibly representing floodplain deposits or loess (Fig. 9f). These laminas
491 and bedding planes dip 5°–15° (Fig. 8c). From 35 to 47 mbs (base of core), the sediments
492 are mainly coarse gravels of Facies A, similar to the upper 18 mbs.

493

494 **4.1.3.4 Site P9** (26.97883°N, 85.90906°E; total depth of core: 96 mbs)

495 The upper 28 m of sediments at Site P9 (Fig. 8d) are mostly coarse gravels (16
496 mm < d < 256 mm) with silt to coarse sand, representing Facies A. From 28 to 41 mbs,
497 sediments become finer grained, consisting of poorly sorted silt to sand with gravels
498 intercalated with well sorted clayey silt, suggesting the channel/floodplain environment
499 of Facies B. The sediments are generally massive and normally graded, with some sub-
500 horizontal wavy laminas in silt at 32–33 mbs (Fig. 9g). Bedding dips 5°–30° (Fig. 8d).
501 Thin layers of organic rich, brown clayey silt also characterize this unit. Color mottling,
502 oxidized spots and irregular layers are present in the fine sediments. At the bottom of this
503 unit, well sorted silt to clay is present (39–41 mbs), with a particularly friable silt at 40–

504 41 mbs, which is likely aeolian loess. Beneath this unit, from 41 mbs to the base of the
505 core at 96 mbs, the sediments are mainly coarse gravels of Facies A, similar to the upper
506 28 mbs (Fig. 9h).

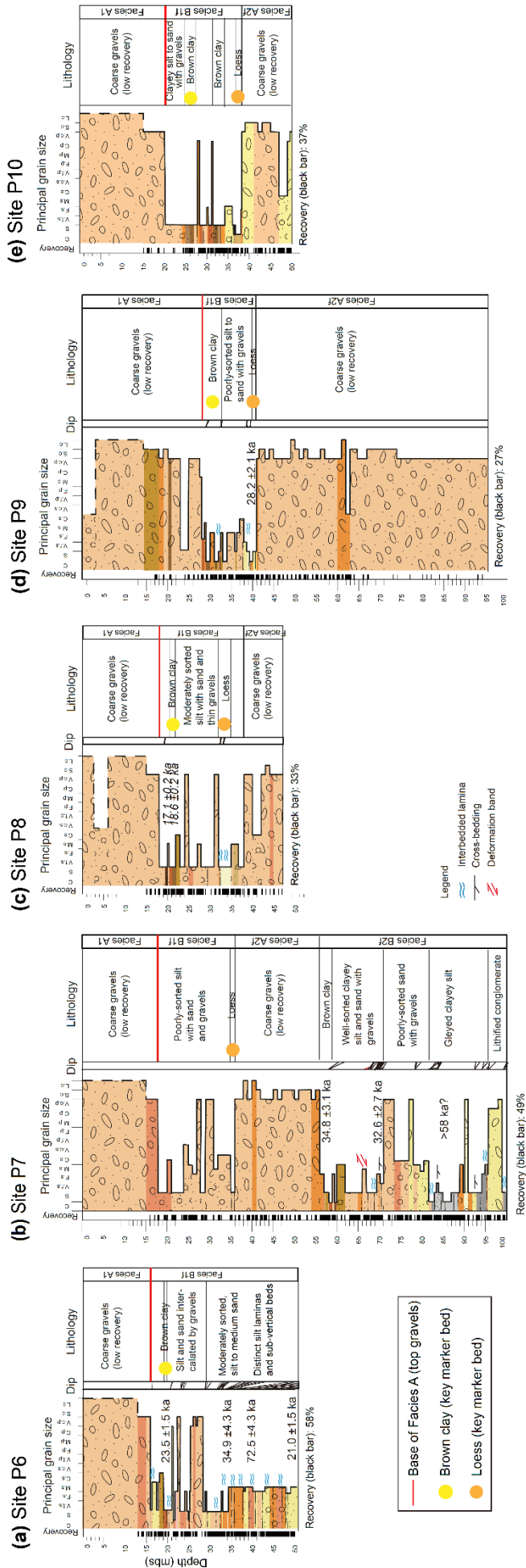
507

508 **4.1.3.5 Site P10** (26.97794°N, 85.90878°E; total depth of core: 50 mbs)

509 The upper 20 m of sediments at Site P10 (Fig. 8e) are mostly coarse gravels (16
510 mm < d < 256 mm) with silt to coarse sand, representing Facies A. From 20 to 38 mbs,
511 the sediments are finer grained, consisting of well sorted clayey silt intercalated with
512 poorly sorted silt to sand with pebbles and thin gravel layers, assigned as Facies B.
513 Intervals of organic-rich dark brown clayey silt are also distinct (Fig. 9i). Towards the
514 bottom of this unit (36–38 mbs), well sorted, friable to earthy-hard silty clay, possibly
515 aeolian loess, is present. The sediments are generally massive, and color mottling with
516 oxidized spots and organic matter is common. Beneath this unit, from 38 to 50 mbs (base
517 of core), the sediments are mainly coarse gravels of Facies A, similar to the upper 25 m.

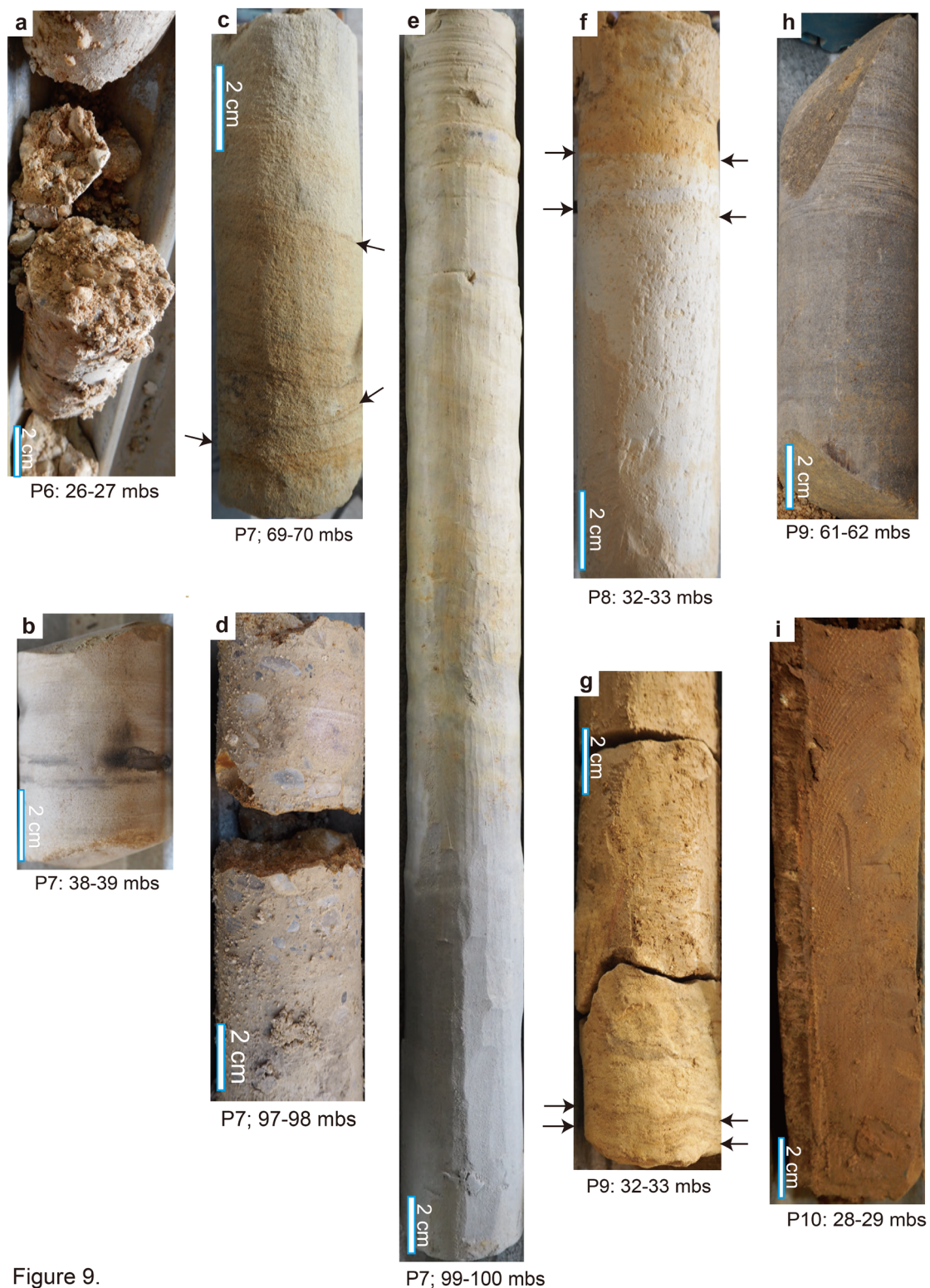
518

519



520 **Figure 8. Graphic sedimentary core logs for the Ratu river sites (a) P6, (b) P7, (c)**
521 **P8, (d) P9, and (e) P10 showing principal grain size, sediment color, dip angles, and**
522 **description of lithology. Black bars are recovered core. Symbols next to core log are**
523 **described in legend below. Dating results are for OSL and radiocarbon (*italic*) ages**
524 **(also shown in Tables 1 and 2). Measured dip angles are shown as tilted lines. Facies**
525 **A and B are interpreted facies (see Section 4.2 for details). Red line marks the base**
526 **of top gravels (Facies A1). Brown clay (yellow dots) and loess (orange dots) are key**
527 **beds traced in Fig. 15.**

528



529

Figure 9.

530

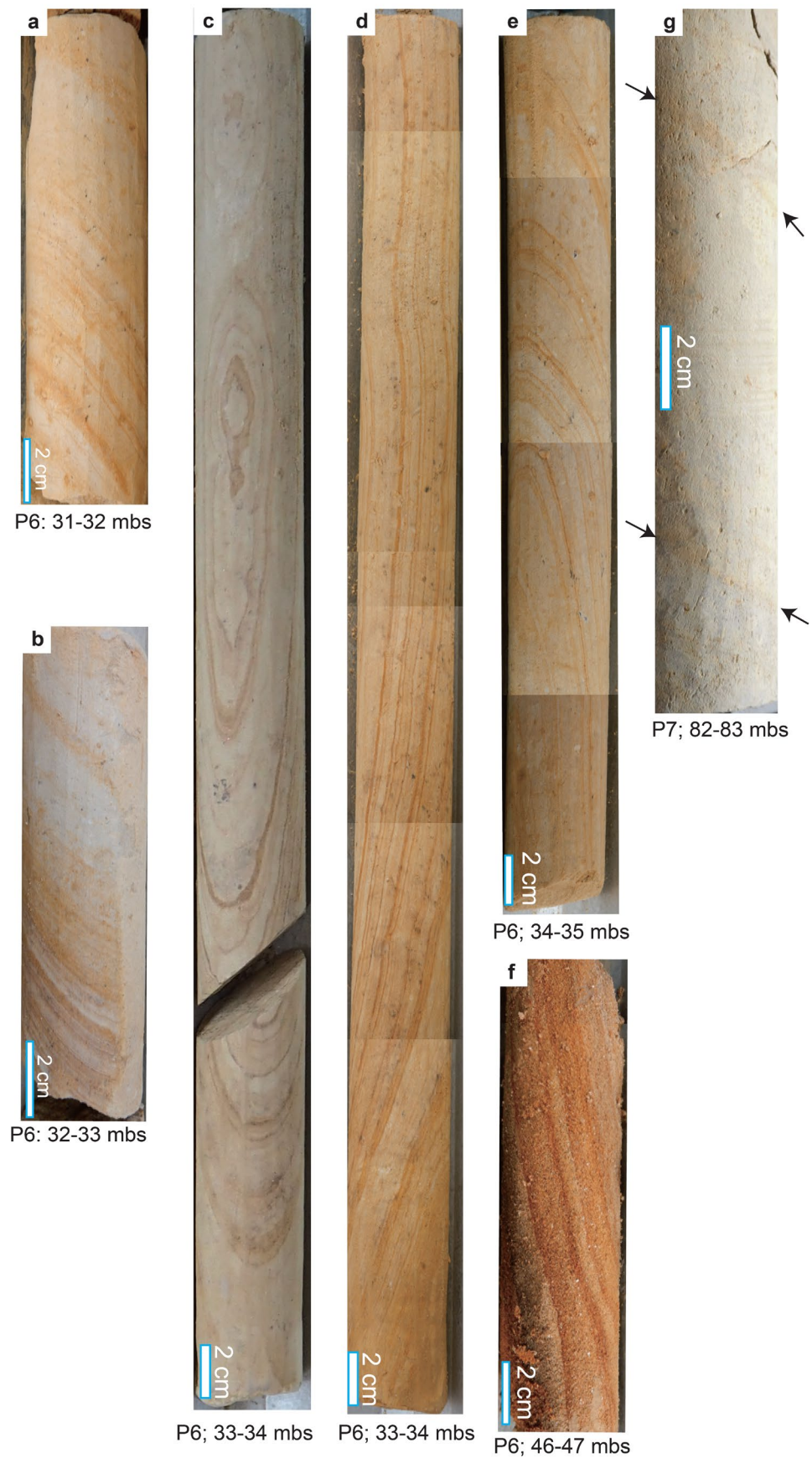
Figure 9. Representative features of cores for the Ratu river sites P6–P10. Cores in

531

each image shallow upward. (a) Gravels with matrix of sand and silt at Site P6; 26–

532 **27 mbs. (b) Large cobble of quartzite at Site P7; 38–39 mbs. (c) Cross-bedding in**
533 **silty fine sand at Site P7; 69–70 mbs. (d) Lithified conglomerate at Site P7; 97–98**
534 **mbs. (e) Grayish orange silt transitioning into gray silt at Site P7; 99–100 mbs. (f)**
535 **Sub-horizontal laminas in silt at Site P8; 32–33 mbs. (g) Sub-horizontal laminas in**
536 **silt at Site P9; 32–33 mbs. (h) Large cobble of sandstone at Site P9; 61–62 mbs. (i)**
537 **Brown clay at Site P10; 28–29 mbs.**

538



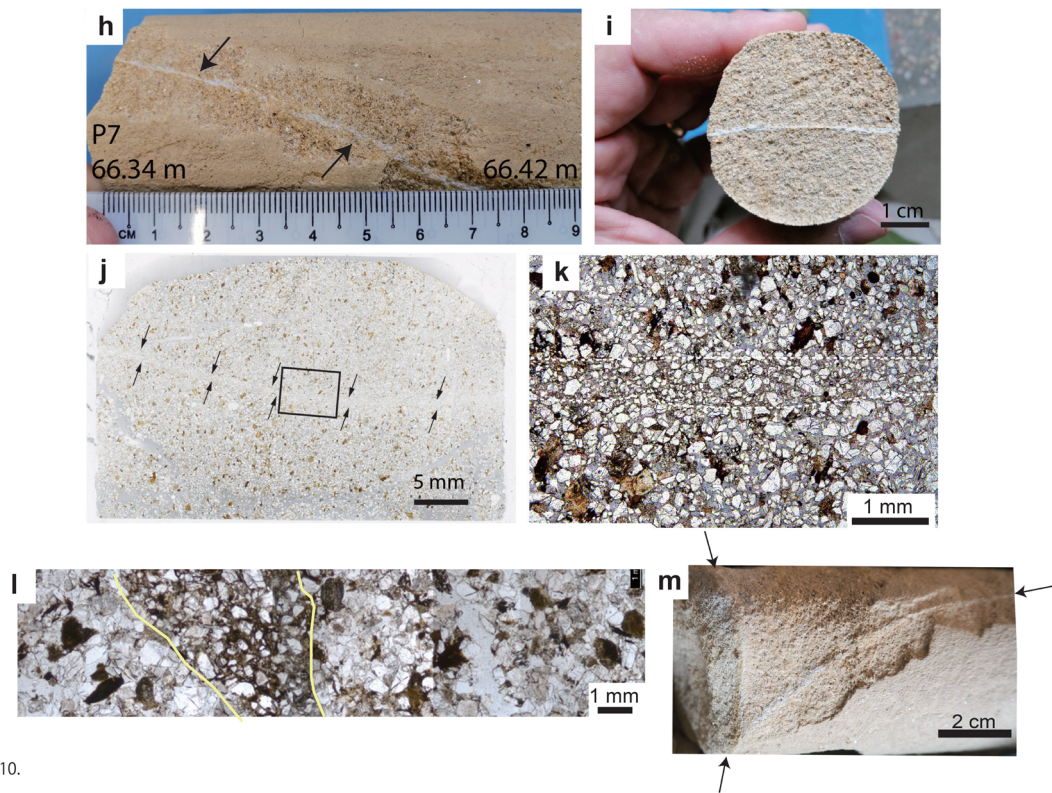


Figure 10.

540

541 **Figure 10. High-angle bedding and deformation band observed at Sites P6 and P7.**

542 **Cores in each image shallow upward. (a) Inclined laminas in silt at Site P6; 31–32**

543 **mbs. (b) Inclined laminas in silt at Site P6; 32–33 mbs. (c) Near-vertically dipped**

544 **laminas in silt at Site P6; 33–34 mbs. (d) Same core as (c). (e) Inclined laminas in silt**

545 **exhibiting gradual increase in dip with depth at Site P6; 34–35 mbs. (f) Near-**

546 **vertically dipped laminas in medium sand at Site P6; 46–47 mbs. (g) Inclined**

547 **laminas in silt at Site P7; 82–83 mbs. (h) Deformation band observed in medium-**

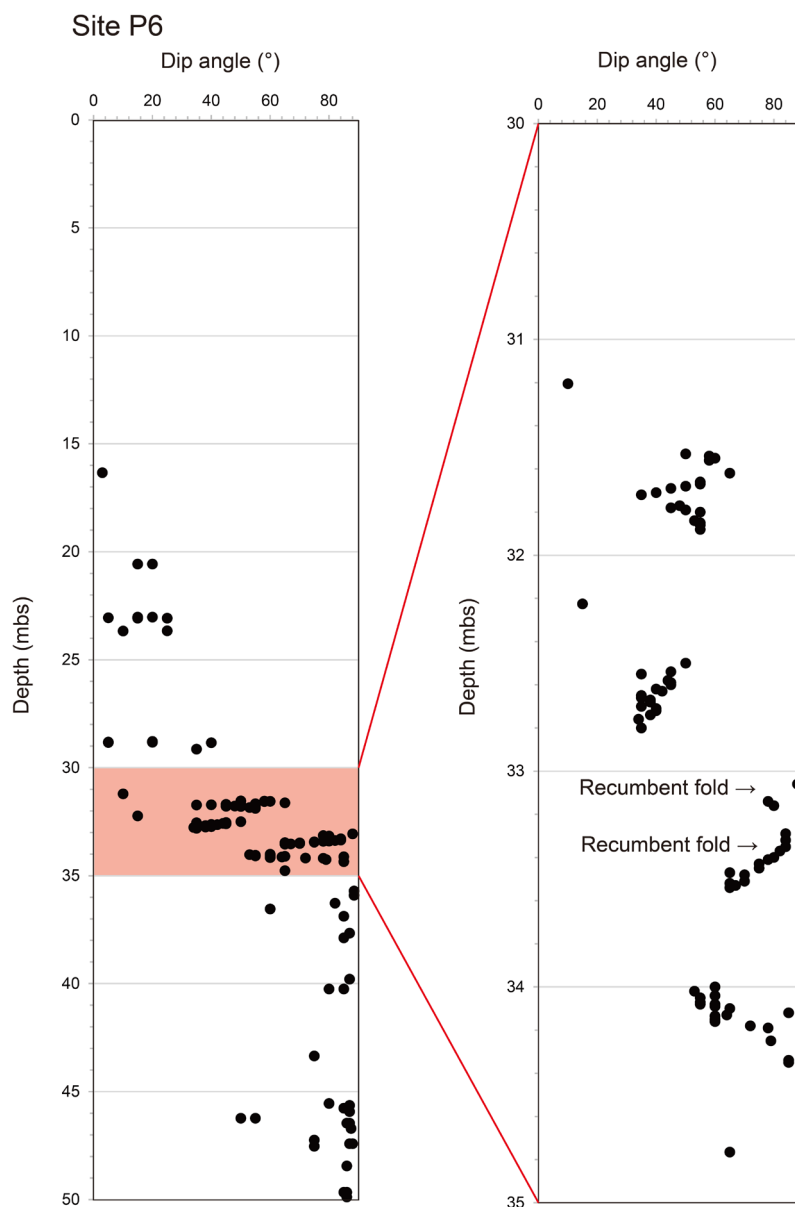
548 **coarse sand at Site P7; 66.34–66.5 mbs. Deformation band is white (marked by**

549 **arrows), and dip is steep. (i) Same core as (h), viewed uphole at 66.35 mbs. (j) High-**

550 **resolution scan of thin section of core cut perpendicular to plane of deformation**

551 **band. Section epoxy is stained weakly blue to show porosity. Note finer grain size**
552 **and whiter color of deformation band (arrows) relative to matrix. White box show**
553 **area of (k). (k) Plane polarized photomicrograph of inset box shown in (j). Epoxy is**
554 **stained light blue to show porosity. Note porosity reduction and grain size reduction**
555 **within deformation band (central region highlighted with dashed lines). (l) Close-up**
556 **of plane polarized photomicrograph of deformation band without epoxy from**
557 **another thin section. Yellow line marks the top and bottom of the deformation band.**
558 **(m) Deformation bands observed in conjugate set. Same location as (h).**

559



560

561 **Figure 11. Distribution of dip angles measured at Site P6. The right panel shows**

562 **close-up of 30–35 mbs, shaded in red in the left panel. Two recumbent folds are**

563 **identified between 33–33.6 mbs, owing to continuous core recovery (see Figs. 9c,d).**

564

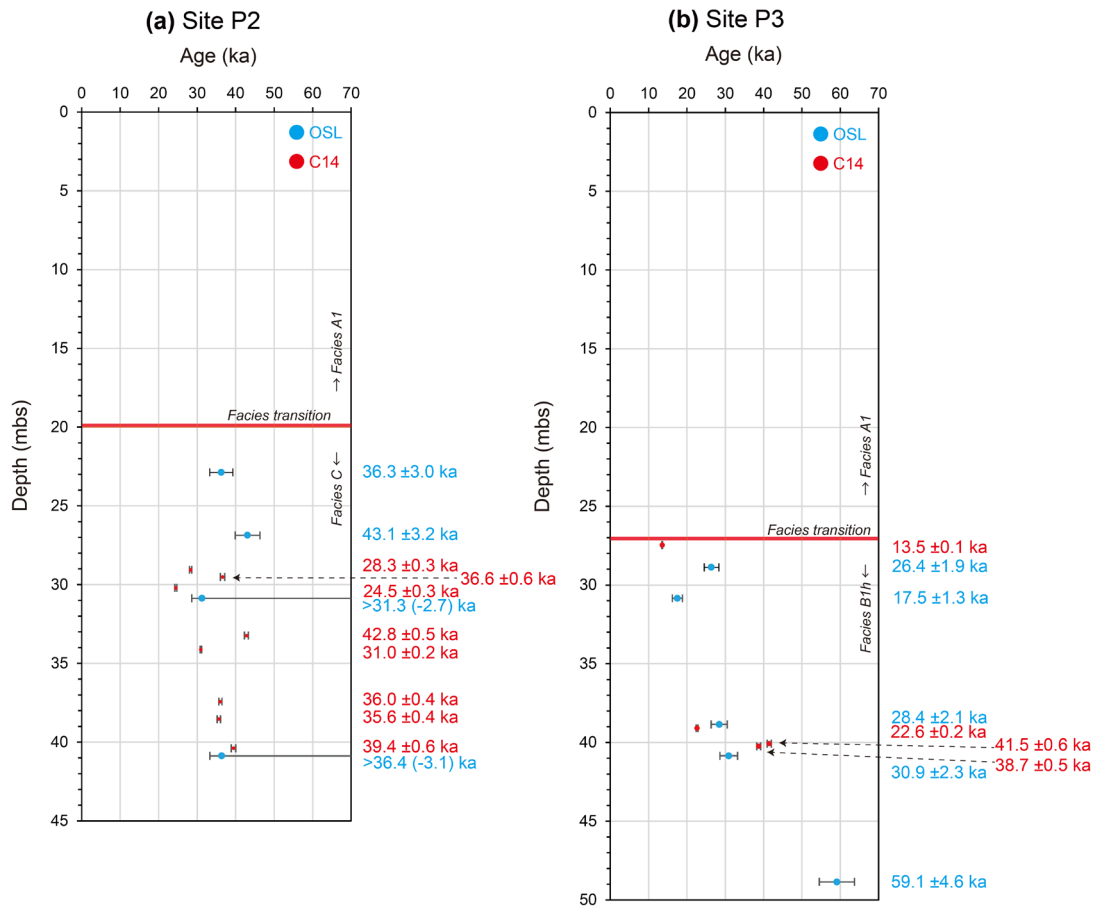
565 **4.2. Sediment ages, marker beds, and timing of facies transitions**

566 Sediment ages from Sites P2–P4 and P6–P9 were determined from 18 samples by
567 OSL dating and 14 samples by ^{14}C dating (Figs. 4, 6, 12, Tables 1, 2). The ages span from
568 13.5 ± 0.1 to 72.5 ± 4.3 ka. Based on our stratigraphic observations (Section 4.1) and the
569 recovered ages, we infer the timing of facies transitions. Despite the variations in
570 deposition and sediment thickness observed in each river, we are able to correlate the
571 major facies transitions among them. We also identify several key lithologies that can be
572 correlated across the different sites and across different rivers: brown clay, gleyed clay/silt,
573 and well-sorted aeolian silt (loess). Together, this information is used to construct a
574 regional cross-section and timing of events in Section 5.

575 Figure 12 shows the ^{14}C and OSL ages at Sites P2 and P3. The overall ranges of
576 ages obtained by the two methods are similar (Fig. 12). However, there is a wide scatter
577 in dates that cannot be explained by the reported uncertainties from either method. This
578 may be related to specific challenges associated with each dating method, such as
579 reworking of organic material, and partial bleaching and/or saturation (all OSL electron
580 traps have become filled, and no further charge is trapped in the sample) of quartz sands.
581 For example, the gleyed clay at 40 mbs at Site P3 yielded older ^{14}C ages (38.7–41.5 ka)
582 than the OSL data both above and below (30.9 ± 2.3 ka) (Figs. 6a, 12b). This could be

583 explained by the clay containing reworked old residual carbon (e.g., Wu et al., 2011;
 584 Reuther et al., 2017). Due to this possibility, we prefer the OSL age over the ^{14}C age for
 585 this section, since the OSL ages are internally consistent. We also note that the OSL ages
 586 obtained at 30.9 mbs and 40.9 mbs are >31.3 and >36.4 ka, respectively, at Site P2
 587 represent lower limits (Fig. 12a), since the OSL responses for the obtained equivalent
 588 doses are approaching saturation and reaching the limit of detection; these ages therefore
 589 have infinite positive error bars (Supporting Information Fig. S5).

590



592 **Figure 12. Sediment ages from Sites P2 and P3 (also see Tables 1, 2). Blue dots: OSL**
593 **dating. Red dots: ^{14}C dating. Age values are given next to each data point (blue:**
594 **OSL, red: ^{14}C). Orange line marks the lithologic base of Facies A1 (see Figs. 3 and**
595 **5). Error bars for OSL include dose rate errors and uncertainty for equivalent dose.**
596 **Error bars for ^{14}C are 1σ counting statistics. (a) Site P2. (b) Site P3.**

597

598 The first marker bed is the brown clay in Facies B, which is observed both in the
599 hanging wall (28 mbs at Site P3 and 50 mbs at Site P4) and in the footwall (20–30 mbs
600 at Sites P6–P10), and has a sediment age of 17.5–26.4 ka (Figs. 6, 8). In the hanging wall,
601 the brown clay is dated between 13.5–26.4 ka (Site P3, ^{14}C and OSL ages above and
602 below) and 24.1 ± 3.2 ka (Site P4, OSL) (Fig. 6; Tables 1, 2). In the footwall, the brown
603 clay is dated at 23.5 ± 1.5 ka (Site P6, OSL) and 17.1 ± 0.2 to 18.6 ± 0.2 ka (Site P8, ^{14}C)
604 (Fig. 8; Tables 1, 2).

605 The second marker bed is the gleyed clay in Facies B in the hanging wall, identified
606 at 39–40 mbs at Site P3, 80–85 mbs at Site P4, and 86–90 mbs at Site P5 (Fig. 6). The
607 gleyed clay is dated at 30.9 ± 2.3 ka (Site P3, OSL) and between 26.9 and 35.8 ka (Site P4,
608 OSL ages above and below) (Fig. 6; Table 2).

609 The third marker bed is the loess in the footwall, identified at 35–36 mbs at Site P7,

610 32–35 mbs at Site P8, 39–41 mbs at Site P9, and 36–38 mbs at Site P10 (Fig. 8; Section
611 4.1). This loess is dated at 28.2 ± 2.1 ka by OSL methods at Site P9 (Fig. 8; Table 2).

612 The obtained sediment ages also constrain the timing of the observed facies
613 transitions (Section 4.1). The youngest and clearest facies transition that we identify
614 occurs between the upper Facies A, which encompasses the upper part in all boreholes,
615 and the Facies B section beneath it (observed in all but Site P2, which has Facies C below
616 Facies A). Here, we name the upper Facies A that is common in all boreholes as “Facies
617 A1,” and the Facies B below Facies A1 as “Facies B1h” and “Facies B1f” in the hanging
618 wall and footwall of the Bardibas thrust, respectively (Figs. 4, 6, 8). We do not have any
619 dates from Facies A1 as it is not suitable for dating (coarse gravels with very low
620 recovery), but the nearest sample below the facies transition is obtained at 27 mbs at Site
621 P3 and has an age of 13.5 ± 0.1 ka (^{14}C); this represents a maximum age for the transition
622 into Facies A1 (Fig. 12b).

623 The facies transition at Site P2, from Facies C (lacustrine) below to Facies A1
624 above, is poorly dated. However, within Facies C at this site, we dated eight samples by
625 ^{14}C and four by OSL methods (Fig. 12a). The ages are scattered and do not exhibit a
626 strong relationship with depth, but in general range from 24.5 ± 0.3 to 43.1 ± 3.2 ka (Fig.
627 4b, 12a, Tables 1, 2); these sediments are older than the Facies A/B transition (13.5 ± 0.1

628 ka) estimated at Site P3.

629 The base of Facies B1, which is buried beneath Facies A1, is best observed in the
630 footwall. At Sites P7–P10, the base of Facies B1f is marked by the loess marker bed
631 (28.2 ± 2.1 ka), and we consider this age to represent the timing of this transition (Fig. 8).
632 Beneath this unit at these sites, we observe a coarse-grained sequence assigned as Facies
633 A and an underlying fine-grained sequence of Facies B in the footwall (Sites P7–P10).
634 Here we name these second sequences of Facies A and B in the footwall as “Facies A2f”
635 and “Facies B2f”, respectively (Figs. 4, 6, 8). At Site P7, we obtained an OSL age of
636 34.8 ± 3.1 ka at the base of Facies A2f at 56.6 mbs, and 32.6 ± 2.7 ka at 70.9 mbs within
637 Facies B2f (Fig. 8; Table 2). Below this depth, age constraints are poor: we have an
638 estimate age of >58 ka at 85 mbs at Site P7 by OSL, but we are reluctant to use this age
639 as there were not sufficient quartz aliquots for this sample (only 8; Table 2). At Site P6,
640 OSL ages of Facies B1f at 30–50 mbs include some older ages than Facies B1f at Sites
641 P7–P10, ranging from 21.0 to 72.5 ka (Fig. 8, Table 2). The large scatter in ages at Site
642 P6 may be due to disturbance by the deformation that produced the sub-vertical beds
643 ($\sim 75^\circ$ – 90°) that characterize this section below 29 mbs (Fig. 11).

644 These deeper facies transitions recorded in the footwall (associated with Facies A2f
645 and B2f) are not well observed in the hanging wall (Sites P1–P5), despite the fact that the

646 dated ages show that the sediments cover the same age range (Figs. 4, 6, 8). In particular,
 647 the deep sediments of Facies B1h (59.1 ± 4.6 ka; Site P3) and Facies C (43.1 ± 3.2 ka; Site
 648 P2) in the hanging wall are older than the base of Facies B1f (28.2 ± 2.1 ka; Site P9) in the
 649 footwall (Figs. 4, 6, 8; Table 2). This may be the result of different facies being active in
 650 different locations; alternatively, some sedimentary sections may not be preserved in the
 651 hanging wall due to different rates of uplift/subsidence, and/or there could be poor
 652 recovery of some sections in the hanging wall. It is likely that Facies B1h corresponds to
 653 both Facies B1f and B2f, with a missing or very thin or poorly recovered section of Facies
 654 A2f in between (Figs 4, 6, 8).

655

Table 1

Site	Depth (mbs)	Lithology	Dated material	Conventional radiocarbon age (ka) (1σ)	Calendar calibrated age (ka) (higher probability)*	Calendar calibrated age (ka) (lower probability)**	Stable isotope $\delta^{13}C$ (‰)	Carbon content (%)
P2	29.05-29.07	Brown silt	Organic sediment	24.26 ± 0.09	28.600 - 28.005	28.459 - 28.150	-14.4	0.27
P2	29.5-29.54	Gray silty clay	Organic sediment	32.59 ± 0.19	37.144 - 36.023	36.714 - 36.243	-17	0.19
P2	30.2-30.21	Gray clay	Organic sediment	20.36 ± 0.06	24.751 - 24.202	24.544 - 24.327	-16.9	0.09
P2	33.23-33.24	Black silty clay	Organic sediment	38.87 ± 0.36	43.323 - 42.272	43.027 - 42.516	-11	1.2
P2	34.1-34.15	Black silt	Organic sediment	26.81 ± 0.11	31.147 - 30.762	31.061 - 30.865	-13.2	0.5
P2	37.42-37.43	Dark gray medium sand	Organic sediment	32.15 ± 0.18	36.428 - 35.617	36.260 - 35.850	-13.6	0.5
P2	38.53-38.55	Black silt	Organic sediment	31.75 ± 0.17	36.092 - 35.201	35.888 - 35.426	-13.6	0.3
P2	40.37-40.4	Black silt	Organic sediment	34.91 ± 0.24	40.038 - 38.826	39.745 - 39.110	-12.5	0.4
P3	27.45-27.48	Gray silty sand	Organic sediment	11.72 ± 0.04	13.615 - 13.442	13.703 - 13.681	-17.7	0.2
P3	39.09-39.1	Grayish orange silt	Organic sediment	18.76 ± 0.06	22.830 - 22.434	22.693 - 22.491	-18.2	0.07
P3	40-40.15	Black clay	Organic sediment	36.9 ± 0.31	42.016 - 40.904	41.775 - 41.236	-13.3	1.4
P3	40.23-40.25	Gray silt	Organic sediment	34.16 ± 0.22	39.213 - 38.216	38.870 - 38.435	-14.7	0.3
P8	19.82-19.87	Brown silt	Organic sediment	14.06 ± 0.04	17.330 - 16.882	17.185 - 16.996	-11.4	0.52
P8	21.47-21.49	Brown silt	Organic sediment	15.34 ± 0.06	18.765 - 18.462	18.700 - 18.547	-12.3	1.62

Calibration of the conventional age were performed using the INTCAL13 (2013 calibration databases) (Reimer et al. 2013), high probability density range method and Bayesian probability analysis (Ramsey, 2009). For sediment age, we use the higher probability calendar-calibrated age.

* 95.4% probability density range for all samples except for P3 27.45-27.48 mbsf, which is 94.1% probability.

** 68.2% probability density range for all samples except for P3 27.45-27.48 mbsf, which is 1.3%.

657 **Table 1. Summary of radiocarbon dating results from Sites P2–P8 showing sample**
658 **location, lithology, dated material, conventional radiocarbon age, calendar**
659 **calibrated age, $\delta^{13}\text{C}$ (‰), and carbon content. See more details in Supporting**
660 **Information Text S2.**

661

Table 2.

Site	Depth (mbs)	Lithology	U ^a (ppm)	Th ^a (ppm)	K ^a (%)	Rb ^a (ppm)	Cosmic ^{b,c} (Gy/ka)	Dose-rate ^{b,c,d} (Gy/ka)	n ^e	Average equivalent dose ^f (Gy)	Weighted average equivalent dose ^f (Gy)	2-mixed model equivalent dose ^f (Gy)	Average OSL Age ^{g,h} (ka)	Weighted average OSL Age ^{h,i} (ka)	2-mixing model OSL Age ^{h,i,j} (ka)
P2	22.75-23	Silt with fine sand	3.4	19.5	1.62	42	0.026±0.003	3.44±0.20	30(60)	124.8±7.3	102.0±1.9	99.2±2.0	36.3±3.0	29.6±1.8	28.8±1.8
									[6]			(21%)			
P2	26.75-27	Silt with medium sand	3.9	17.4	1.44	182	0.021±0.002	3.24±0.19	26(60)	139.5±6.3	114.07±2.6	99.0±3.5	43.1±3.2	35.2±2.2	30.6±2.1
									[13]			(19%)			
P2	30.75-31	Clayey silt with very fine sand	4.4	20.2	1.68	42	0.017±0.002	3.73±0.22	14(48)	>116.9±7.2	>101.3±5.1	107.6±5.7	>31.3±2.7	>27.2±2.1	28.8±2.3
									[14]			(6%)			
P2	40.75-41	Silt with fine sand	4.1	18.5	1.54	175	0.011±0.001	3.43±0.20	15(48)	>124.9±7.8	>93.9±3.6	78.6±4.5	>36.4±3.1	>27.4±1.9	22.9±1.9
									[13]			(24%)			
P3	28.75-29	Clay	4.6	16.7	1.39	138	0.019±0.002	3.29±0.20	25(60)	183.3±19.1	102.5±3.0	86.9±3.5	55.7±6.7	31.2±2.1	26.4±1.9
									[7]			(35%)			
P3	30.7-31	Silt	3.9	17.7	2.20	155	0.02±0.002	3.94±0.24	34 (29)	133.84±9.1	79.9±1.8	69.1±2.6	34.0±3.1	20.3±1.3	17.5±1.3
									[70]			(34%)			
P3	38.7-39	Silt with very fine sand	5.6	15.0	2.04	135	0.02±0.002	3.98±0.24	10 (2)	113.0±5.0	104.2±3.7	73.7±2.9	28.4±2.13	26.2±1.8	
									[32]			(11%)			
P3	40.7-41	Gleyed silt with fine sand	3.6	16.8	1.53	97	0.02±0.002	3.21±0.19	30 (4)	175.1±12.1	119.9±3.0	98.9±4.2	54.6±5.0	37.4±2.4	30.9±2.3
									[52]			(36%)			
P3	48.7-49	Medium sand with silt	4.3	17.0	2.13	141	0.02±0.002	3.91±0.24	39 (11)	231.2±11.1	193.4±3.9	186.6±5.0	59.1±4.6	49.5±3.2	47.7±3.2
									[58]			(21%)			
P4	50.75-51	Brown silt	3.7	15.9	1.32	163	0.007±0.001	2.98±0.18	18(48)	128.1±9.3	94.2±3.6	71.9±8.5	43.0±4.1	31.6±2.3	24.1±3.2
									[10]			(26%)			
P4	69.75-70	Silt with fine sand	4.7	22.1	1.83	146	0.004±0.000	4.04±0.24	22(48)	185.8±13.0	143.69±4.0	108.8±5.9	46.0±4.2	35.6±2.3	26.9±2.2
									[18]			(28%)			
P4	99.75-100	Clayey silt	3	16.4	1.36	120	0.002±0.000	2.90±0.17	26(48)	103.8±7.5	86.0±1.4	89.5±1.4	35.8±3.3	29.6±1.8	30.9±1.9
									[2]			(14%)			
P6	19.75-20	Brown clayey silt	2.2	11	0.91	123	0.034±0.003	2.02±0.12	26(48)	62.9±3.9	53.0±0.7	47.4±0.93	31.1±2.7	26.2±1.6	23.5±1.5
									[0]			(29%)			
P6	33.75-34	Silt with fine sand	3.2	14.5	1.20	131	0.015±0.002	2.69±0.16	11(48)	93.8±10.1	85.4±3.0	51.0±6.4	34.9±4.3	31.7±2.2	19.0±2.6
									[11]			(24%)			
P6	39-39.25	Fine to medium sand	1.9	9.3	0.77	100	0.012±0.001	1.70±0.10	10(16)	164.0±17.8	129.67±4.7	123.3±6.0	96.4±11.9	76.3±5.3	72.5±4.3
									[6]			(27%)			
P6	49.75-50	Fine to medium sand with silt	2.1	11.1	0.92	123	0.008±0.001	1.98±0.12	54(76)	80.0±4.3	47.9±0.7	41.5±1.7	40.4±3.3	24.2±1.5	21.0±1.5
									[1]			(34%)			
P7	56.5-56.75	Fine sand with silt	3.3	16.4	1.36	98	0.006±0.001	2.97±0.18	18(48)	103.3±6.6	89.4±2.4	78.0±3.9	34.8±3.1	30.1±2.0	26.3±2.1
									[16]			(24%)			
P7	70.75-71	Silt to fine sand	3.2	15.5	1.29	103	0.004±0.000	2.81±0.17	32(48)	91.6±5.2	74.1±1.2	74.6±1.3	32.6±2.7	26.4±1.6	26.5±1.6
									[6]			(25%)			
P7	84.75-85	Silt	3.1	15.5	1.29	175	0.003±0.000	2.79±0.17	8	>150			> 58		
P7	99.75-100	Silt	5.9	17.7	1.47	106	0.002±0.000	3.68±0.22		No quartz					
P9	31.75-32	Clay	2.4	14.8	1.23	113	0.016±0.002	2.57±0.15		No quartz					
P9	40.75-41	Silt	2.2	12.4	1.03	108	0.011±0.001	2.19±0.13	27(48)	61.8±2.9	53.1±0.9	46.4±1.5	28.2±2.1	24.3±1.5	21.2±1.4
									[3]			(22%)			

^a Elemental concentrations from ICP-MS of whole sediment measured at Activation Laboratories Limited Ancaster, Ontario Canada.

^b Estimated fractional day water content for whole sediment is taken as 10% and with an uncertainty of ± 5%.

^c Estimated contribution to dose-rate from cosmic rays calculated according to Prescott and Hutton (1994). Uncertainty taken as ±10%.

^d Total dose-rate from beta, gamma and cosmic components. Beta attenuation factors for U, Th and K compositions incorporating grain size factors from Mejdahl (1979). Beta attenuation factor for Rb is taken as 0.75 (cf. Adamiec and Aitken, 1998). Factors utilized to convert elemental concentrations to beta and gamma dose rates from Adamiec and Aitken (1998) and beta and gamma components attenuated for moisture content. Dose rates calculation was confirmed using the Dose Rate and Age Calculator (DRAC) of Duncan et al. (2015).

^e Number of replicated equivalent dose (D_e) estimates used to calculate D_e. These are based on recuperation error of < 10%. Number in parentheses is the number of saturated aliquots. The number in the square parentheses is the total measurements made including failed runs with unusable data.

^f Average equivalent dose (D_e) determined from replicated single-aliquot regenerative-dose (SAR; Murray and Wintle, 2000) runs. The uncertainty is the standard error and includes an uncertainty from beta source estimated of ±2.5%.

^g Weighted average equivalent dose (D_e) determined from replicated single-aliquot regenerative-dose (SAR; Murray and Wintle, 2000) runs. The uncertainty is the standard error and includes an uncertainty from beta source estimated of ±2.5%.

^h Age based on minimum population in 2-mixing model using the program of Vermeesch (2009). Values in parentheses are the dispersion of the aliquots.

ⁱ Uncertainty incorporate all random and systematic errors, including dose rates errors and uncertainty for the D_e.

In this study, we use average OSL ages for samples that showed ≤ 25% dispersion of the aliquots, and 2-mixing model OSL ages for samples that yielded > 25% dispersion. Preferred ages are highlighted in bold.

663 **Table 2. Summary of OSL dating results from Sites P2, P3, P4, P6, P7 and P9**
664 **showing sample location, lithology, radioisotope concentration, moisture contents,**
665 **total dose rates, equivalent dose estimates and optical ages. Dose rate and age**
666 **calculations follow the details indicated in the footnote. See more details in**
667 **Supporting Information Text S1.**

668

669 **5. Discussion**

670 **5.1. Shallow structure of the Bardibas thrust**

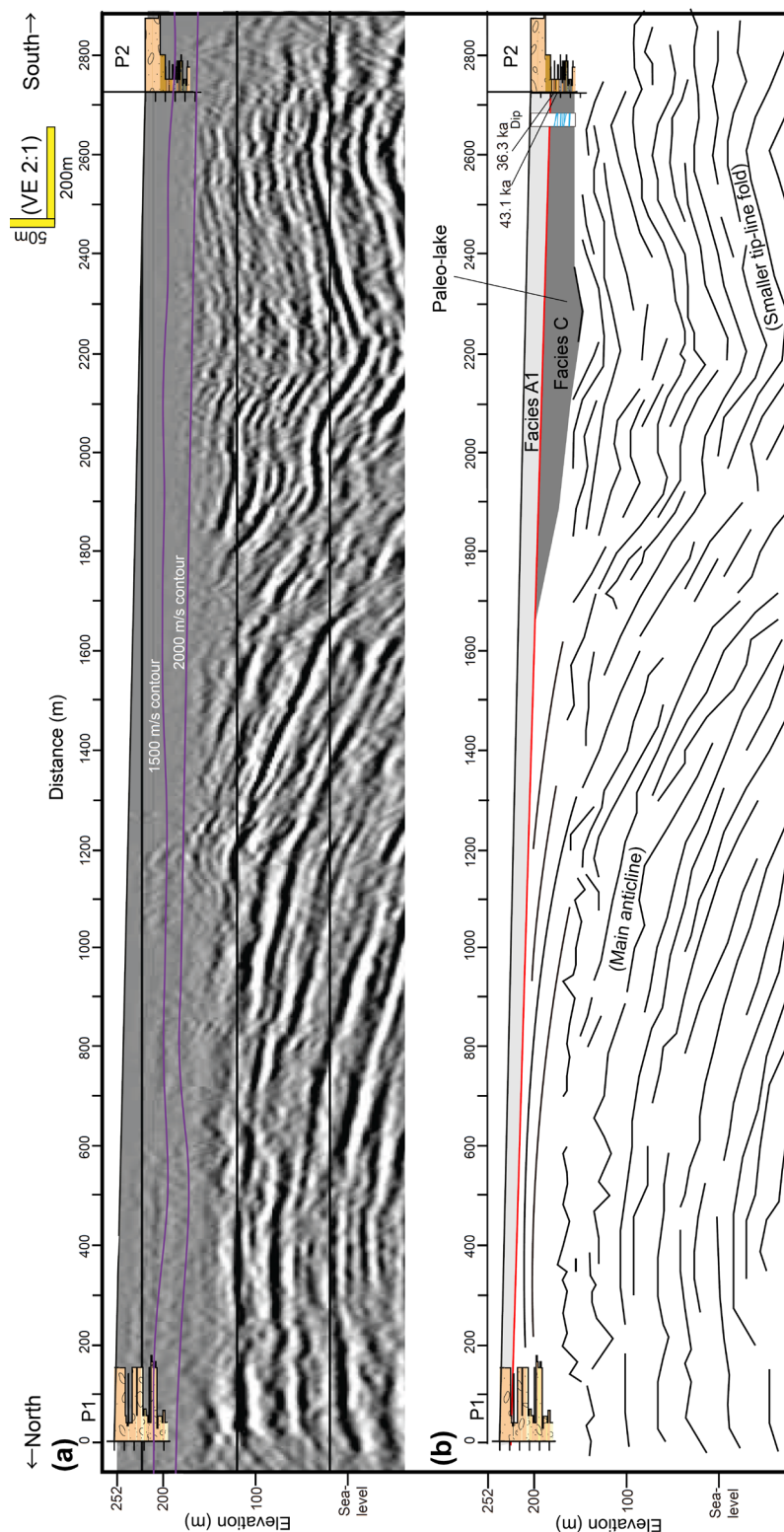
671 The Bardibas thrust is characterized by a hanging wall anticline composed of
672 Siwaliks bedrock beveled by erosion and buried by ~100 m of more recent sediments (Fig.
673 3). Sediment cores in this study reveal that a ~15–68-m-thick gravel sequence (Facies A1)
674 was deposited during the latest Pleistocene to Holocene, capping both the hanging wall
675 and footwall (Section 4.1). Near the fault tip, displacement by the thrust is accommodated
676 by a tip-line fold or fault-propagation fold, deforming the syntectonic strata in the
677 footwall (Fig. 3a).

678 We construct cross-sections across the Bardibas thrust by placing the boreholes
679 presented here onto the seismic profiles of Almeida et al. (2018; and unpublished data;

680 Figs. 13–15). We also compare our data with the refraction velocity models of Liu et al.
681 (2020), which were developed from the same raw data as the seismic profiles of Almeida
682 et al. (2018; Figs. 3b, 16). We first document the shallow structures surrounding the
683 hanging wall anticline beneath the Lakshmi and Bhabsi rivers, using the stratigraphy from
684 Sites P1–P5. We then constrain the shallow structures around the fault tip and growth
685 strata in the footwall beneath the Ratu river, using the stratigraphy from Sites P6–P10.
686 These comparisons, together with sediment ages, allow us to infer the shortening of the
687 hanging wall anticline, and the uplift of the hanging wall of the Bardibas thrust relative
688 to the footwall.

689

690



691

692 **Figure 13. Lakshmi river cross-section. (a) Graphic sedimentary core logs of Sites**

693 **P1 and P2 placed in seismic reflection profile of Almeida et al. (unpublished data).**

694 **Vertical exaggeration=2:1. (b) Interpretation of (a) with colored Facies A1 (light**
695 **gray) and Facies C (dark gray). Red line marks the base Facies A1. Measured dip**
696 **angles from the cores at Site P2 are shown in blue bars, vertically exaggerated (2:1).**
697 **Representative ages obtained at Site P2 are shown next to core log (also see Fig. 12;**
698 **Table 1). The hanging wall anticline of the Bardibas thrust is observed at depth, with**
699 **a small syncline between the south-dipping forelimb of the main anticline and a**
700 **north-dipping limb of smaller tip-line fold of a southern splay, creating a local**
701 **lacustrine depocenter.**

702

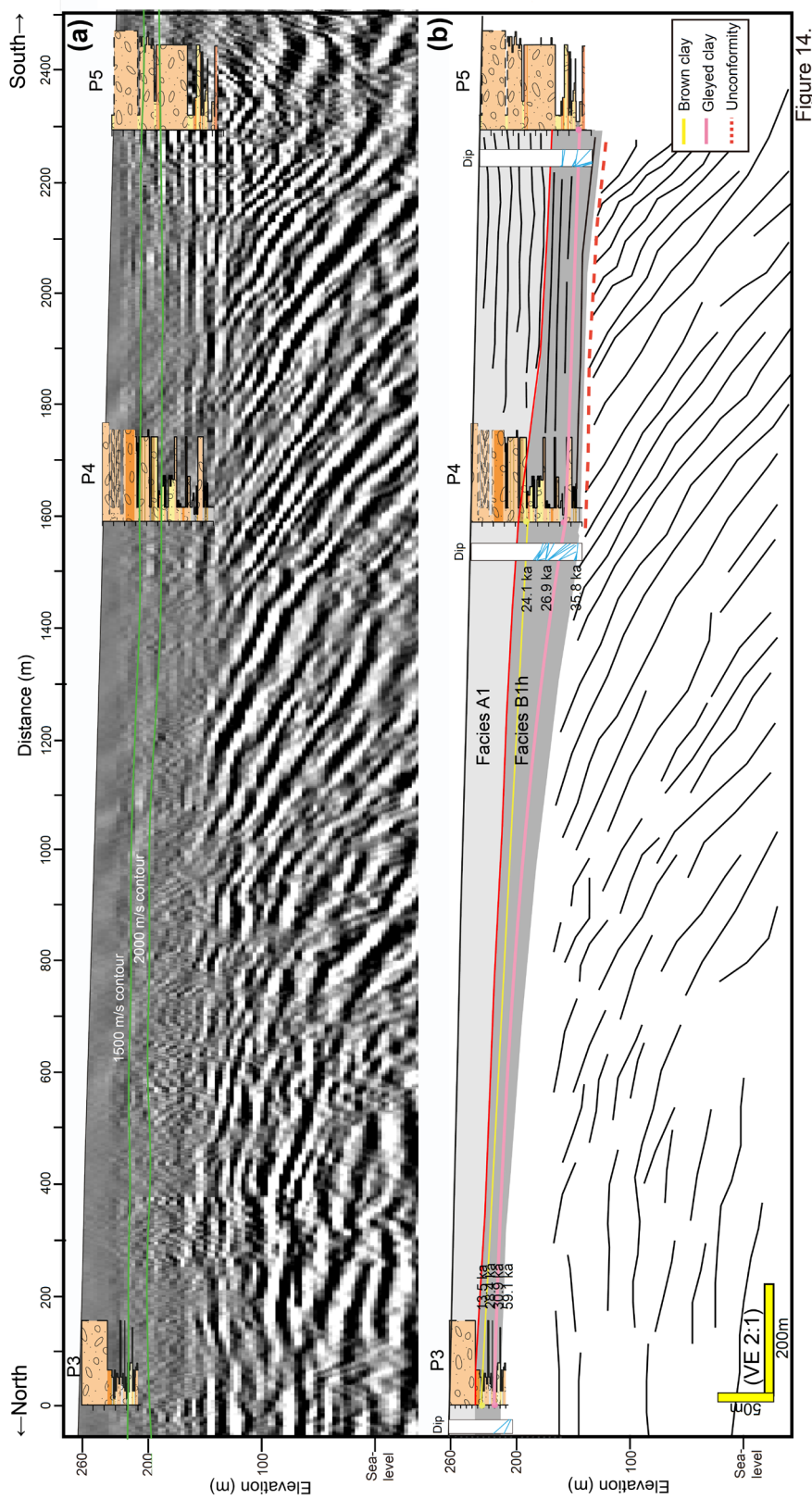
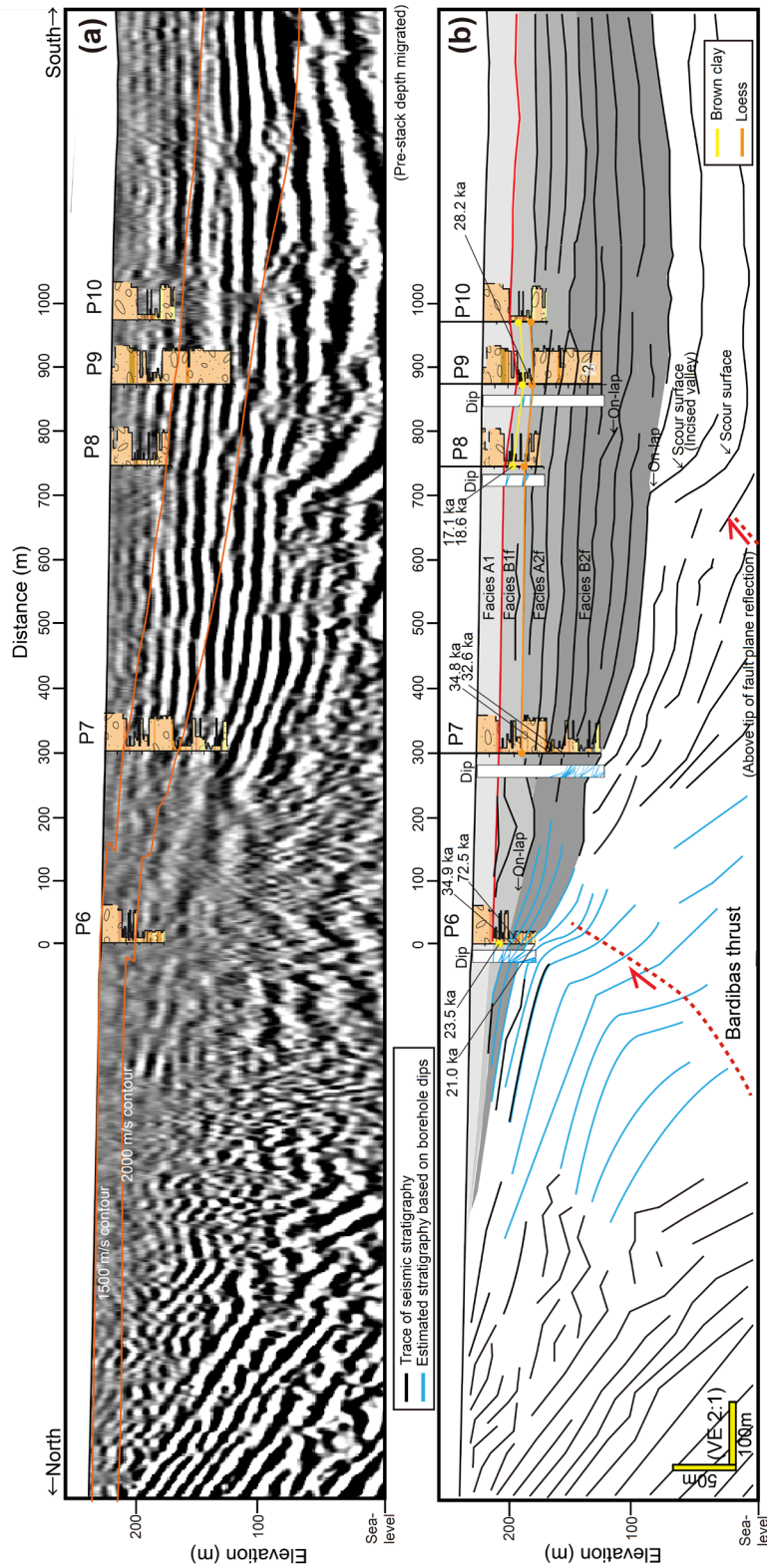


Figure 14.

703

704 **Figure 14. Bhabsi river cross-section. (a) Graphic sedimentary core logs of Sites P3–**

705 **P5 placed on seismic reflection profile of Almeida et al. (2018). The hanging wall**
706 **anticline of the Bardibas thrust is observed at depth (tilted strata). Vertical**
707 **exaggeration=2:1. (b) Interpretation of (a) with colored Facies A1 (light gray) and**
708 **Facies B (dark gray). Red line marks the base of Facies A1 at 27–68 mbs. The**
709 **seismically imaged angular unconformity (marked by red dashed line) between the**
710 **tilted sediments and relatively younger sediments (colored in gray). Measured dip**
711 **angles from the cores are shown in blue bars, vertically exaggerated (2:1). Marker**
712 **beds of brown clay (yellow dots and lines) and gleyed clay (pink dots and lines) are**
713 **traced and their ages are shown next to graphic logs (also see Fig. 12; Tables 1, 2).**
714

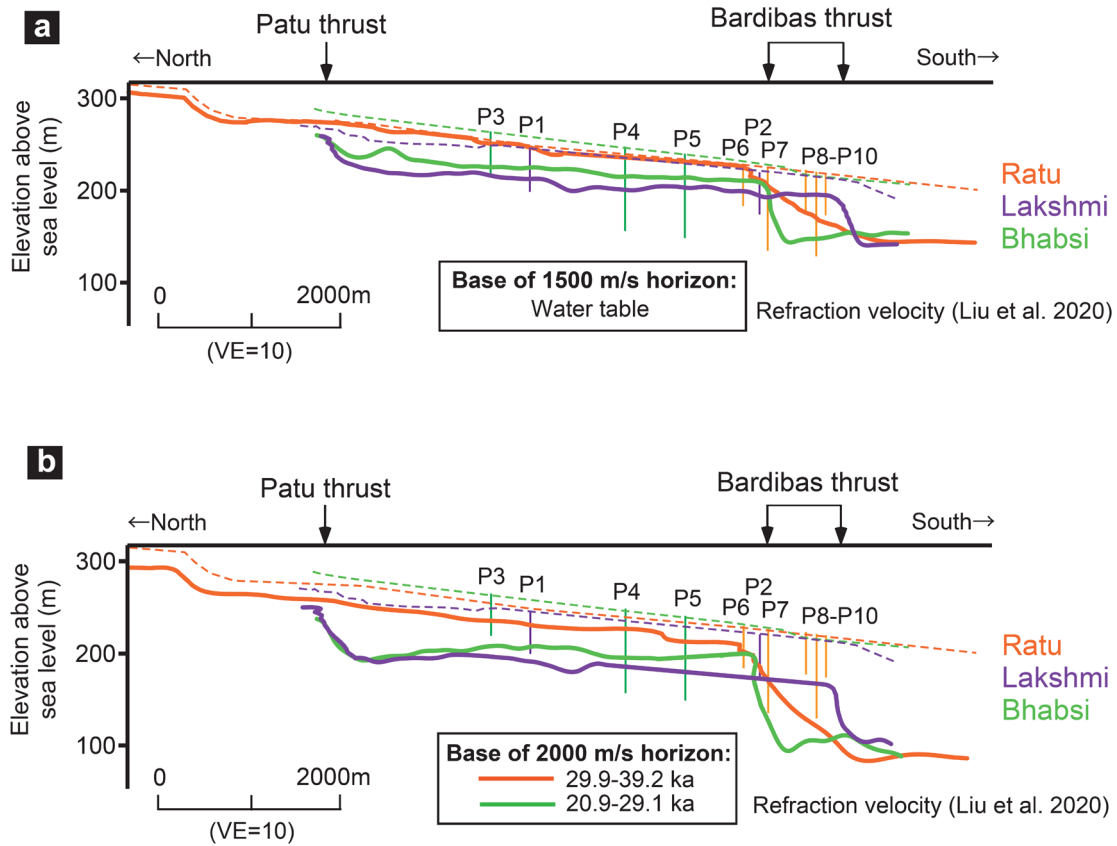


715

716 **Figure 15. Ratu river cross-section. (a) Graphic sedimentary core logs of Sites P6–**

717 **P10 placed on seismic reflection profile of Almeida et al. (2018). Northward increase**

718 **in dip in deeper sediments represents the effect of fault-propagation folding near the**
719 **tip of the Bardibas thrust. Growth strata are observed in the footwall (south side).**
720 **Vertical exaggeration=2:1. Near the base of the fold axis beneath Sites P6 and P7,**
721 **seismic section shows poor imaging. (b) Interpretation of (a) with colored Facies A**
722 **and B. Red line marks the base of top gravels (Facies A1) at ~15–28 mbs. Measured**
723 **dip angles from the cores are shown in blue bars, vertically exaggerated (2:1).**
724 **Marker beds of brown clay (yellow dots and lines) and loess (orange dots) are traced**
725 **and their ages are shown next to graphic log (also see Table 1). Fluvial on-lap of**
726 **sediments onto tilted strata is inferred. Red dashed lines represent the two fault**
727 **splays of the Bardibas thrust from Almeida et al. (2018). The tip of the southern**
728 **splay is inferred based on fault plane reflections beneath the growth strata, and the**
729 **position of the northern splay is inferred based on fault-propagation folding.**
730



731

732 **Figure 16. Boreholes placed onto refraction velocity models and the estimation of**

733 **the timing of uplift. (a) Boreholes and sediment ages from this study placed on the**

734 **refraction velocity model by Liu et al. (2020). Vertical exaggeration=10:1. 1500 m/s**

735 **contour traced along the Ratu, Bhabsi and Ratu river profiles, interpreted to**

736 **represent the water table. (b) 2000 m/s contour, proposed by Liu et al. (2020) to**

737 **represent the top of the bedrock (Siwalik Group). In this study, the 2000 m/s horizon**

738 **is found to be consistently above this contact, suggesting that the Siwalik Group**

739 **strata have faster seismic velocities.**

740

741 **5.1.1. Temporary lacustrine depocenter formed due to uplift of the hanging wall**

742 **anticline**

743 Along the Lakshmi river, Site P1 is located near the crest of the hanging wall
744 anticline of the Bardibas thrust, above the gently north-dipping back-limb, whereas Site
745 P2 is located to the south, above a secondary tip-line anticline (Figs. 2c, 13). Since we do
746 not have sediment ages from Site P1, and the seismic reflection imaging does not exhibit
747 clear and continuous reflectors in this shallow section (Fig. 13a), we cannot define the
748 timing of the facies transitions at Site P1. Because of this, we cannot exclude the
749 possibility that Site P1 may have penetrated the bedrock Upper Siwalik Group (Fig. 13b).

750 At Site P2, beneath the recent ~10–20 m of coarse gravels (Facies A1), we
751 identified a >25-m-thick section of lacustrine facies sediments (Facies C), which was not
752 evident at Site P1 (Figs. 4, 13). We interpret that a depocenter formed between the broad
753 anticlinal uplift to the north and the narrower uplift zone related to the fault tip to the
754 south, that would have impounded the river, creating a small depocenter in the small
755 syncline between these two anticlines (Fig. 13b).

756 The rate of deposition of the lacustrine sediments (Facies C) may represent the
757 minimum rate of uplift of the secondary anticline in order to maintain a lacustrine
758 depositional environment (e.g., Collignon et al., 2016). Samples from this section (Site

759 P2, Facies C) date from around 24.5 ± 0.3 to 43.1 ± 3.2 ka; however, it is not possible to
760 confidently infer how long the depocenter was active due to the large scatter in the data
761 (Fig. 12a). In addition, there may be a non-depositional time gap between the top of Facies
762 C and the base of Facies A1. We therefore are unable to use this section to infer tectonic
763 deformation rates.

764 Analogous modern depocenters have been identified elsewhere in the vicinity of
765 the MFT, produced by local tectonic uplift. Dasgupta et al. (2013) reported the
766 distribution of elongated lakes and marshes (long axis: ~ 0.5 – 1 km) with clay deposits
767 (~ 1 – 2 m thick) at the base of north-facing scarps in the Bhutan Himalaya. These lakes are
768 inferred to have resulted from damming of south-flowing rivers during uplift of the
769 hanging wall of the local strands of the MFT there (Dasgupta et al., 2013). Larger paleo-
770 lakes (~ 5 km in diameter) are also documented in the Lesser Himalaya in Kumaun near
771 thrust faults, with sediments composed largely of carbonaceous mud (> 5 – 10 m thick)
772 deposited around 21–36 ka (Kotlia et al., 2000, 2008, 2010). These paleo-lakes are
773 inferred to have formed behind thrust faults (Kotlia et al., 2000, 2008, 2010). Our study
774 is the first documentation of such a paleo-lake formed by the MFT in the frontal piedmont
775 in Nepal.

776 The paleo-lake sediments documented in this study were later capped by coarser

777 fluvial inputs/gravels (Facies A1) during the late Pleistocene to Holocene (Site P2, Figs.
778 4, 13). This change may have resulted from a reduction in the rate of tectonic uplift, the
779 breaching of the anticline by the Lakshmi river, or from a climate event that modified the
780 fluvial sediment supply and/or discharge. Similarly, a number of paleo-lakes in the
781 Kumaun Himalaya are also documented to have been filled with coarse fluvial deposits
782 at around the same time (Kotlia et al., 2000, 2010), suggesting that this lake filling may
783 have been the result of a regional climatic shift. The transition to coarse fluvial deposition
784 across the late Pleistocene–Holocene is discussed in more detail in Section 5.2.

785

786 **5.1.2. Tilted stratigraphy and uplift inferred from marker beds and ages above the** 787 **hanging wall anticline**

788 Along the Bhabsi river, Site P3 is located near the crest of the hanging wall
789 anticline of the Bardibas thrust, whereas Sites P4 and P5 are located on the forelimb, more
790 than 1 km south of the crest (Fig. 14). The coarse gravels of Facies A1 that compose the
791 top unit in these cores thicken downstream, from 27 to 42 m and then 68 m. Based on the
792 distance between the sites, and the changes in sediment thickness and channel slope, the
793 base of Facies A1 dips $\sim 1.2^\circ$ between Sites P3 and P4, and $\sim 2.8^\circ$ between Sites P4 and
794 P5, steeper than the current channel slope of $\sim 0.7^\circ$ (Fig. 14b). Below this unit (Facies

795 B1h), brown clay (at 28 mbs at Site P3 and 50 mbs at Site P4) and gleyed clay (at 39–40
796 mbs at Site P3, 80–85 mbs at Site P4, and 86–90 mbs at Site P5) can be traced as marker
797 beds (Section 4.2; Fig. 14b). Between Sites P3 and P4 the apparent dip of the brown clay
798 bed between boreholes is $\sim 1.5^\circ$, and the dip of the gleyed clay bed ranges $2.1\text{--}2.3^\circ$.
799 Between Sites P4 and P5, the gleyed clay bed dip ranges from 0.8° to 1.5° (Fig. 14b).
800 Compared to the stratigraphic dip constrained by the marker beds, the orientations of
801 laminae and silt beds measured directly from recovered cores ($2\text{--}65^\circ$) show some much
802 steeper values, which we attribute to local depositional and/or post-depositional processes
803 such as cross-bedding and soft sediment deformation, or deviation of the well bore from
804 vertical (Fig. 14b).

805 The tilting of the strata inferred from the boreholes along the Bhabsi river is likely
806 caused by a combination of changes in river slope through time due to changes in
807 sediment supply and/or river discharge (e.g., Finnegan et al., 2007), and folding of the
808 hanging wall anticline of the Bardibas thrust, with associated southward tilt of the
809 forelimb, similar to the shape of the underlying fold. In the current study, we cannot
810 quantify the effect of varying sediment supply or river discharge on channel slope,
811 however the difference in dip between the mapped dip of the marker beds and the current
812 river slope may be a maximum estimate for tectonic tilting. We note that between Sites

813 P4 and P5, the dip of the gleyed clay beds in Facies B1h (0.8–1.5°) is less than that at the
814 base of Facies A1 (~2.8°) above, although the clay beds of Facies B1h are older and
815 should have incurred more tectonic deformation. This suggests that sediment supply and
816 river discharge have a strong influence on the sediment thickness of Facies A1, obscuring
817 the effect of tectonic deformation (folding) by the thrust. This also suggests that the base
818 of Facies A1 may be erosive, and could have removed the underlying sediments (such as
819 the brown clay downstream of Site P4).

820 Here, we use the age and tilting of the base of the brown clay (24.1±3.2 ka) and
821 gleyed clay (30.9±2.3 ka) (Section 4.2) marker beds to estimate the shortening rate using
822 an area-of-uplift calculation (e.g. Lavé & Avouac, 2000; Almeida et al., 2018; Fig. 17).
823 We first estimate the area of uplift for each of the two marker beds, by tracing the tilted
824 stratigraphy of the base of the brown clay and the gleyed clay in the seismic section, and
825 inferring their original (undeformed) tilt of the sediments based on the modern channel
826 slope (Fig. 17b).

827 Since we did not observe brown clay at Site P5, we interpret that this marker bed
828 terminates between Sites P4 and P5, and/or was eroded at the base of Facies A1 (Fig. 17b).
829 Here, we estimate the extension of the brown clay south of Site P4, by extending the
830 stratigraphy between Sites P3 and P4 on a straight line (Fig. 17a,b). The section south of

831 Site P5 and north of Site P3 are also poorly imaged by the seismic data, and we cannot
832 directly observe the area of uplift between Site P5 and the fault tip, and the area of uplift
833 at the backlimb north of Site P3 (Fig. 17a,b). Here, we assume that the fold is symmetric,
834 and estimate the uplift at these locations by extending the stratigraphy of the marker beds
835 south of Site P5 to the fault tip and north of Site P3, and inferring the intersection with
836 the original (undeformed) tilt of the sediments based on the modern channel slope (Fig.
837 17a,b). Our ranges of shortening allow for qualitative uncertainties in the location of the
838 axial surface defining the northern edge of the backlimb, which is poorly imaged by the
839 seismic data and not penetrated by boreholes (Fig. 17ab).

840 We use a depth to detachment from the undeformed horizon of $\sim 1.9\text{--}2.1$ km,
841 defined by Almeida et al. (2018) from the Ratu profile, considering possible errors
842 associated with the location of the axial surface (horizontal shift by ± 100 m) and fault dip
843 shifts by $\pm 5^\circ$ (Almeida et al., 2018; Fig. 3a). Since the hanging wall is buried by thicker
844 sediments beneath the Bhabsi river than at Ratu river (Figs. 14, 15), it is possible that the
845 axial surface beneath Bhabsi is located further away from the fault tip than at Ratu,
846 making the detachment deeper than ~ 2 km. However, since we cannot clearly constrain
847 the axial surface from the Bhabsi profile due to the scatter in seismic signals (Fig. 17),
848 we prefer to use the depth to detachment (1.9–2.1 km) that is better constrained in the

849 Ratu section (Fig. 3a). We then assume conservation of mass; i.e., that the area displaced
850 along the detachment equals the area of uplift (Fig. 17c). By dividing the area of uplift by
851 the depth to detachment, we obtain shortening of 275 ± 14 and 313 ± 16 m in 24.1 ± 3.2
852 (brown clay) and 30.9 ± 2.3 ka (gleyed clay), respectively.

853 We plot the shortening vs. time to calculate an average shortening rate, assuming
854 that the rate was constant over time (Fig. 18a). From this analysis, the shortening rate of
855 the Bardibas thrust ranges from 11.4 ± 2.4 m/ka (mm/a), inclusive of the full error ranges.
856 The linear regression taking into account uncertainties of both ages and shortening (York
857 et al., 2004) yields a shortening rate of 10.5 ± 1.8 m/ka (mm/a) (Figure 18a; best-fit line).
858 The shortening rate may have changed over time, but we do not have sufficient date points
859 to address this. We also note that a deeper detachment depth will produce smaller
860 shortening rates; e.g. if we use 3 km as detachment depth, we estimate a shortening rate
861 of 7.5 ± 1.3 m/ka.

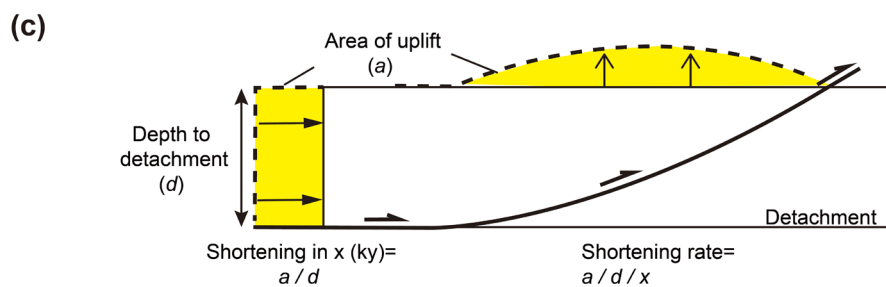
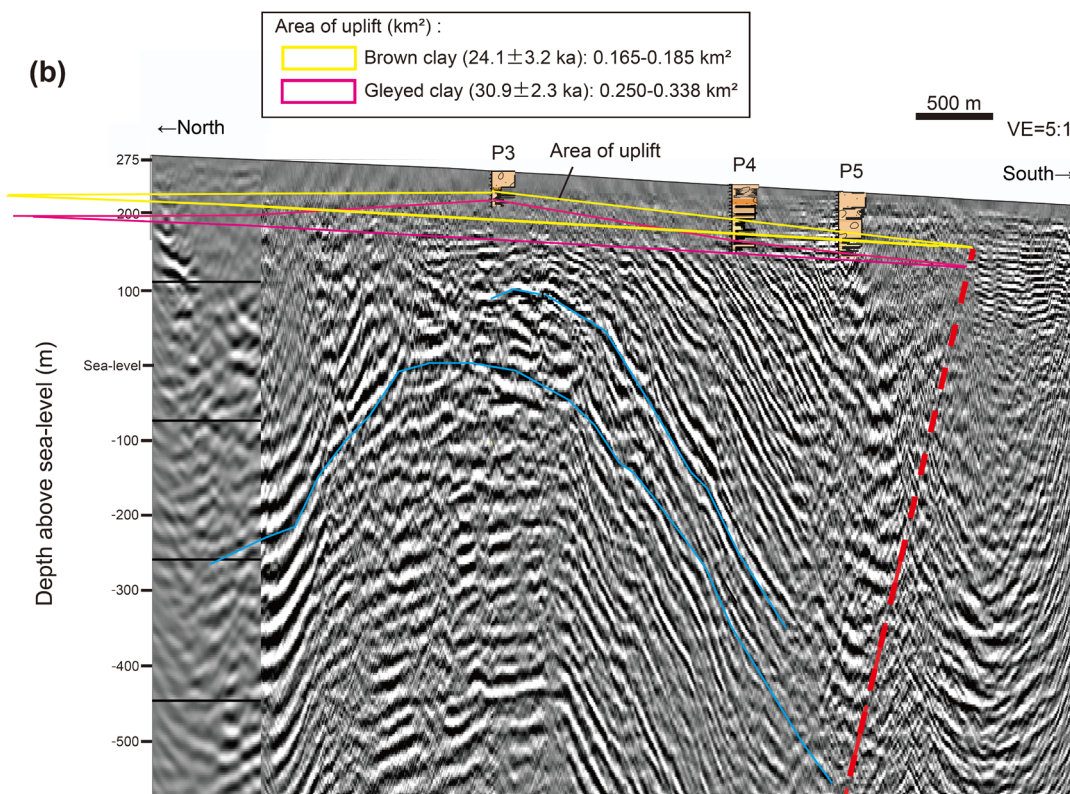
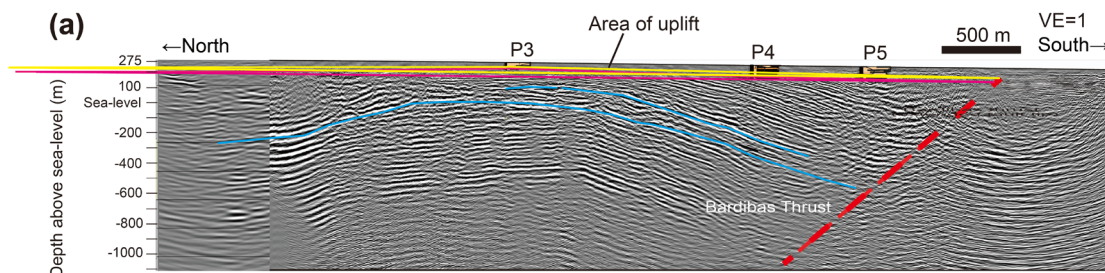
862 Near or below the base of Sites P4 and P5 (deeper than ~ 100 mbs), seismic
863 imaging reveals that the Siwalik bedrock dips $\sim 14^\circ$, significantly steeper than the
864 overlying sediments, below an angular unconformity (Almeida et al., 2018; Fig. 14).
865 Creating this angular unconformity requires at least two phases: first, uplift and erosion
866 (here, associated with tectonic folding), followed by a period during which the deposition

867 rate exceeded the uplift rate. The sediments at 49 mbs at Site P3 are dated to 59.1 ± 4.6 ka,
868 which is the oldest obtained age in the drilled sections of the hanging wall. The overall
869 thickness of the stratigraphy at Site P3 is thinner compared to Sites P4 and P5, likely due
870 to the faster uplift near the crest of the anticline (Fig. 14, Table 2). Given that the
871 underlying Siwalik Group sediments are much older (Miocene–Pliocene), we infer that
872 the P3 borehole did not penetrate the Siwalik Group bedrock (Figs. 6, 14; Table 2).

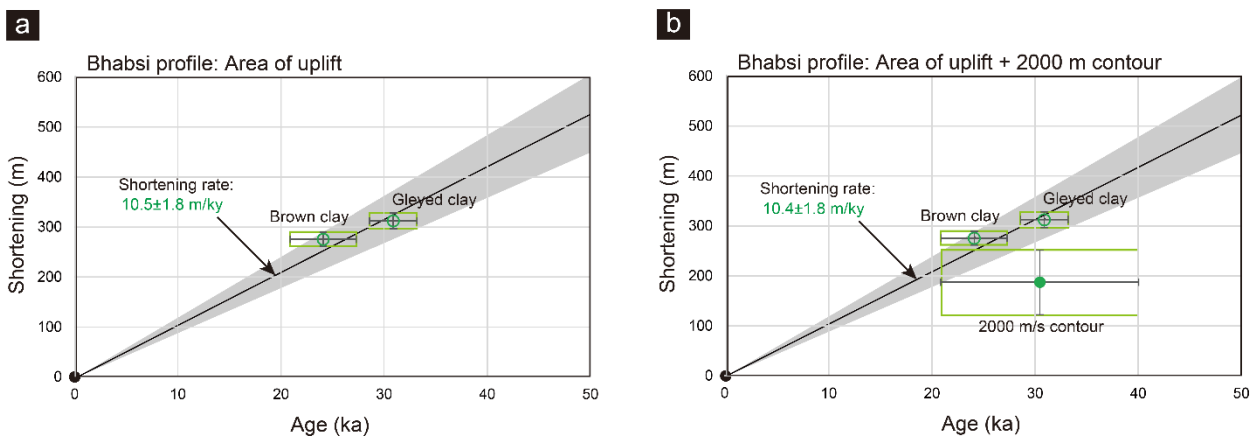
873 The geometry of the upper 100 m of strata is not well-imaged in the seismic
874 section (Fig. 14). The refraction velocity model by Liu et al. (2020) provides some
875 additional detail in this shallow section (Figs. 3b, 16). Liu et al. (2020) highlight a
876 transition at 1500 m/s, which they associate with the water table; this horizon lies
877 somewhere in Facies B1h in the hanging wall units but does not show the southward
878 deepening that we observe at Sites P3–P5, suggesting it may indeed reflect water rather
879 than stratigraphy (Figs. 3b, 16). Liu et al. (2020) interpret the boundary between Siwalik
880 Group and young sediments to be at 2000 m/s; with this interpretation, our boreholes P4
881 and P5 would penetrate the Siwalik Group (Figs. 3b, 16), which is inconsistent with the
882 deepest dates from P4 (Fig. 6). The fine-grained Facies B1h sediments may have lower
883 porosities and higher seismic velocities than the typical coarser young sediments (Facies
884 A1), resulting in the miss-association of these sediments with the lithified, higher velocity

885 Siwalik Group sediments.

886



888 **Figure 17. Shortening rate estimated from area-of-uplift calculation at the Bhabsi**
 889 **river. (a) Sites P3–P5 placed on seismic reflection profile of Almeida et al. (2018). No**
 890 **vertical exaggeration. Red dashed line represents the Bardibas thrust. Blue lines are**
 891 **representative trace of folded reflections at greater depth for reference. (b) Close-up**
 892 **of the entire lateral length of (a). Vertical exaggeration=5:1. Areas of uplift are**
 893 **obtained by tracing the base of the brown clay key marker bed (yellow) and the**
 894 **gleyed clay key marker bed (pink), assuming that the fold is symmetric, and by**
 895 **inferring that their depositional dip was equal to the modern channel slope. (c)**
 896 **Schematic cartoon showing the approach used to obtain shortening in this study,**
 897 **assuming that the area displaced along the detachment equals the area of uplift**
 898 **(colored yellow).**
 899



900 **Figure 18. Shortening rate estimation for the Bhabsi river section. Black dot shows**

901 **0 ka (zero shortening). Box shows error range. The slope of the best-fit linear**
902 **regression line indicates the shortening rate incorporating both uncertainties of**
903 **shortening and age (York et al., 2004). Error is 2σ . Gray shaded areas are 95%**
904 **confidence intervals. (a) Shortening estimated from area-of-uplift calculation based**
905 **on stratigraphy of key bed markers (base of brown clay and gleyed clay) along the**
906 **Bhabsi river profile (Fig. 17), plotted with sediment age. (b) Shortening combining**
907 **data from uplift of marker beds and 2000 m/s contours (Fig. 19).**

908

909 **5.1.3. High-angle beds and deformation bands related to shallow deformation at** 910 **the fault tip**

911 Sites P6–P10 are located near the fault tip of the Bardibas thrust, south of the
912 forelimb of the hanging wall anticline (Figs. 3c, 15). Here, there are two splays of the
913 Bardibas thrust. The tip of the southern splay is inferred to be at ~300 mbs based on fault
914 plane reflections beneath the growth strata, and the position of the northern splay is
915 inferred based on fault-propagation folding (Almeida et al., 2018; Fig. 15). The high-
916 angle beds observed in the cores at Sites P6 (~30–85° below 30 mbs) and P7 (~15°–45°
917 below 55 mbs) are likely the result of fault-propagation folding up dip of the northern
918 splay (Fig. 15). The seismic imaging cannot recover these high dips due to scattering of

919 the signal; Site P6 therefore lies in a zone of no imaging that continues ~300 m to the
920 south (Fig. 15). Based on the observations of bed dip from P6, we suggest that the abrupt
921 transition from imaging to noise reflects a fold axis.

922 Packages of sediments defined as Facies A1, B1f, A2f, and B2f can be traced across
923 Sites P6–P10 (Fig. 8); these sediments form the growth strata identified in seismic
924 reflection profiles (Almeida et al., 2018) and illustrate the gradual southward decrease in
925 stratigraphic dip (Fig. 15b). Traceable marker beds include the brown clay/silt and the
926 loess, as described in Section 4.2 (Figs. 8, 15b). Measured dips from the cores are
927 generally consistent with the dips of the seismic stratigraphy (Fig. 15b). The slight tilting
928 of beds (by $\sim 4^\circ$), which we observe around Sites P8 and P9 at ~ 15 – 40 mbs in both the
929 cores and seismic stratigraphy, likely reflects kink band deformation above the fault tip
930 documented by Almeida et al. (2018).

931 The tilted strata of Facies B2f observed at Sites P6 (> 31 mbs, Fig. 8a) and P7 ($>$
932 55 mbs, Fig. 8b) thicken downstream, from ~ 30 m thick below Site P6 to ~ 100 m thick
933 below Site P10, as inferred from seismic data (Fig. 15b). This observation is consistent
934 with uplift above the fault tip reducing the accommodation space. To the south, below
935 Site P8, a scour surface is present at ~ 130 mbs, interpreted as an incised valley associated
936 with episodes of incision and deposition (Almeida et al., 2018; Fig. 15b).

937 The near-vertical dip observed at Site P6 is consistent with surface outcrop
938 measurements of bedding dips below river terraces that are vertical and even locally
939 overturned in the southernmost part of the anticline forelimb (Almeida et al., 2018; Fig.
940 3a). These terraces are distributed above the current footwall growth strata, and the
941 exposed tilted beds are documented as Siwalik bedrock (Fig. 3a). Beneath the current
942 river, the bedrock is covered by growth strata. These growth strata exhibit sub-horizontal
943 dips at shallow depths, and become steep below ~30–55 mbs at Sites P6 and P7 (Fig. 11).
944 The near-vertical beds below ~30 mbs at Site P6 are dated to 21.0–72.5 ka (Fig. 8),
945 indicating that they are not bedrock Upper Siwalik Group, despite their intense
946 deformation. The significant amount of deformation of these young sediments and the
947 terraces at the surface is likely due to localized deformation at the fault tip (Fig. 15).

948 Shallow deformation is also evident in the form of deformation bands, found in
949 medium-coarse sand at Site P7 at 66 mbs (Section 4.1.3.2) (Figs. 10h–m). Here, we note
950 deformation bands ~230 m above the fault tip of the Bardibas thrust; these are likely
951 associated with related folding and strain. Deformation bands are a suite of narrow
952 (generally mm- to cm-thick), low-displacement, tabular deformational features found
953 both in poorly lithified porous sediments (Cashman et al., 2007), and lithified sediments
954 with porosity >15%, such as sandstones, carbonates, tuffs, and chalks (Aydin, 1978;

955 Wilson et al., 2003; Fossen et al., 2007; Cilona et al., 2012; Wennberg et al., 2013; Pizzati
956 et al., 2020). The deformation bands observed in this study indicate significant grain size
957 reduction and porosity loss by cataclasis (Fig. 10h–m), and are classified as ‘shear bands’
958 or ‘cataclastic shear bands’ on the basis of their morphology (Fossen et al., 2007).

959 Cataclastic shear bands are generally known to form where higher confining and
960 shear stresses in an initially high-porosity material are sufficient for grain breakage to
961 occur (Fossen et al., 2007). In porous lithified rock, shear band formation is thought to
962 occur at 1.5–3.0 km depth and effective stresses of 20–40 MPa, based on numerous field
963 studies in predominantly quartz-rich aeolian sandstones (Fossen et al., 2007 and
964 references therein), with the onset of cataclasis at burial depths of 0.9–1.2 km in quartz-
965 rich sands, while in more arkosic sands, the onset of cataclasis in shear bands can occur
966 at burial depths of 0.4–0.5 km (Beke et al., 2019; Pizzati et al., 2020). In contrast, the
967 position of Site P7 in the hanging wall block of the active Bardibas thrust precludes
968 significant burial beyond present-day depth, and the maximum overburden stress at ~66
969 m depth is ~1.3 MPa, assuming an average 15% overburden porosity. The confining
970 stresses are thus too low to explain the significant cataclasis that is observed in the core
971 (Figure 10h–m). The formation of deformation bands and observed cataclasis may thus
972 likely instead records slip at seismic velocities reaching the surface in the process zone at

973 the tip of the Bardibas thrust at some point post-deposition.

974 Cataclastic shear bands, with both porosity loss and visible cataclasis are also
975 documented from unlithified sands in the immediate vicinity of active faults such as the
976 San Andreas and McKinnleyville faults in California, USA (Cashman & Cashman, 2000;
977 Cashman et al. 2007, Kaproth et al., 2010). These cataclastic bands in sands with
978 maximum burial <200 m have been posited to be indications of slip at seismic velocities
979 owing to the very low (<4.5 MPa) possible maximum overburden stresses at such depths
980 being insufficient on their own to induce the observed cataclasis (Cashman et al., 2007).
981 We suggest that the deformation band at Site P7 at ~66 m burial depth may similarly
982 record brittle localized slip suggestive of rapid failure.

983

984 **5.1.4. Slip rate estimation based on age and vertical uplift inferred from seismic**
985 **refraction velocities**

986 Figure 16 shows the depths of interpreted horizons based on seismic refraction
987 velocities along the Lakshmi, Bhabsi, and Ratu river profiles (Liu et al., 2020). By placing
988 our boreholes on the refraction velocity models and integrating our new dates with
989 previously inferred fault throw, we can infer the rate of uplift on the Bardibas thrust (Figs.
990 3b, 16). Here, we evaluate the 1500 and 2000 m/s contours identified by Liu et al. (2020)

991 and establish the age of sediments for these horizons.

992 We first evaluate the 1500 m/s contour, interpreted by Liu et al. (2020) to represent
993 the water table. Along the Lakshmi, Bhabsi, and Ratu rivers, this contour exhibits a
994 vertical offset of ~17–32, ~12–51, ~57–66 m between the hanging wall and footwall of
995 the Bardibas thrust, respectively (Liu et al., 2020) (Figs. 3b, 16a). In our boreholes, this
996 1500 m/s contour exists at ~40 mbs (Facies B) at Site P1 and ~27 mbs (Facies C) at Site
997 P2 along the Lakshmi river (Figs. 3b, 16a). At the Bhabsi river, the 1500 m/s horizon
998 exists at ~40 mbs (Facies B1h), ~35 mbs (Facies A1), and ~30 mbs (Facies A1) at Sites
999 P3, P4, and P5, respectively (Figs. 3b, 16a). At the Ratu river, the 1500 m/s horizon is
1000 inferred at the subsurface at Site P6, ~15 mbs (Facies B1f) at Site P7, and at ~50 mbs
1001 (Facies A2f) at Site P9 (Figs. 15, 16ab). Given that we observe different lithologies at
1002 these depths, we agree that the 1500 m/s contour likely represents a non-stratigraphic
1003 feature like the water table, and therefore we are unable to assign an age for this horizon.

1004 The 2000 m/s contour is inferred to represent a regional lithological boundary,
1005 common in all the three rivers, likely at the base of or within relatively young sediments
1006 (Liu et al., 2020) (Fig. 3b). At the Lakshmi river, this contour lies approximately at the
1007 base of our borehole at Site P2, and therefore the dates from the borehole would
1008 correspond to the sediments overlying it (Figs 3b, 16b). The dates in Facies C are mixed,

1009 ranging from 24.5 ± 0.3 ka at 30.2 mbs to 43.1 ± 3.2 ka at 26.8 mbs (Fig. 12a). Three
1010 well-constrained dates at 37.4–40.4 mbs near the base of the borehole all date between
1011 35.2–40 ka (Fig. 12a), so we here use 40 ka to represent the youngest possible age of the
1012 contact at the Lakshmi river.

1013 At the Bhabsi river, the 2000 m/s contour is at ~55 mbs (Facies B1h) at Site P4 and
1014 ~40–45 mbs (Facies A1/Facies B1h) at Site P5 (Fig. 3b, 16b); we estimate the timing of
1015 this horizon to be ~20.9–29.1 ka, based on the sediment age from Site P4 (24.1 ± 3.2 ka
1016 at 50.8 mbs and 26.9 ± 2.2 ka at 69.8 mbs) (Fig. 6). At the Ratu river, the 2000 m/s horizon
1017 is inferred at ~30 mbs (Facies B1f) at Site P6 and ~60 mbs (Facies B2f) at Site P7 (Figs.
1018 3b, 16b); we infer the timing of this horizon to range ~29.9–39.2 ka, based on sediment
1019 age of 34.8 ± 3.1 and 32.6 ± 2.7 ka at 56.8 mbs and 70.8 mbs at Site P7, respectively, and
1020 34.9 ± 4.3 ka at 33.8 mbs at Site P6 (Fig. 8).

1021 Here, we treat the sediment age of the 2000 m/s contour beneath the three rivers to
1022 be the same, and use the overall age range of ~20.9–40 ka to characterize this horizon for
1023 all the rivers, and fully incorporate the uncertainties of age. At the Lakshmi river, a
1024 vertical offset of ~37–42 m of the 2000 m/s contour is evident (Liu et al., 2020) (Fig. 16b).
1025 When using the sediment age of 20.9–40 ka, this yields a tectonic throw rate of 0.9–2.0
1026 m/ka (mm/a), corresponding to a shortening rate of 1.9–5.9 m/ka (mm/a) given a fault dip

1027 of 20°–30° (Fig. 19).

1028 At the Bhabsi river, a vertical offset of ~61–86 m is inferred at the 2000 m/s contour
1029 (Liu et al., 2020; Figs. 3b, 16b,c). From the estimated vertical offset and assigned age
1030 (20.9–40 ka), we calculate an uplift rate of 1.5–4.1 m/ka (mm/a), translated to a shortening
1031 rate of 3.1–12 m/ka (mm/a), using a fault dip of 20–30° (Fig. 19). The slip rate is
1032 comparable with the average shortening rate of 9.7–12.1 m/ka (mm/a) estimated by area
1033 of uplift calculation at the Bhabsi river in Section 5.1.2 (Figs. 17, 18), although it is also
1034 wide enough to be consistent with area of uplift estimates based on deeper detachment
1035 depths as well. When combining the results from the area of uplift and 2000 m/s contour,
1036 the linear regression taking into account uncertainties on all errors (York et al., 2004)
1037 yields a shortening rate of 10.4 ± 1.8 m/ka (mm/a) (Fig. 18b).

1038 At the Ratu river, a vertical fault offset of >~95–101 m is inferred at the 2000 m/s
1039 contour (Liu et al., 2020; Figs. 3b, 16). The offset is a minimum fault throw, as the hanging
1040 wall is not fully preserved due to substantial erosion along the Ratu section (Fig. 3b).
1041 From the estimated vertical displacement, assigned age (20.9–40 ka), and fault dip (20–
1042 30°), we calculate an uplift rate of >2.4–4.8 m/ka (mm/ya), corresponding to a shortening
1043 rate of >4.8–14.1 m/ka (mm/a; Fig.19).

1044 Uplift along the Ratu river has also been estimated from river terraces (Bollinger

1045 et al., 2014). Bollinger et al. (2014) describe at least four river terrace levels in the hanging
1046 wall of the Bardibas thrust, which have heights of ~ 1 – 2 , ~ 16 , ~ 40 – 45 , and ~ 70 m above
1047 the current riverbed. If we incorporate the height of the regionally highest river terrace
1048 level (~ 70 m) as the maximum additional uplift in our estimation of slip rate at the Ratu
1049 section, this yields a maximum uplift and shortening rate of ~ 8.2 m/ka (mm/a) and ~ 23.9
1050 m/ka (mm/a), respectively, using a fault dip of 20 – 30° (Fig. 19).

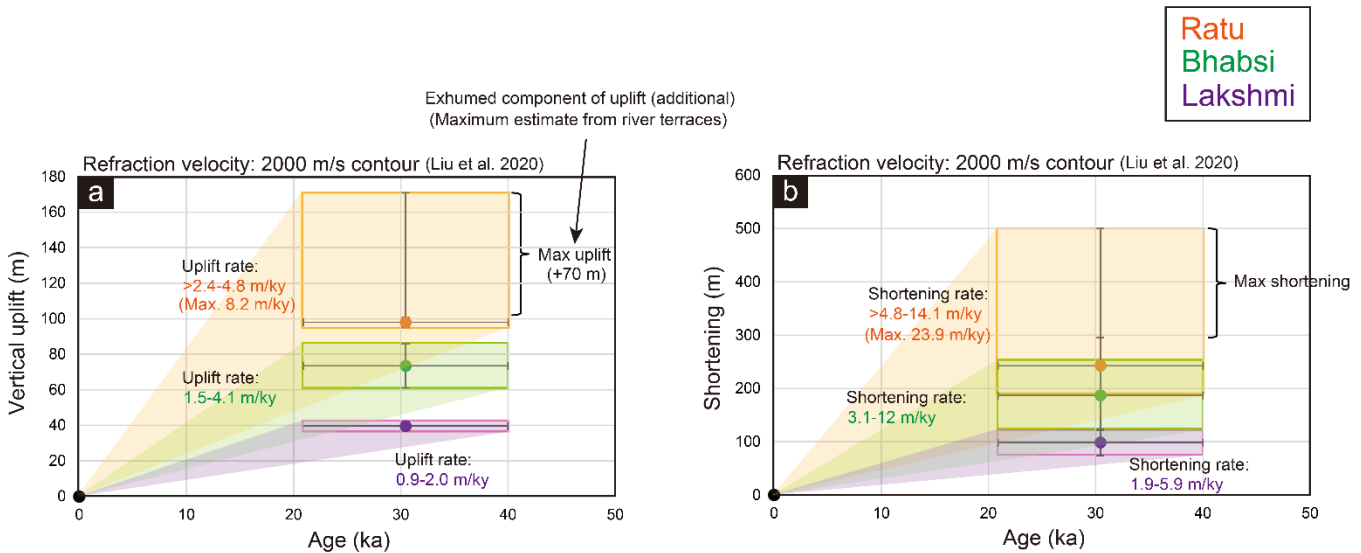
1051 Bollinger et al. (2014) estimate an uplift rate of ~ 10 mm/a by the Bardibas thrust
1052 on the basis of the 70 m high terrace, estimated to date to ~ 7 ka (Gaillard et al., 2011).
1053 Using a fault dip of 20 – 30° , this would reflect a slip rate of 20 – 29 m/ka, which exceeds
1054 the shortening rate across the Himalaya (e.g., Lindsey et al., 2018) and is therefore
1055 implausible. We note that the age of this terrace (~ 7 ka) is poorly constrained, which is
1056 derived from a single charcoal sample (Gaillard et al. 2011). Furthermore, fluctuations in
1057 past river base level could either add to or subtract from this value, and we are not able
1058 to constrain this as we do not have materials dated within the last 7 ka (Tables 1, 2). The
1059 height of river terrace levels may also be affected by incision caused by climate events;
1060 assumptions of steady-state (erosion balancing uplift) may not be appropriate as the
1061 regional climate events such as the Indian monsoonal variations are reported in millennial
1062 to centennial to decadal scales (e.g., Wang et al., 2001; Fleitmann et al., 2003; 2007), and

1063 are likely to have an impact on river base levels and sedimentary environment (e.g., Pratt
1064 et al., 2004; Sharma et al., 2004) (Section 5.2).

1065 Overall, our results indicate that the Bardibas thrust has slipped at an average rate
1066 of 1.9–5.9 m/ka (mm/a) (uplift rate: 0.9–2.0 m/ky) beneath the Lakshmi river, 3.1–12.1
1067 m/ka (mm/a) (uplift rate: 1.5–4.1 m/ka) beneath the Bhabsi river, and >4.8 m/ka
1068 (maximum 23.8 m/ka) (uplift rate: >2.4 m/ka; maximum uplift rate: 8.2 m/ka) beneath
1069 the Ratu river over the last ~50 ka (Figs. 18, 19). We calculate an increase in slip rate from
1070 west (Lakshmi) to east (Ratu), which is consistent with the fact that the overall slip on the
1071 Bardibas thrust decreases towards the west where the Bardibas thrust strand is dying out,
1072 and transferring slip onto the Patu fault strand to the north (Almeida et al., 2018; Liu et
1073 al., 2020) (Fig. 2c). Our results from the Bhabsi river are more accurate as they likely
1074 reflect the full tectonic offset (Figs. 18, 19). The eastward increase in fault slip is
1075 compatible with observed variations in sediment thickness among the three rivers; we
1076 measure thicker sediments in the hanging wall along the Bhabsi river than in the Ratu
1077 river. In addition, there are possible variations caused by local depositional conditions
1078 due to river size and/or proximity of the range front. For example, we measure a thicker
1079 section of Facies A1 (27–68 m thick) beneath the Bhabsi river in the hanging wall of the
1080 Bardibas thrust than beneath the Ratu river (15–28 m thick) in the footwall of the Bardibas

1081 thrust (Figs. 13–15), also indicated by the brown clay marker bed that underlies it (Section
 1082 4.2) (Figs. 14–15).

1083



1084 **Figure 19. Uplift and shortening rate estimations using the 2000 m/s contour by Liu**
 1085 **et al. (2020). Black dot shows 0 ka (zero shortening). Box shows error range. Colored**
 1086 **areas show the range of uplift/shortening rate incorporating all errors. (a) Vertical**
 1087 **offset at the base of 2000 m/s velocity contours along the Ratu, Bhabsi, and Lakshmi**
 1088 **river profiles, plotted with sediment age. We incorporate additional uplift (~70 m;**
 1089 **maximum value) above the riverbed from river terrace studies (Bollinger et al.,**
 1090 **2014). (b) Shortening estimated from vertical fault offset at the base of 2000 m/s**
 1091 **velocity contours (a), plotted with sediment age.**

1092

1093 The Patu strand remains active at the longitude of the Ratu river, so we interpret
1094 that the slip here is being partitioned between the Bardibas and Patu thrusts (Fig. 2c). At
1095 the Ratu river, Almeida et al. (2018) calculated a total shortening of 1.81 km associated
1096 with the Patu thrust, and 1.67 km associated with the Bardibas thrust along their seismic
1097 lines. If the shortening rate is distributed along the same lines in the inferred ratio
1098 (1.81:1.67), this would imply that the Patu thrust is shortening at a rate of $>5.2\text{--}15.3$ m/ka
1099 (mm/a), and together the faults would be taking up $>10\text{--}29.4$ m/ka (mm/a). This
1100 assumption may be reasonable given that each fault is the frontal thrust of the range within
1101 a short distance (Fig. 2c), but is not founded in observation, and the uncertainties above
1102 do not reflect either the possibility that the ratio of active shortening differs from the total
1103 shortening, or uncertainties in the total shortening.

1104 Bollinger et al. (2014) inferred that the river terrace abandonments in this region
1105 were locally consecutive to great earthquakes, and estimated the recurrence interval of
1106 past earthquakes and an average uplift rate of 8.5 ± 1.5 mm/a (along the Sir river) and 10--
1107 12 mm/a (along the Ratu river) on the Patu and Bardibas thrusts, respectively, based on
1108 the elevations and dating of river terraces. Overall, their estimation is much larger than
1109 the uplift rate inferred in this study. This may be due to the maximum estimate of uplift
1110 from river terraces, which may also be affected by incision caused by climate events

1111 (Section 5.2).

1112 The geodetically constrained shortening rate across this section of the Himalaya is
1113 15–16 m/ka (mm/a) (Lindsey et al., 2018); thus, the rate on this section of the Bardibas
1114 thrust inferred from this study from the Bhabsi river (3.1–12.1 m/ka; York regression:
1115 10.4 ± 1.8 m/ka) (Fig. 18) represents 19–81% (York regression: 54–81%) of the total
1116 shortening across the range. Lavé and Avouac (2000) interpreted that nearly all of the
1117 interseismic shortening eventually manifests as slip on the frontal thrust systems in the
1118 region around the Bakeya and Bagmati Rivers, 40–60 km west of our field area. This
1119 would be consistent with our results, but our large uncertainties mean that we cannot
1120 exclude the possibility of significant shortening being accommodated on other structures
1121 within the range.

1122

1123 **5.2. Implications for the depositional environment across monsoonal climate**

1124 **variations**

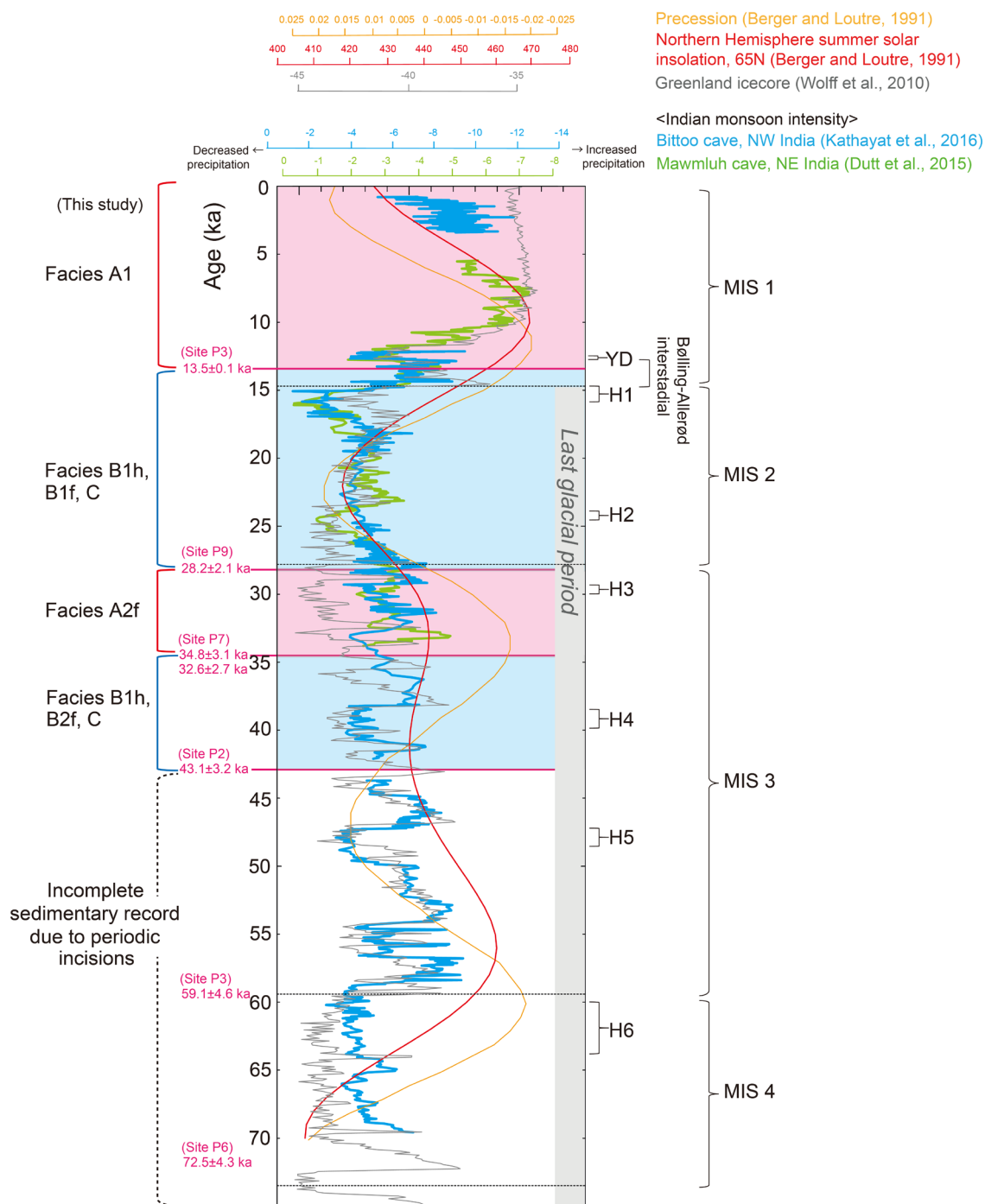
1125 **5.2.1 Facies transitions in this study compared with paleoclimate records**

1126 We identify three depositional facies in the sediment cores recovered from the
1127 three rivers: coarse-grained braided channel (Facies A), fine-grained braided channel

1128 (Facies B), and fluvio-lacustrine (Facies C); these are primarily marked by changes in p
1129 (grain diameter) size (Section 4.1; Figs. 4, 6, 8). The fact that we observe similar facies
1130 transitions in different rivers suggest that they represent a regional event. In general,
1131 changes in fluvial sediment grain size are thought to be associated with variations in river
1132 discharge, sediment supply, abrasion, and subsidence rate (e.g., Robinson & Slingerland,
1133 1998; Dingle et al., 2017). The timescale of the sediment deposition in this study is tens
1134 of ka, and therefore tectonic subsidence/uplift (>hundreds of ka) and/or earthquake-
1135 triggered landsliding (<few hundred years) (e.g., Bollinger et al., 2014; Rizza et al., 2019)
1136 cannot be the cause for the observed variations in grain size, except for Facies C, which
1137 we observe only at Site P2 and interpret as related to localized uplift to the south (see
1138 Section 5.1.1). We can also eliminate variations in abrasion, as the sediments are quartz-
1139 dominant and the length of the catchment is only a few km. We therefore suggest that
1140 changes in river discharge and sediment supply are likely to be the primary processes
1141 recorded in these sedimentary facies. Higher river discharge is capable of transporting
1142 more and coarser sediments, and hence, the grain size of deposited sediments is expected
1143 to be larger (e.g., Parker, 1978). Empirical and physical studies have shown that an
1144 increase in river discharge tends to increase both sediment grain size and channel width
1145 (e.g., Parker, 1978; Bray, 1982; Hey and Thorne, 1986).

1146 A major transition from fluvio-lacustrine facies (Facies B1h, B1f and C) to coarse
1147 braided channel facies (Facies A1) is observed at depths of ~15–68 mbs in all ten
1148 boreholes (Figs. 4, 6, 8). ¹⁴C and OSL dating from Site P3 suggest that this transition,
1149 from finer sediments to coarser, is younger than ~13.5±0.1 ka, around the Pleistocene-
1150 Holocene transition (Fig. 12b). The timing of this facies transition coincides with a
1151 transition in regional climate observed in a number of climate proxies. Specifically, the
1152 Indian monsoon was generally weak in the late Pleistocene, and became much stronger
1153 during the Holocene, as determined from speleothems from the Bittoo cave in northwest
1154 India (Kathayat et al., 2016), the Timta cave in north-central India (Sinha et al., 2005),
1155 and the Mawmluh cave in northeast India (Dutt et al., 2015) (Fig. 20). Previous studies
1156 have linked monsoonal variability with Earth's orbital parameters, such as precessional
1157 cycles and variations in the Northern Hemisphere summer solar insolation (NHSI),
1158 punctuated by millennial-scale oscillations such as the Younger Dryas and Heinrich
1159 events (e.g., Cai et al., 2015; Kathayat et al., 2016). The period of strengthened monsoon
1160 around the Pleistocene/Holocene transition correlates with the peak of the NHSI and
1161 precession that occurred following the Bølling-Allerød interstadial and the last glacial to
1162 interglacial boundary (Berger and Lutre, 1991; Wolff et al. 2010) (Fig. 20).

1163



1164

1165 **Figure 20. Comparison of our stratigraphic records to records related to the Indian**
 1166 **summer monsoon. Plotted records include: compiled $\delta^{18}O$ records of cave**
 1167 **speleothems (blue and green) tracking Indian summer monsoon intensity, Northern**

1168 **Hemisphere summer solar insolation (NHSI) (red), orbital precession cycle (orange),**
1169 **and Greenland ice core records (gray). Speleothem $\delta^{18}\text{O}$ data indicate Indian**
1170 **summer monsoon intensity, where larger absolute values indicate increased**
1171 **precipitation. YD: Younger Dryas. H1–H6: Heinrich events. Gray vertical bar**
1172 **marks the duration of the last glacial period. MIS 1–4: Marine isotope stages,**
1173 **separated by horizontal dotted lines (black). Red shading: Facies A in this study.**
1174 **Blue shading: Facies B and C in this study. Red horizontal line marks the age of each**
1175 **facies transition based on sediment age from Sites P2 (43.1 ± 3.2 ka), P3 (13.5 ± 0.1 ka),**
1176 **P6 (72.5 ± 4.3 ka), P7 (34.8 ± 3.1 ka, 32.6 ± 2.7 ka), and P9 (28.2 ± 2.1 ka) in this study.**
1177 **Facies B and C roughly correlates with the minima of the precession and NHSI,**
1178 **when the monsoon was weaker. In contrast, Facies A roughly coincides with the**
1179 **precession and NHSI maxima, when the monsoon was stronger. Prior to ~ 43 ka, we**
1180 **are unable to correlate facies with climate events due to missing ages likely**
1181 **associated with incision.**

1182

1183 Below this interval, the footwall strata exhibit packages of fine-grained Facies B1f
1184 dated to ~ 13.5 – 28.2 ka (Figs. 8, 15). These dates match to a period with low NHSI and
1185 low precession, when the monsoon was weak (Dutt et al., 2015; Kathayat et al., 2016)

1186 (Fig. 20). This period also corresponds to marine isotope stage (MIS) 2, during the last
1187 glacial.

1188 Below this section of Facies B1h and B1f, we have mixed records: at Sites P3 and
1189 P4 (hanging wall), we do not recognize another major facies transition, although ages in
1190 these cores reach as old as 59.1 ± 4.6 ka (Fig. 6). In contrast, in the footwall cores (P7–
1191 P10), we identify a second package of coarse-grained Facies A2f dating to ~ 28.2 – 34.8 ka
1192 (Figs. 8, 15). This difference may relate to lower stratigraphic preservation over the
1193 hanging wall due to uplift, or may have been eroded due to base level fluctuations. We
1194 therefore consider that the footwall record is likely to be more representative. Notably,
1195 the ages for this coarser section coincide with a period when the NHSI and precession
1196 were elevated, and the beginning of MIS 3 (globally warm period) (Fig. 20). Climate
1197 proxies also show that the monsoon was stronger during this period, although not as
1198 strong as during the Holocene (Dutt et al., 2015; Kathayat et al., 2016; Fig. 20).

1199 The borehole at Site P7 penetrates an additional section of fine-grained Facies B2f
1200 in its lowest section (Fig. 8). This period also correlates to the deposition of Facies C
1201 (lacustrine) sediments at Site P2 (Fig. 4). During or before this period, there was also
1202 events of incision, as inferred from fluvial onlap in seismic imaging (Fig. 15). Climate
1203 proxies from this time (prior to ~ 32.6 – 34.8 ka) show high-frequency variations without

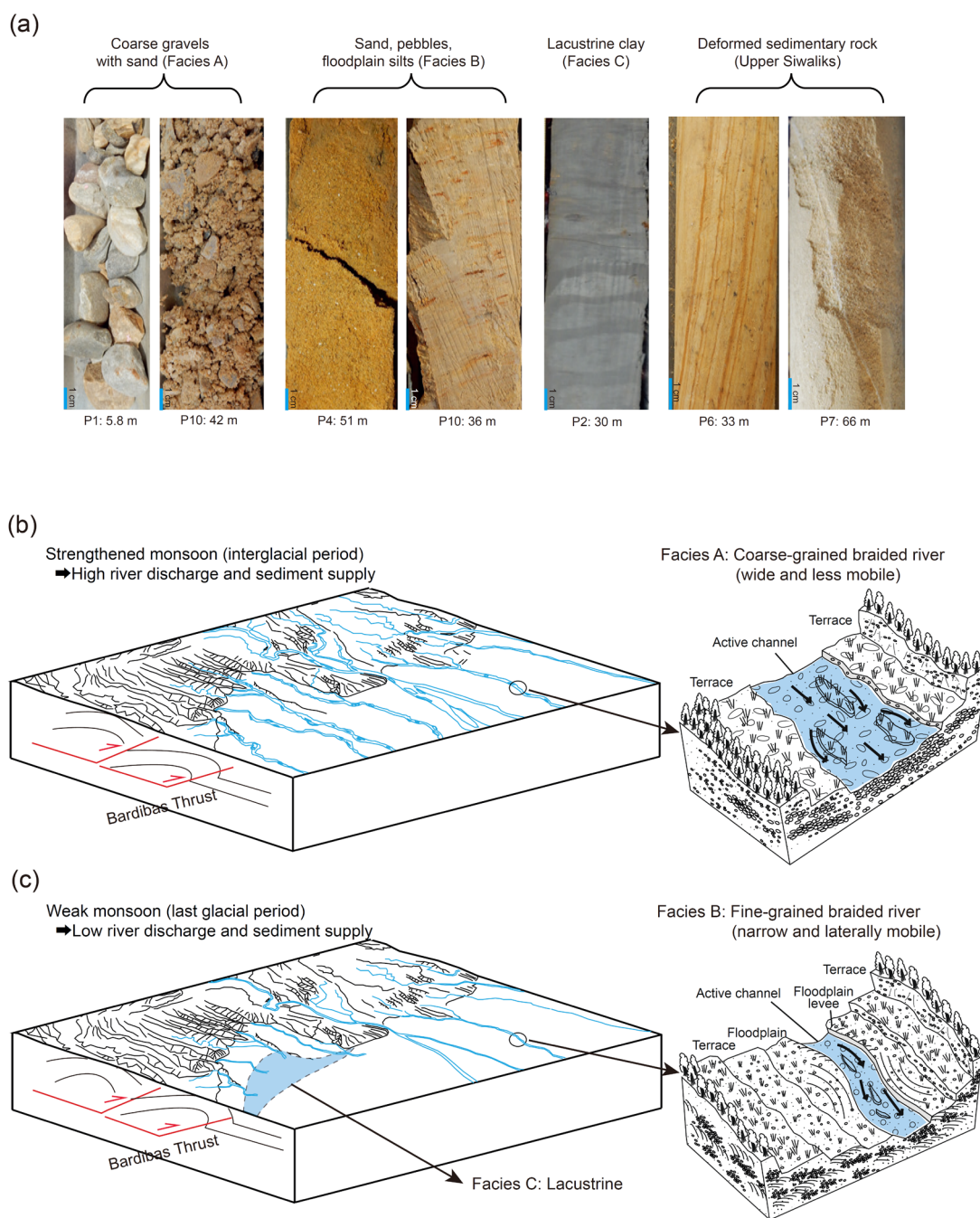
1204 large magnitude of changes; while during this time, the NHSI started low and increased
1205 over time (Fig. 20). Given our limited records (likely incomplete due to periodic incision),
1206 together with the variability in other climate proxies, it is not possible to link the facies
1207 in this section to specific climatic conditions. The oldest sediments that we recovered in
1208 this study date to 59.1 ± 4.6 ka at Site P3 in the hanging wall and 72.5 ± 4.3 ka at Site P6 in
1209 the footwall; however, we did not recover sediments between 43.1–59.1 ka and 59.1–72.5
1210 ka.

1211 We suggest that the primary sedimentary facies transitions observed in this study
1212 are likely associated with changes in the Indian monsoonal climate, which is linked to
1213 Earth's precession (~23-ka-cycle; Fig. 20). Indian monsoon intensity is a primary control
1214 on river discharge and sediment supply in this region. While the latest transition in
1215 sedimentary facies appears to correlate with the last glacial maximum, the catchments of
1216 the rivers we are studying were never glaciated (e.g. Owen et al., 2002, 2005, 2009;
1217 Tsukamoto et al., 2002; Asahi, 2010), and thus the glaciers did not directly affect river
1218 discharge and sediment output in this region.

1219 We interpret instead that the strengthened Indian monsoon through the late
1220 Pleistocene to the Holocene led to increased river discharge and the advance of coarse
1221 bedload-dominant braided channels in our study area (Figs. 21a, b). These channels were

1222 likely wider and less mobile, similar to modern channels (Section 2), due to the high
1223 stream power and transport capability (e.g., Wickert et al., 2013; Bufe et al., 2016; Fig.
1224 21b). In contrast, weak monsoon periods should have decreased river discharge and
1225 formed a finer-grained channel environment (Fig. 21a, c). These rivers were likely
1226 narrower and had higher lateral mobility, forming distinct floodplains and occasional river
1227 bedload sediments, as inferred from Facies B (Fig. 21c).

1228



1229

1230 **Figure 21. Overview of observed facies and inferred evolution of depositional**

1231 **environment. (a) Summary of observed facies (see main text). (b) Left: Fluvial**

1232 **environment during strengthened monsoon characterized by wide braided rivers.**

1233 **Rivers are marked in blue. Right: Schematic image of coarse-grained braided**

1234 **channel facies (Facies A) during strengthened monsoon. These rivers are wide with**
1235 **less distinct floodplains (less laterally mobile). (c) Left: Fluvio-lacustrine**
1236 **environment during weak monsoon, characterized by narrower braided rivers.**
1237 **Right: Schematic image of fine-grained braided channel facies (Facies B) during**
1238 **weak monsoon. These rivers were laterally mobile, with adjacent floodplain levees.**

1239

1240 Other regions around the Himalaya also exhibit a coarse alluvial/fluvial
1241 aggradation around the early Holocene (~12–6 ka). These results are inferred from fluvial
1242 terraces in several duns and valleys between the MFT and MBT, including the Subathu
1243 sub-basin (Kumar et al., 2007), Ganga valley (Sinha et al., 2010; Ray and Srivastava,
1244 2010), Yamuna valley (Dutta et al., 2012), Kangra Dun (Dey et al., 2016) and Pinjaur Dun
1245 (Suresh et al., 2007), and in foreland alluvial fan systems south of the MFT, such as the
1246 Matiali inter-megafan (Kar et al., 2014) and the southern Ganga Plain (Sinha et al., 2007)
1247 (Supporting Information Fig. S8). These studies document a shift from a fine-grained
1248 environment such as interfluvial floodplains, distal fans, paleosols, aeolian and lakes
1249 during the last glacial, to a coarser-grained environment in the early Holocene (e.g., Sinha
1250 et al., 2007; Kumar et al., 2007; Srivastava et al., 2009; Dutta et al., 2012). Loess
1251 deposition, as observed in Facies B in this study (Section 4), is reported in multiple

1252 regions in the Himalaya (e.g., Pant et al., 2005; Srivastava et al., 2003a, 2009), often tied
1253 to cold, dry and windier conditions when the monsoon was weaker (e.g., Harrison et al.,
1254 2001; Pourmand et al., 2004).

1255 Although the primary shift from fine to coarser sediments is likely climatic in
1256 origin, the lacustrine Facies C in this study observed at Site P2 is not. We interpret that
1257 this section is the result of uplift around the frontal thrust temporarily defeating the river,
1258 resulting in a local depocenter and ponding (Section 5.1.1; Fig. 21c). However, the fact
1259 that this ponding no longer exists suggests that it may have been favoured by the weaker
1260 monsoon conditions that were active at the time: the reduced river discharge made its
1261 defeat by tectonic uplift more likely.

1262 These lacustrine sediments may provide a record of climate-related hydrological
1263 changes. For example, the alternations from oxidized to gleyed clay observed at 29–34
1264 mbs at Site P2 (Figs. 4b, 12a, Section 4.1.2) imply diagenetic changes from aerobic to
1265 anaerobic conditions, perhaps related to the stadial Heinrich 4–6 events (Fig. 20). The
1266 increase in $\delta^{13}\text{C}$ values (-13.6–11‰) in gleyed fine sediments at 33–41 mbs suggests
1267 decreased precipitation (Table 1). The gradual transition to oxidized sediments above 29
1268 mbs (Fig. 4b) and the low $\delta^{13}\text{C}$ values (-17 to -14.4‰) between 28–30 mbs (Table 1,
1269 Section 4.1.2), may reflect a transition to a warmer climate towards the Holocene, as the

1270 paleo-lake was gradually filled by fluvial input. Based on our limited ages, we cannot
1271 confidently relate these variations to regional climate, but suggest that these sediments
1272 could provide a window into past climate in this region.

1273

1274 **5.2.2. Implications for base level changes across monsoonal climate variation**

1275 In addition to stratigraphic changes, we also observe striking changes in relative
1276 base level, likely also tied to climatic variations. Sites P1–P5 are located in the hanging
1277 wall of the MFT, and therefore tectonic uplift should lower the relative river base level,
1278 decreasing the accommodation space for sediments. This is consistent with the angular
1279 unconformity imaged in the hanging wall of the Bardibas thrust beneath the Bhabsi River
1280 that indicates that the local base level was at least 100 m lower than the present river level
1281 when it formed, however after that anticline beveling event, it has risen (Almeida et al.,
1282 2018) (Figs. 3d, 14). To explain this, we must conclude that monsoonal climate variations
1283 have affected river base levels in this region (Fig. 22). In the footwall, an incised valley
1284 observed in the Ratu River profile also suggests that relative base levels fluctuated in the
1285 past (Almeida et al., 2018) (Fig. 15). Based on sediment ages determined here, there has
1286 been significant net aggradation over the last few 10s of ka, but it is likely that the
1287 observed record is not continuous, preferentially preserving sediments deposited in the

1288 early parts of aggradation periods, as the upper sediments might have been later eroded
 1289 as base level once again dropped (Fig. 22). This process was likely more intense in the
 1290 hanging wall region (Sites P1–P5) than the footwall (Sites P7–P10), as the hanging wall
 1291 has been subject to persistent tectonic uplift.

1292

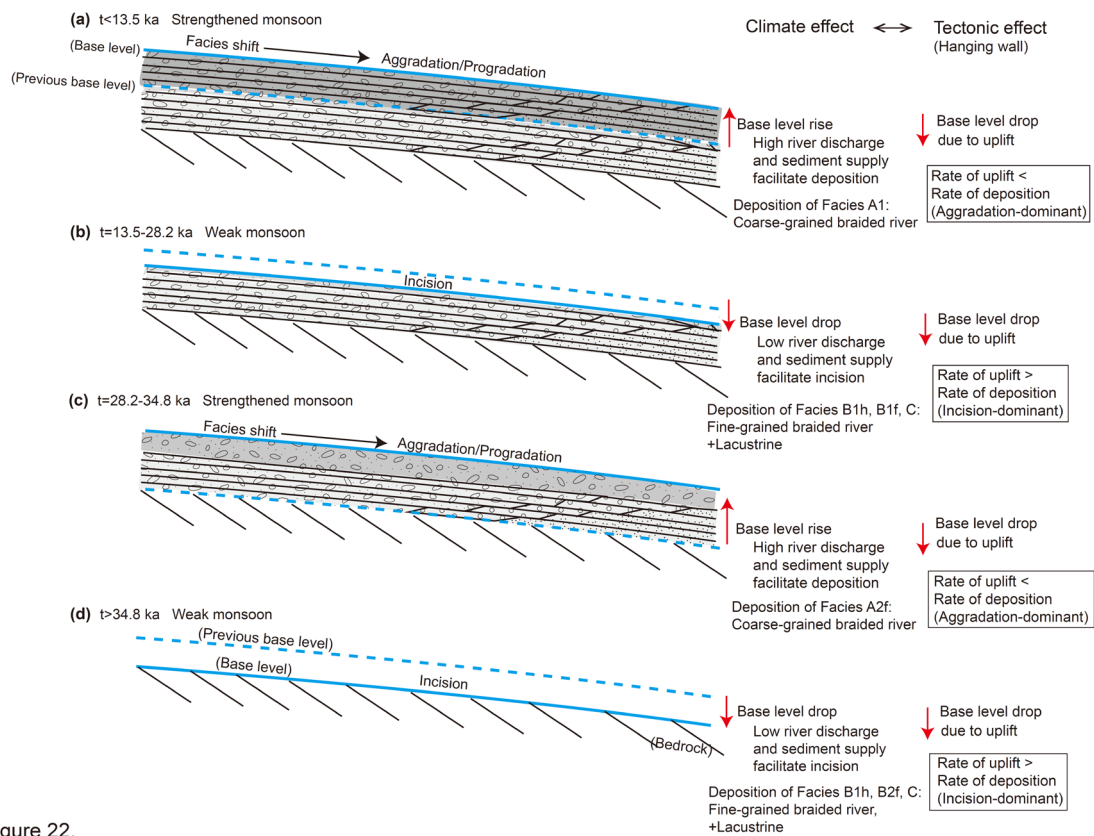


Figure 22.

1294 **Figure 22. Base level evolution inferred in this study during different time intervals.**
 1295 **Solid blue line: location of base level at each time stage. Dashed blue line: location**
 1296 **of previous base level. Tectonic uplift in the hanging wall lowers the relative base**
 1297 **level. (a) $t < 13.5$ ka: Sediment aggradation/progradation is facilitated by**

1298 **strengthened monsoon that causes increase in river discharge and sediment supply,**
1299 **raising the base level. Facies A1 deposited during this period. (b) $t=13.5\text{--}28.2$ ka:**
1300 **During a weak monsoon period, a decrease in river discharge and sediment supply**
1301 **facilitated incision and base level fall, or slow base level rise. Incision and slow**
1302 **deposition occurred, and Facies B and C were deposited during this period. (c)**
1303 **$t=28.2\text{--}34.8$ ka: Dominant aggradation/progradation, rise of base level, and**
1304 **deposition of Facies A2 during strengthened monsoon (similar process as $t<13.5$ ka).**
1305 **(d) $t>34.8$ ka: Enhanced incision, base level fall and/or slow rise, and deposition of**
1306 **Facies B and C during weak monsoons (similar process as $t=13.5\text{--}28.2$ ka).**

1307

1308 Regionally, the monsoon is known to have a substantial influence on base level
1309 (Figs. 1, Supporting Information Fig. S8). In Higher and Lesser Himalayan rivers,
1310 increased river discharge during strengthened monsoons is inferred to produce large
1311 sediment supply and immediate aggradation in the form of increased alluvium, fill-terrace
1312 deposits and landslides, raising river base levels (e.g., Pratt et al., 2002, 2004; Bookhagen
1313 et al., 2005, 2006) (Fig. 1). This upstream aggradation is associated with lower sediment
1314 supply downstream, as observed in the Ganga and Yamuna Rivers in the Ganga Plain,
1315 where high river discharge but low sediment supply during a strengthened monsoon

1316 favours incision, lowering the base level (e.g., Srivastava et al., 2003b; Gibling et al.,
1317 2005; Sinha et al., 2007) (Fig. 1). In our case, the sites we are studying are very close to
1318 the headwaters of the rivers, and our results more closely mirror the upstream results.

1319 Other studies in the piedmont foreland, however, do not always report consistent
1320 results. Some report similar patterns: in the Kangra Dun valley (Thakur et al., 2014; Dey
1321 et al., 2016), Dehra Dun (Densmore et al., 2016), and Matiali inter-megafan (Kar et al.,
1322 2014), strengthened monsoons seem to be associated with high river discharge, high
1323 sediment supply and dominant fan/terrace aggradation (Fig. 1), with incision during weak
1324 monsoon conditions. However, other regions report different patterns: in the Subathu sub-
1325 basin (Kumar et al., 2007), Ganga valley (Sinha et al., 2009; Ray and Srivastava, 2010),
1326 Yamuna valley (Dutta et al., 2012), and Pinjaur Dun (Suresh et al., 2007), strengthened
1327 monsoons seem to be associated with high river discharge, low sediment supply and
1328 dominant incision in the form of terrace abandonment and base level drop (Fig. 1). These
1329 studies suggest that there is higher sediment supply during weak monsoon periods due to
1330 less vegetation cover and enhanced weathering.

1331 All of these studies in the piedmont agree that a strengthened monsoon should
1332 increase river discharge, but suggest different patterns in sediment supply. We note that
1333 the regions where sediment supply seems to decrease are formed by large river systems

1334 (e.g. Ganga river), and are relatively downstream, compared to the smaller, foothill-fed
1335 river systems closer to the catchment like the ones in this study. Thus, these differences
1336 likely reflect very real differences in the erosion patterns and sediment transport of
1337 different scales of fluvial systems.

1338

1339 **6. Conclusions**

1340 We drilled and cored to depths of 45–100 m at ten sites along three rivers crossing
1341 the southernmost blind fault strand of the MFT in central Nepal, locally named the
1342 Bardibas thrust. We characterize the sedimentary facies of the recovered cores, and obtain
1343 sediment ages using OSL and radiocarbon dating. By combining our observations with
1344 previously published seismic profiles, we study the subsurface structure and the slip rate
1345 of the Bardibas thrust, and infer the evolution of the depositional environment. Our main
1346 findings are:

- 1347 1. Sediment cores reveal a lacustrine depocenter between the south-dipping limb of the
1348 hanging wall anticline and a north-dipping limb of a smaller tip-line fold, formed due
1349 to the uplift near the fault tip of the Bardibas thrust. Our study is the first to document
1350 a paleolake formed by the MFT in the Nepalese Himalayan piedmont.

- 1351 2. Near the tip of the Bardibas thrust, high-angle bedding planes and deformation bands
1352 were observed in the sediment cores, ~250 m above the fault tip. These structures
1353 characterize the shallow deformation ahead of the propagating fault tip,
1354 demonstrating that deformation by the blind thrust reaches to shallow depths via local
1355 folding and small-scale faults.
- 1356 3. We identify marker beds and correlate them between boreholes. By measuring their
1357 deformation and age, our results indicate that the Bardibas thrust has slipped at an
1358 average rate of 1.9–5.9 m/ka (uplift rate: 0.9–2.0 m/ka) beneath the Lakshmi river,
1359 3.1–12.1 m/ka (uplift rate: 1.5–4.1 m/ka) beneath the Bhabsi river, and >4.8 m/ka
1360 (maximum 23.9 m/ka) (uplift rate: >2.4 m/ka; maximum uplift rate: 8.2 m/ka) beneath
1361 the Ratu river over the last ~50 ka. The rate on this section of the Bardibas thrust (3.1–
1362 12.1 m/ka; Bhabsi) represents 19–81% of the total shortening across the Himalaya at
1363 this longitude. The uplift rates estimated in this study are smaller than those reported
1364 from previous studies based on elevations of river terraces.
- 1365 4. We recognize major transitions from finer-grained, fluvio-lacustrine facies to coarse-
1366 grained braided channel facies in all ten boreholes. The timing of the facies transitions
1367 correlates with reported Indian monsoonal intensity variations linked to northern
1368 hemisphere summer solar insolation and precession. We infer that strengthened

1369 monsoon conditions led to increased river discharge and advance of coarse bedload-
1370 dominant braided channels, whereas weak monsoon periods formed a finer-grained
1371 fluvial channel environment.

1372 5. Fluctuations of river base levels in the past are evident from the seismically imaged
1373 angular unconformity underlying the deposition of ~100 m of recent sediments in the
1374 hanging wall, and an incised valley in the footwall. Monsoonal climate variations
1375 have likely affected the river base levels in this region, causing a non-steady state
1376 among uplift, deposition, and incision.

1377

1378 **Acknowledgments**

1379 This research was supported by the National Research Foundation Singapore
1380 (NRF) and the Singapore Ministry of Education under the Research Centres of Excellence
1381 initiative, the Earth Observatory of Singapore, and the NRF Fellowship scheme (award
1382 No. NRF-NRFF2013-06). This work comprises Earth Observatory of Singapore
1383 contribution no. 425. We express our gratitude to Ranjan Kumar Dahal, Manita Timilsina,
1384 Om Dhakal, Nitesh Shrestha, and staff members from Geotech Solutions International
1385 Pvt Ltd for the drilling operations and core management, and for providing laboratory
1386 space. We also thank Suman Pariyar for helping with onsite operations. We are grateful

1387 to the Department of Mines and Geology (National Seismological Center, Nepal) and
1388 their staff members for providing laboratory space and core storage space. We thank Zhi
1389 Long Goh, Jing Ci Neo, Miranda Ong, and Cheng Seah for their assistance in core
1390 description and log data analyses. We are thankful to Paul Tapponnier, Çağil Karakaş,
1391 and Edgardo Latrubesse for useful discussions. We are grateful to Paula Marques
1392 Figueiredo and Antonio Votor for preparing the sediments ready for OSL dating. The
1393 authors declare that they have no known financial conflicts of interests or personal
1394 relationships that could have appeared to influence the results of this paper.

1395

1396 **Open Research**

1397 All data used in this study is attached in Supporting Information. The satellite image in
1398 Figure 2b uses a map from Google Earth imagery, Image Landsat/Copernicus.

1399

1400 **References**

- 1401 Adamiec, G. & Aitken, M. (1998). Dose-rate conversion factors: update. *Ancient TL*, 16,
1402 37–50.
- 1403 Ader, T., Avouac, J., Liu-Zeng, J., Lyon-Caen, H., Bollinger, L., Galetzka, J., Genrich, J.,
1404 Thomas, M., Chanard, K., Sapkota, S. N., Rajaure, S., Shrestha, P., Ding, L., &

- 1405 Flouzat, M. (2012). Convergence rate across the Nepal Himalaya and interseismic
1406 coupling on the Main Himalayan Thrust: Implications for seismic hazard. *Journal*
1407 *of Geophysical Research: Solid Earth*, 117(B04403),
1408 doi:<https://doi.org/10.1029/2011JB009071>.
- 1409 Almeida, R. V., Hubbard, J., Liberty, L., Foster, A., & Sapkota, S. N. (2018). Seismic
1410 imaging of the Main Frontal Thrust in Nepal reveals a shallow decollement and blind
1411 thrusting. *Earth and Planetary Science Letters*, 494, 216-225.
1412 <https://doi.org/10.1016/j.epsl.2018.04.045>
- 1413 Asahi, K. (2010). Equilibrium-line altitudes of the present and Last Glacial Maximum in
1414 the eastern Nepal Himalayas and their implications for SW monsoon climate.
1415 *Quaternary International*, 212, 26-34. doi:10.1016/j.quaint.2008.08.004
- 1416 Aydin, A. (1978). Small faults formed as deformation bands in sandstone. *Pure and*
1417 *Applied Geophysics* 116, pp. 913–930.
- 1418 Beke, B., Fodor, L., Millar, L., Petrik, A., (2019). Deformation band formation as a
1419 function of progressive burial: Depth calibration and mechanism change in the
1420 Pannonian Basin (Hungary). *Marine and Petroleum Geology* 105, pp. 1 – 16.
- 1421 Berger, A., & Loutre, M. F. (1991). Insolation values for the climate of the last 10 million
1422 years. *Quaternary Science Reviews*, 10, 297-317.

- 1423 Blum, M. D., & Törnqvist, T. E. (2000). Fluvial responses to climate and sea-level change:
1424 a review and look forward. *Sedimentology*, 47 (s1), 2-
1425 48. <https://doi.org/10.1046/j.1365-3091.2000.00008.x>.
- 1426 Bollinger, L., Sapkota, S. N., Tapponnier, P., Klinger, Y., Rizza, M., Van der Woerd, J.,
1427 Tiwari, D. R., Pandey, R., Bitri, A., & Bes de Berc, S. (2014). Estimating the return
1428 times of great Himalayan earthquakes in eastern Nepal: Evidence from the Patu and
1429 Bardibas strands of the Main Frontal Thrust. *Journal of Geophysical Research: Solid
1430 Earth*, 119, 7123-7163. doi:10.1002/2014JB010970.
- 1431 Bookhagen, B., Thiede, R. C., & Strecker, M. R. (2005). Late Quaternary intensified
1432 monsoon phases control landscape evolution in the northwest Himalaya. *Geology*,
1433 33 (2), 149-152. doi: 10.1130/G20982.1
- 1434 Bookhagen, B., Fleitmann, D., Nishizumi, K., Strecker, M. R., & Thiede, R. C. (2006).
1435 Holocene monsoonal dynamics and fluvial terrace formation in the northwest
1436 Himalaya India. *Geology*, 34 (7), 601-604. doi: 10.1130/G22698.1.
- 1437 Bookhagen, B., & Burbank, D. W. (2010). Toward a complete Himalayan hydrological
1438 budget: Spatiotemporal distribution of snowmelt and rainfall and their impact on
1439 river discharge. *Journal of Geophysical Research*, 115, F03019.
1440 doi:10.1029/2009JF001426

- 1441 Bray, D. I. (1982). Regime equations for gravel-bed rivers. *in* Hey, R.D., Bathurst, J.C.,
1442 and Thorne, C.R., eds., *Gravel-Bed Rivers; Fluvial Processes, Engineering and*
1443 *Management*: Chichester, U.K., Wiley, p. 517–542.
- 1444 Cai, Y., Fung, I. Y., Edwards, R. L., An, Z., Cheng, H., Lee, J-E., Tan, L., Shen, C-C.,
1445 Wang, X., Day, J. A., Zhou, W., Kelly, M. J., & Chiang, J. C. H. (2015). Variability
1446 of stalagmite-inferred Indian monsoon precipitation over the past 252,000 y. *PNAS*,
1447 112 (10), 2954-2959. <https://doi.org/10.1073/pnas.1424035112>
- 1448 Cashman, S., Cashman, K. (2000). Cataclasis and deformation-band formation in
1449 unconsolidated marine terrace sand, Humboldt County, California. *Geology* 28, pp.
1450 111–114. [https://doi.org/10.1130/0091-7613\(2000\)28<111:CADFIU>2.0.CO;2](https://doi.org/10.1130/0091-7613(2000)28<111:CADFIU>2.0.CO;2)
- 1451 Cashman, S.M., Baldwin, J.N., Cashman, K.V., Swanson, K., Crawford, R., (2007).
1452 Microstructures developed by coseismic and aseismic faulting in near-surface
1453 sediments, San Andreas Fault, California. *Geology* 35, pp. 611 – 614.
1454 <https://doi.org/10.1130/G23545A.1>
- 1455 Catuneanu, O., Abreu, V., Bhattacharya, J. P., Blum, M. D., Dalrymple, R. W., Eriksson,
1456 P. G., Fielding, C. R., Fisher, W. L., Galloway, W. E., Gibling, M. R., Giles, K. A.,
1457 Holbrook, J. M., Jordan, R., Kendall, C. G. St. C., Macurda, B., Martinsen, O. J.,
1458 Miall, A. D., Neal, J. E., Nummedal, D., Pomar, L., Posamentier, H. W., Pratt, B. R.,

- 1459 Sarg, J. F., Shanley, K. W., Steel, R. J., Strasser, A., Tucker, M. E., & Winker, C.
1460 (2009). Towards the standardization of sequence stratigraphy. *Earth-Science*
1461 *Reviews*, 92, 1-33. doi:10.1016/j.earscirev.2008.10.003
- 1462 Cilona, A.; Baud, P.; Tondi, E.; Agosta, F.; Vinciguerra, S.; Rustichelli, A.; Spiers, C.,
1463 (2012). Deformation bands in porous carbonate grainstones: Field and laboratory
1464 observations. *J. Structural Geology* 45, pp. 137 – 157.
1465 <https://doi.org/10.1016/j.jsg.2012.04.012>
- 1466 Collignon, M., Yamato, P., Castelltort, S., & Kaus, B. J. P. (2016). Modeling of wind gap
1467 formation and development of sedimentary basins during fold growth: application
1468 to the Zagros Fold Belt, Iran. *Earth Surface Processes and Landforms*, 41 (11), 1521-
1469 1535. <https://doi.org/10.1002/esp.3921>.
- 1470 Corvinus, G. & Rimal, L. N. (2001). Biostratigraphy and geology of the Neogene Siwalik
1471 Group of Surai Khola and Rato Khola areas in Nepal. *Palaeogeography,*
1472 *Palaeoclimatology, Palaeoecology*, 165 (2001) 251–279.
1473 [https://doi.org/10.1016/S0031-0182\(00\)00163-2](https://doi.org/10.1016/S0031-0182(00)00163-2)
- 1474 Dal Zilio, L., Hetényi, G., Hubbard, J. & Bollinger, L. (2021). Building the Himalaya
1475 from tectonic to earthquake scales. *Nature Reviews Earth & Environment*, 2, 251–
1476 268. <https://doi.org/10.1038/s43017-021-00143-1>

- 1477 Dasgupta, S., Mazumdar, K., Moirangcha, L. H., Gupta, T. D., & Mukhopadhyay, B.
1478 (2013). Seismic landscape from Sarpang re-entrant, Bhutan Himalaya foredeep,
1479 Assam, India: Constraints from geomorphology and geology. *Tectonophysics*, 592,
1480 130-140. <http://dx.doi.org/10.1016/j.tecto.2013.02.021>
- 1481 Deal, E., Favre, A. C., & Braun, J. (2017). Rainfall variability in the Himalayan orogen
1482 and its relevance to erosion processes. *Water Resources Research*, 53, 4004-4021.
1483 doi:10.1002/2016WR020030.
- 1484 DeCelles, P. G., & Cavazza, W. (1999). A comparison of fluvial megafans in the
1485 Cordilleran (Upper Cretaceous) and modern Himalayan foreland basin systems. *GSA*
1486 *Bulletin*, 111 (9), 1315-1334.
- 1487 Densmore, A. L., Sinha, R., Sinha, S., Tandon, S. K., & Jain, V. (2016). Sediment storage
1488 and release from Himalayan piggyback basins and implications for downstream river
1489 morphology and evolution. *Basin Research*, 28, 446-461. doi: 10.1111/bre.12116
- 1490 Dey, S., Thiede, R. C., Schildgen, T. F., Wittmann, H., Bookhagen, B., Scherler, D., Jain,
1491 V., & Strecker, M. R. (2016). Climate-driven sediment aggradation and incision
1492 since the late Pleistocene in the NW Himalaya, India. *Earth and Planetary Science*
1493 *Letters*, 449, 321-331. <http://dx.doi.org/10.1016/j.epsl.2016.05.050>
- 1494 Dingle, E. H., Attal, M., & Sinclair, H. D. (2017). Abrasion-set limits on Himalayan

- 1495 gravel flux. *Nature*, 544, 471-482. doi:10.1038/nature22039
- 1496 Dhital, M. R. (2015). Geology of the Nepal Himalaya, Regional perspective of the classic
1497 collided orogen. *Regional Geology Reviews*, Springer International publishing,
1498 Switzerland. DOI 10.1007/978-3-319-02496-7.
- 1499 Duncan, J.A., King, G.E., & Duller, G.A.T. (2015). DTAC: Dose Rate and Age Calculator
1500 for trapped charge dating. *Quaternary Geochronology*, 28, 54-61.
- 1501 Dutt, S., Gupta, A. K., Clemens, S. C., Cheng, H., Singh, R. K., Kathayat, G., & Edwards,
1502 R. L. (2015). Abrupt changes in Indian summer monsoon strength during 33,800 to
1503 5500 years B.P. *Geophysical Research Letters*, 42, 5526-5532,
1504 doi:10.1002/2015GL064015.
- 1505 Dutta, S., Suresh, N., & Kumar, R. (2012). Climatically controlled late Quaternary terrace
1506 staircase development in the fold-and-thrust belt of the Sub Himalaya.
1507 *Palaeogeography, Palaeoclimatology, Palaeoecology*, 356-357, 16-26.
1508 doi:10.1016/j.palaeo.2011.05.006
- 1509 Farquhar, G.D., O'leary, M.H., & Berry, J.A. (1982). On the relationship between carbon
1510 isotope discrimination and the intercellular carbon dioxide concentration in leaves.
1511 *Funct. Plant Biol.* 9 (2), 121e137.
- 1512 Finnegan, N. J., Sklar, L. S., & Fuller, T. K. (2007). Interplay of sediment supply, river

- 1513 incision, and channel morphology revealed by the transient evolution of an
1514 experimental bedrock channel. *Journal of Geophysical Research*. 112, F03S11,
1515 doi:10.1029/2006JF000569
- 1516 Fleitmann, D., Burns, S. J., Mudelsee, M., Neff, U., Kramers, J., Mangini, A., Matter, A.
1517 (2003). Holocene forcing of the Indian monsoon recorded in a stalagmite from
1518 southern Oman. *Science*, 300 (5626), 1737-1739. DOI: 10.1126/science.1083130
- 1519 Fleitmann, D., Burns, S. J., Mangini, A., Mudelsee, M., Kramers, J., Villa, I., Neff, U.,
1520 Al-Subbary, A. A., Buettner, A., Hippler, D. & Matter, A. (2007). Holocene ITCZ
1521 and Indian monsoon dynamics recorded in stalagmites from Oman and Yemen
1522 (Socotra). *Quaternary Science Reviews*, 26, 170-188.
1523 doi:10.1016/j.quascirev.2006.04.012
- 1524 Fossen, H., Schultz, R. A., Shipton, Z. K. & Mair, K. (2007). Deformation bands in
1525 sandstone: a review. *Journal of the Geological Society, London*, 164, 755-769.
- 1526 Gaillard, C., Singh, M., & Malassé, A. D. (2011). Late Pleistocene to early Holocene lithic
1527 industries in the southern fringes of the Himalaya. *Quaternary International*,
1528 229,112-122. doi:10.1016/j.quaint.2010.06.023
- 1529 Gibling, M. R., Tandon, S. K., Sinha, R., & Jain, M. (2005). Discontinuity-bounded
1530 alluvial sequences of the southern Gangetic plains, India: Aggradation and

- 1531 degradation in response to monsoonal strength. *Journal of Sedimentary Research*,
- 1532 75 (3), 369-385. DOI 10.2110/jsr.2005.029
- 1533 Goodbred S. L. & Kuehl, S. A. (2000a). The significance of large sediment supply, active
- 1534 tectonism, and eustasy on margin sequence development: Late Quaternary
- 1535 stratigraphy and evolution of the Ganges-Brahmaputra delta. *Sedimentary geology*,
- 1536 133, 227-248. [https://doi.org/10.1016/S0037-0738\(00\)00041-5](https://doi.org/10.1016/S0037-0738(00)00041-5)
- 1537 Goodbred, S. L. & Kuehl, S. A. (2000b). Enormous Ganges-Brahmaputra sediment
- 1538 discharge during strengthened early Holocene monsoon. *Geology*, 28 (12), 1083-
- 1539 1086. [https://doi.org/10.1130/0091-7613\(2000\)28<1083:EGSDDS>2.0.CO;2](https://doi.org/10.1130/0091-7613(2000)28<1083:EGSDDS>2.0.CO;2)
- 1540 Goodbred, S. L., Paolo, P. M., Ullah, M. S., Pate, R. D., Khan, S. R., Kuehl, S. A., Singh,
- 1541 S. K., & Rahaman, W. (2014). Piecing together the Ganges-Brahmaputra-Meghna
- 1542 River delta: Use of sediment provenance to reconstruct the history and interaction
- 1543 of multiple fluvial systems during Holocene delta evolution. *GSA Bulletin*, 126
- 1544 (11/12), 1495-1510. doi: 10.1130/B30965.1.
- 1545 Harrison, S. P., Kohfeld, K. E., Roelandt, C., & Claquin, T. (2001). The role of dust in
- 1546 climate changes today, at the last glacial maximum and in future. *Earth Science*
- 1547 *Reviews*, 54: 43–80. [https://doi.org/10.1016/S0012-8252\(01\)00041-1](https://doi.org/10.1016/S0012-8252(01)00041-1)
- 1548 Hey, R. D., & Thorne, C. R. (1986). Stable channels with mobile beds. *Journal of*

- 1549 *Hydraulic Engineering*, v. 112, p. 671–689.
- 1550 Hirschmiller, J., Grujic, D., Bookhagen, B., Coutand, I., Huyghe, P., Mugnier, J. L., &
1551 Ojha, T. (2014). What controls the growth of the Himalayan foreland fold-and-thrust
1552 belt? *Geology*, 42 (3), 247-250. doi:10.1130/G35057.1
- 1553 Holcomb, D.J. & Olsson, W.A. 2003. Compaction localization and fluid flow. *Journal of*
1554 *Geophysical Research*, 108(B6), 2290. <https://doi.org/10.1029/2001JB000813>
- 1555 Iseya, F. (1989). Mechanism of inverse grading of suspended load deposits. In: Taira, A.,
1556 Masuda, F. (Eds.), *Sedimentary Facies in the Active Plate Margin*, pp. 113–129.
- 1557 Jain, M. & Singhvi, A. K. (2001). Limits to depletion of blue-green light stimulated
1558 luminescence in feldspars: implications for quartz dating. *Radiation Measurements*,
1559 33 (6), 883-892. [https://doi.org/10.1016/S1350-4487\(01\)00104-4](https://doi.org/10.1016/S1350-4487(01)00104-4)
- 1560 Kaproth, B., Cashman, S., Marone, C., (2010). Deformation band formation and strength
1561 evolution in unlithified sand: The role of grain breakage. *J. Geophysical Research B*
1562 115, B12103. Doi:10.1029/2010JB007406.
- 1563 Kar, R., Chakraborty, T., Chakraborty, C., Ghosh, P., Tyagi, A. K., & Singhvi, A. K. (2014).
1564 Morpho-sedimentary characteristics of the Quaternary Matiali fan and associated
1565 river terraces, Jalpaiguri, India: Implications for climatic controls. *Geomorphology*,
1566 227, 137-152. <http://dx.doi.org/10.1016/j.geomorph.2014.05.014>

- 1567 Kathayat, G., Cheng, H., Sinha, A., Spötl, C., Edwards, R. L., Zhang, H., Li, X., Yi, L.,
1568 Ning, Y., Cai, Y., Lui, W. L., & Breitenbach, S. F. (2016). Indian monsoon variability
1569 on millennial-orbital timescales. *Scientific Reports*, 6: 24374, DOI:
1570 10.1038/srep24374
- 1571 Kohn, M.J., 2010. Carbon isotope compositions of terrestrial C3 plants as indicators of
1572 (paleo) ecology and (paleo) climate. *Proc. Natl. Acad. Sci.* 107 (46),19691e19695.
- 1573 Kotlia, B. S., Sharma, C., Bhalla, M. S., Rajagopalan, G., Subrahmanyam, K.,
1574 Bhattacharyya, A., & Valdiya, K. S. (2000). Paleoclimatic conditions in the late
1575 Pleistocene Wadda Lake, eastern Kumaun Himalaya (India). *Paleogeography,*
1576 *Paleoclimatology, Paleoecology*, 162, 105-118.
- 1577 Kotlia, B. S., Sanwal, J., & Bhattacharya, S. K. (2008). Climatic record between ca. 31
1578 and 22 ka BP in East-Central Uttarkhand Himalaya, India. *Himalayan Geology*, 29
1579 (1), 25-33.
- 1580 Kotlia, B. S., Sanwal, J., Phartiyal, B., Joshi, L. M., Trivedi, A., & Sharma, C. (2010).
1581 Late Quaternary climatic changes in the eastern Kumaun Himalaya, India, as
1582 deduced from multi-proxy studies. *Quaternary International*, 213, 44-55.
1583 doi:10.1016/j.quaint.2009.09.002
- 1584 Kumar, R., Suresh, N., Sangode, S. J., & Kumaravel, V. (2007). Evolution of the

- 1585 Quaternary alluvial fan system in the Himalayan foreland basin: Implications for
1586 tectonic and climatic decoupling. *Quaternary International*, 159, 6-20.
1587 doi:10.1016/j.quaint.2006.08.010.
- 1588 Larson, K.M., Burgmann, R., Bilham, R., & Freymueller, J.T. (1999). Kinematics of the
1589 India-Eurasia collision zone from GPS measurements. *Journal of Geophysical*
1590 *Research: Solid Earth*, 104 (B1), 1077–1093.
1591 <https://doi.org/10.1029/1998JB900043>
- 1592 Lavé, J. & Avouac, J.-P. (2000). Active folding of fluvial terraces across the Siwaliks
1593 Hills, Himalayas of central Nepal. *Journal of Geophysical Research*, 105, 5735–5770.
1594 <https://doi.org/10.1029/1999JB900292>
- 1595 Lavé, J. & Avouac, J.-P. (2001). Fluvial incision and tectonic uplift across the Himalayas
1596 of central Nepal. *Journal of Geophysical Research*, 106, B11, 26561-26591.
1597 <https://doi.org/10.1029/2001JB000359>
- 1598 Lavé, J., Yule, D., Sapkota, S., Basant, K., Madden, C., Attal, M. & Pandey, R. (2005).
1599 Evidence for a great medieval earthquake (~1100 A.D.) in the central Himalayas,
1600 Nepal. *Science*, 307, 1302-1305. 10.1126/science.1104804
- 1601 Liu, Y., Hubbard, J., Almeida, R. V., Foster, A., Liberty, L., Lee, Y. S., & Sapkota, S. N.
1602 (2020). Constraints on the shallow deformation around the Main Frontal Thrust in

- 1603 central Nepal from refraction velocities. *Tectonophysics*, 777, 228366.
1604 <https://doi.org/10.1016/j.tecto.2020.228366>
- 1605 Manning, M. P. & Reid, R. C. (1977). CHO systems in the presence of an iron catalyst.
1606 *Industrial and Engineering Chemistry Process Design and Development*, 16(3):358–
1607 6.
- 1608 Mejdahl, V. (1979). Thermoluminescence dating: beta attenuation in quartz grains.
1609 *Archaeometry* 21, 61–73.
- 1610 Murray, A.S. and Wintle, A.G. (2000). Luminescence dating of quartz using an improved
1611 single-aliquot regenerative-dose protocol. *Radiation Measurements*, 32(1): pp57-73.
- 1612 Murray, A.S. and Wintle, A.G. (2003). The single aliquot regenerative dose protocol:
1613 potential for improvements in reliability. *Radiation Measurements*, 37(4-5):
1614 pp377-381.
- 1615 Nakata, T., Kimura, K., & Rockwell, T. (1998). First successful paleoseismic trench study
1616 on active faults in the Himalaya. *Eos, Transactions, American Geophysical Union*,
1617 79, 615.
- 1618 O'Leary, M.H. (1981). Carbon isotope fractionation in plants. *Phytochemistry* 20
1619 (4),553e567.
- 1620 Osmond, C.B., Winter, K., & Ziegler, H. (1982). Functional significance of different

- 1621 pathways of CO₂ fixation in photosynthesis. In: Lange, O.L., Nobel, P.S., Osmond,
1622 C.B., Ziegler, H. (Eds.), *Physiological Plant Ecology II*. Springer, Berlin, pp.
1623 481e499p.
- 1624 Owen, L. A., Finkel, R. C., & Caffee, M. W. (2002). A note on the extent of glaciation
1625 throughout the Himalaya during the global Last Glacial Maximum. *Quaternary*
1626 *Science Reviews*, 21, 147-157. [https://doi.org/10.1016/S0277-3791\(01\)00104-4](https://doi.org/10.1016/S0277-3791(01)00104-4)
- 1627 Owen, L. A., & Benn, D. I. (2005). Equilibrium-line altitudes of the Last Glacial
1628 Maximum for the Himalaya and Tibet: an assessment and evaluation of results.
1629 *Quaternary International*, 138-139, 55-78. doi:10.1016/j.quaint.2005.02.006
- 1630 Owen, L. A. (2009). Latest Pleistocene and Holocene glacier fluctuations in the Himalaya
1631 and Tibet. *Quaternary Science Reviews*, 28, 2150-2164.
1632 doi:10.1016/j.quascirev.2008.10.020
- 1633 Pant, R. K., Basavaiah, N., Juyal, N., Saini, N. K., Yadava, M. G., Appel, E., & Singhvi,
1634 A. K. (2005). A 20-ka climate record from Central Himalayan loess deposits. *Journal*
1635 *of Quaternary Science*, 20 (5), 485-492. DOI: 10.1002/jqs.938
- 1636 Parker, G. (1978). Self-formed straight rivers with equilibrium banks and mobile bed.
1637 Part 2. The gravel river. *Journal of Fluid Mechanics*, v. 89, p. 127–146.
- 1638 Pickering, J. L., Goodbred, S. L., Reitz, M. D., Hartzog, T. R., Mondal, D. R., & Hossain,

- 1639 M. S. (2014). Late Quaternary sedimentary record and Holocene channel avulsions
1640 of the Jamuna and old Brahmaputra river valleys in the upper Bengal delta plain.
1641 *Geomorphology*, 227, 123-136. <http://dx.doi.org/10.1016/j.geomorph.2013.09.021>
- 1642 Pickering, J. L., Goodbred, S. L., Beam, J. C., Ayers, J. C., Covey, A. K., Rajapara, H. M.,
1643 & Singhvi, A. K. (2017). Terrace formation in the upper Bengal basin since the
1644 middle Pleistocene: Brahmaputra fan delta construction during multiple highstands.
1645 *Basin Research*, 1-18. doi: 10.1111/bre.12236
- 1646 Pizzati, M., Balsamo, F., Storti, F., (2020). Displacement-dependent microstructural and
1647 petrophysical properties of deformation bands and gouges in poorly lithified
1648 sandstone deformed at shallow burial depth (Croton Basin, Italy). *J. Structural*
1649 *Geology* 137, 104069 <https://doi.org/10.1016/j.jsg.2020.104069>
- 1650 Plink-Björklund, P. (2015). Morphodynamics of rivers strongly affected by monsoon
1651 precipitation: Review of depositional style and forcing factors. *Sedimentary Geology*,
1652 323, 110-147. <http://dx.doi.org/10.1016/j.sedgeo.2015.04.004>
- 1653 Polach, H. A., & Golson, J. (1966). Collection of specimens for radiocarbon interpretation
1654 of results. Manual No. 2, Australian Institute of Aboriginal Studies, pp. 42.
- 1655 Porat, N. (2006). Use of magnetic separation for purifying quartz for luminescence dating.
1656 *Ancient TL* 24(2): pp33-36.

- 1657 Pourmand, A., Marcantonio, F., & Schulz, H. (2004). Variations in productivity and eolian
1658 fluxes in the northeastern Arabian Sea during the past 110 ka. *Earth and Planetary*
1659 *science Letters*, 221, 39-54. doi:10.1016/S0012-821X(04)00109-8
- 1660 Pratt, B., Burbank, D. W., Heimsath, A., & Ojha, T. (2002). Impulsive alluviation during
1661 early Holocene strengthened monsoons, central Nepal Himalaya. *Geology*, 30 (10),
1662 911-914. [https://doi.org/10.1130/0091-7613\(2002\)030<0911:IADEHS>2.0.CO;2](https://doi.org/10.1130/0091-7613(2002)030<0911:IADEHS>2.0.CO;2)
- 1663 Pratt, B., Burbank, D. W., Heimsath, A., & Ojha, T. (2004). Landscape disequilibrium on
1664 1000-10,000 year scales Marsyandi River, Nepal, central Himalaya. *Geomorphology*,
1665 58 (1-4), 223-241. <https://doi.org/10.1016/j.geomorph.2003.07.002>
- 1666 Prescott, J.R., & Hutton, J.T. (1994). Cosmic ray contributions to dose rates for
1667 luminescence and ESR dating: Large depths and long-term time variations.
1668 *Radiation Measurements* **23**(2-3): pp497-500.
- 1669 Ramsay, C. B. (2009). Bayesian analysis of radiocarbon dates. *Radiocarbon*, 51 (1), 337-
1670 360. <https://doi.org/10.1017/S0033822200033865>
- 1671 Ray Y., & Srivastava, P. (2010). Widespread aggradation in the mountainous catchment
1672 of the Alaknanda-Ganga River System: timescales and implications to Hinterland-
1673 foreland relationships. *Quaternary Science Reviews*, 29, 2238-2260.
1674 doi:10.1016/j.quascirev.2010.05.023

- 1675 Reimer, P., Bard, E., Bayliss, A., Beck, J., Blackwell, P., Ramsey, C., . . . Van der Plicht,
1676 J. (2013). IntCal13 and Marine13 Radiocarbon Age Calibration Curves 0–50,000
1677 Years cal BP. *Radiocarbon*, 55(4), 1869-1887. doi:10.2458/azu_js_rc.55.16947
- 1678 Reuther, J. D., Cherkinsky, A., & Coffman, S. (2017). Radiocarbon variation in
1679 charcoal/wood and soil fractions from a loessic setting in central Alaska.
1680 *Radiocarbon*, 59, 2, 449-464. DOI:10.1017/RDC.2016.41
- 1681 Rizza, M., Bollinger, L., Sapkota, S. N., Tapponnier, P., Klinger, Y., Karakaş, Ç., Kali, E.,
1682 Etchebes, M., Tiwari, D. R., Siwakoti, I., Bitri, A., & Bes de Berc, S. (2019). Post
1683 earthquake aggradation processes to hide surface ruptures in thrust systems: The M8.
1684 3, 1934, Bihar-Nepal earthquake ruptures at Charnath Khola (Eastern Nepal).
1685 *Journal of Geophysical Research: Solid Earth*, 124(8), 9182-9207.
1686 <https://doi.org/10.1029/2018JB016376>
- 1687 Rubin, D. M., Nelson, J. M., & Topping, D. J. (1998). Relation of inversely graded
1688 deposits to suspended-sediment grain-size evolution during the 1996 flood
1689 experiment in Grand Canyon. *Geology*, 26, 99–102.
- 1690 Robinson, R. A. J. & Slingerland, R. L. (1998). Origin of fluvial grain-size trends in a
1691 foreland basin: the Pocono Formation on the Central Appalachian Basin. *Journal of*
1692 *Sedimentary Research*, 68 (3), 473-486. <https://doi.org/10.2110/jsr.68.473>

- 1693 Sapkota, S.N., Bollinger, L., Klinger, Y., Tapponnier, P., Gaudemer, Y., & Tiwari, D.
1694 (2013). Primary surface ruptures of the great Himalayan earthquakes in 1934 and
1695 1255. *Nature Geoscience*, 6, 71–76. DOI:10.1038/NGEO1669
- 1696 Sharma, S., Joachimski, M., Sharma, M., Tobschall, H. J., Singh, I. B., Sharma, C.,
1697 Chauhan, M.S. & Morgenroth, G. (2004). Lateglacial and Holocene environmental
1698 changes in Ganges plain, Northern India. *Quaternary Science Reviews*, 23, 145-159.
1699 doi:10.1016/j.quascirev.2003.10.005
- 1700 Shipton, Z.K. & Cowie, P.A. (2003). A conceptual model for the origin of fault damage
1701 zone structures in high-porosity sandstone. *Journal of Structural Geology*, 25, 333–
1702 345. [https://doi.org/10.1016/S0191-8141\(02\)00037-8](https://doi.org/10.1016/S0191-8141(02)00037-8)
- 1703 Sinha, A., Cannariato, K. G., Stott, L. D., Li, H. C., You, C. F., Cheng, H., Edwards, R.
1704 L., & Singh, I. B. (2005). Variability of southwest Indian summer monsoon
1705 precipitation during the Bølling-A° llerød. *Geology*, 33 (10), 813-816, doi:
1706 10.1130/G21498.1
- 1707 Sinha, R., Bhattacharjee, P. S., Sangode, S. J., Gibling, M. R., Tandon, S. K., Jain, M., &
1708 Godfrey-Smith, D. (2007). Valley and interfluvial sediments in the Southern Ganga
1709 plains, India: Exploring facies and magnetic signatures. *Sedimentary Geology*, 201,
1710 386-411. doi:10.1016/j.sedgeo.2007.07.004

- 1711 Sinha, S., Suresh, N., Kumar, R., Dutta, S., & Arora, B. R. (2010). Sedimentologic and
1712 geomorphic studies on the Quaternary alluvial fan and terrace deposits along the
1713 Ganga exit. *Quaternary International*, 227, 87-103.
1714 doi:10.1016/j.quaint.2009.09.015
- 1715 Sinha, R., Ahmad, J., Gaurav, K., & Morin, G. (2014). Shallow subsurface stratigraphy
1716 and alluvial architecture of the Kosi and Gandak megafans in the Himalayan
1717 foreland basin, India. *Sedimentary Geology*, 301, 133-149.
1718 <http://dx.doi.org/10.1016/j.sedgeo.2013.06.008>
- 1719 Skolasińska, K. (2014). Inquiry of levee formation by grain size analysis – A case study
1720 from the Warta River (central Poland). *Catena*, 122, 103-110.
1721 <http://dx.doi.org/10.1016/j.catena.2014.06.014>
- 1722 Srivastava, P., Singh, I. B., Sharma, S., Shukla, U. K., & Singhvi, A. K. (2003a).. Late
1723 Pleistocene-Holocene hydrologic changes in the interfluvial areas of the central
1724 Ganga Plain, India. *Geomorphology*, 54, 279-292. doi:10.1016/S0169-
1725 555X(02)00361-6
- 1726 Srivastava, P., Singh, I. B., Sharma, M., & Singhvi, A. K. (2003b). Luminescence
1727 chronometry and late Quaternary geomorphic history of the Ganga Plain, India.
1728 *Palaeogeography, Palaeoclimatology, Palaeoecology*, 197, 15-41.

- 1729 doi:10.1016/S0031-0182(03)00384-5
- 1730 Srivastava, P., Rajak, M. K., & Singh, L.P. (2009). Late Quaternary alluvial fans and
1731 paleosols of the Kangra basin, NW Himalaya: Tectonic and paleoclimatic
1732 implications. *Catena*, 76, 135-154. doi:10.1016/j.catena.2008.10.004
- 1733 Suresh, N., Bagati, T. N., Kumar, R., & Thakur, V. C. (2007). Evolution of Quaternary
1734 alluvial fans and terraces in the intramontane Pinjaur Dun, Sub-Himalaya, NW India:
1735 interaction between tectonics and climate change. *Sedimentology*, 54, 809-833. doi:
1736 10.1111/j.1365-3091.2007.00861.x
- 1737 Thakur, V.C., Joshi, M., Sahoo, D., Suresh, N., Jayangondapermal, R., & Singh, A. (2014).
1738 Partitioning of convergence in Northwest Sub-Himalaya: estimation of late Qua-
1739 ternary uplift and convergence rates across the Kangra reentrant, North India.
1740 *International Journal of Earth Sciences*, 103, 1037–1056.
1741 <http://dx.doi.org/10.1007/s00531-014-1016-7>.
- 1742 Tsukamoto, S., Asahi, K., Watanabe, T., & Rink, W. J. (2002). Timing of past glaciations
1743 in Kanchenjunga Himal, Nepal by optically stimulated luminescence dating of tills.
1744 *Quaternary International*, 97-98, 57-67. [https://doi.org/10.1016/S1040-](https://doi.org/10.1016/S1040-6182(02)00051-4)
1745 [6182\(02\)00051-4](https://doi.org/10.1016/S1040-6182(02)00051-4)
- 1746 Ulak, P. D. (2009). Lithostratigraphy and late Cenozoic fluvial styles of Siwalik Group

- 1747 along Kankai River section, east Nepal Himalaya. *Bulletin of the Department of*
1748 *Geology, Tribhuvan University, Kathmandu, Nepal*, Vol. 12, 2009, pp. 63–74.
- 1749 Vermeesch, P. (2009). Radial Plotter: a Java application for fission track, luminescence
1750 and other radial plots, *Radiation Measurements*, 44, 4, 409-410.
- 1751 Vogel, J. S., Southon, J. R., Nelson, D. E., & Brown, T. A. (1984). Performance of
1752 catalytically condensed carbon for use in accelerator mass spectrometry. *Nuclear*
1753 *Instruments and Methods in Physics Research Section B: Beam Interactions with*
1754 *Materials and Atoms*, 5 (2), 289-293. [https://doi.org/10.1016/0168-583X\(84\)90529-](https://doi.org/10.1016/0168-583X(84)90529-9)
1755 9
- 1756 Wang, Y., Cheng, H., Edwards, R. L., He, Y., Kong, X., An, Z., Wu, J., Kelly, M. J.,
1757 Dykoski, C. A., & Li, X. (2001). The Holocene Asian Monsoon: Links to solar
1758 changes and North Atlantic climate. *Science*, 308 (5723), 854-857. DOI:
1759 10.1126/science.1106296
- 1760 Wennberg, O., Casini, G., Jahanpanah, A., Lapponi, F., Ineson, J., Wall, B., Gilespe, P.,
1761 (2013). Deformation bands in chalk, examples from the Shetland Group of the
1762 Oseberg Field, North Sea, Norway. *Journal of Structural Geology*, 56, pp. 103 – 117.
1763 <https://doi.org/10.1016/j.jsg.2013.09.005>
- 1764 Wesnousky, S. G., Kumahara, Y., Chamlagain, D., Pierce, L. K., Karki, A., & Gautam, D.

- 1765 (2017). Geological observations on large earthquakes along the Himalayan frontal
1766 fault near Kathmandu, Nepal. *Earth and Planetary Science Letters*, 457, 366-375.
1767 <https://doi.org/10.1016/j.epsl.2016.10.006>
- 1768 Wesnousky, S. G. (2020). Great pending Himalaya earthquakes. *Seismological Research*
1769 *Letters*, 91 (6), 3334-3342. <https://doi.org/10.1785/0220200200>
- 1770 Wickert, A. D., Martin, J. M., Tal, M., Kim, W., Sheets, B., & Paola, C. (2013). River
1771 channel lateral mobility: metrics, time scales, and controls. *Journal of Geophysical*
1772 *Research*, 118 (2), 396-412. <https://doi.org/10.1029/2012JF002386>
- 1773 Willett, S. D., & Brandon, M. T. (2002). On steady states in mountain belts. *Geology*, 30
1774 (2), 175-178. [https://doi.org/10.1130/0091-
1775 7613\(2002\)030<0175:OSSIMB>2.0.CO;2](https://doi.org/10.1130/0091-7613(2002)030<0175:OSSIMB>2.0.CO;2)
- 1776 Wilson, J., Goodwin, L., Lewis, C., (2003). Deformation bands in nonwelded ignimbrites:
1777 Petrophysical controls on fault-zone deformation and evidence of preferential fluid
1778 flow. *Geology* 31, pp. 837 – 840. <https://doi.org/10.1130/G19667R.1>
- 1779 Wintle, A.G. & Murray, A.S. (2006). A review of quartz optically stimulated
1780 luminescence characteristics and their relevance in single-aliquot regeneration
1781 dating protocols. *Radiation Measurements*, 41(4): pp369-391.
- 1782 Wolff, E. W., Chappellaz, J., Blunier, T., Rasmussen, S. O., & Svensson, A. (2010).

- 1783 Millennial-scale variability during the last glacial: The ice core record. *Quaternary*
1784 *Science Reviews*, 29, 2828-2838. doi:10.1016/j.quascirev.2009.10.013
- 1785 Wu, Y., Wang, S., & Zhou, L. (2011). Possible factors causing older radiocarbon age for
1786 bulk organic matter in sediment from Daihai Lake, north China. *Radiocarbon*, 53, 2,
1787 359-366. <https://doi.org/10.1017/S0033822200056617>
- 1788 York, D., & Evensen, N. M. (2004). Unified equations for the slope, intercept, and
1789 standard errors of the best straight line. *American Journal of Physics*, 72 (3), 367.
1790 <https://doi.org/10.1119/1.1632486>